

**NONLINEAR ULTRASOUND FOR THE CHARACTERIZATION OF  
ADDITIVELY MANUFACTURED METALS**

A Dissertation  
Presented to  
The Academic Faculty

by

Aurelio Bellotti

In Partial Fulfillment  
of the Requirements for the Degree  
Doctor of Philosophy in the  
GW Woodruff School of Mechanical Engineering

Georgia Institute of Technology  
May 2023

**COPYRIGHT © 2023 BY AURELIO BELLOTTI**

# **NONLINEAR ULTRASOUND FOR THE CHARACTERIZATION OF ADDITIVELY MANUFACTURED METALS**

Approved by:

Dr. Laurence Jacobs, Advisor  
School of Mechanical Engineering  
*Georgia Institute of Technology*

Dr. Aaron Stebner  
School of Mechanical Engineering  
*Georgia Institute of Technology*

Dr. Jin-Yeon Kim  
School of Civil Engineering  
*Georgia Institute of Technology*

Dr. Jianmin Qu  
Department of Mechanical Engineering  
*Tufts University*

Dr. Christopher Saldana  
School of Mechanical Engineering  
*Georgia Institute of Technology*

Date Approved: March 29, 2023

To Brinkley Raynor and our future together.

## ACKNOWLEDGEMENTS

I would first like to thank my advisors, Dr. Laurence Jacobs and Dr. Jin-Yeon Kim. I chose to attend Georgia Tech based on their work and recommendations of their excellent advising. These recommendations have proven to be true, as both have tremendously helped me understand not only the technical content, but also how to be an effective researcher. I would also like to thank the other members of my committee: Dr. Chris Saldana, Dr. Aaron Stebner, and Dr. Jianmin Qu for their individualized expertise that provides valuable assessment to this work.

I would like to thank the NEUP for providing me with financial support through the University Program Graduate Fellowship. This fellowship has funded me throughout the majority of my PhD and has allowed me to attend conferences, spend time at Los Alamos National Laboratory, and pursue the research of my own interest.

I would like to thank Sandia National Labs for their financial and material support at the beginning of my time at Georgia Tech. I would also like to thank Los Alamos National Laboratory for their material and collaborative support. Dr. Carly Donahue was a wonderful host during my research externship. Dr. Donahue and Dr. Colt Montgomery provided valuable expertise on the test material.

I would like to thank Donald VanderLaan and Dr. Stanislav Emelianov of the Georgia Tech Wallace H. Coulter Department of Biomedical Engineering for their help and use of laboratory equipment. Don provided essential time and expertise in helping setup research equipment that is fundamental to the success of this work.

I would like to thank all my lab mates that I have had the pleasure to work with throughout my time at Georgia Tech. I would like to thank the numerous undergraduate students I've had the pleasure of working with whose questions forced me to solidify my understanding of difficult research topics. I would like to thank the wonderful group of lab mates including Kathrin Hoffmann, Sangyun Park, Denis Pfeifer, Niklas Fahse, Marius Goletz, Max May, Denis Smajic, Hengyu Yang, Nate Tenorio, Fabian Gmeiner, Emmeline Evans, and Keshav Bhat. They have been great colleagues and friends during our time in lab and across the country attending conferences. I would like to particularly thank Brian Fuchs and Katie Scott Levy who taught me how to make measurements, about grad school, with course work, during Qualifying exams, and for their friendship.

I would like to thank my family who have always been there for me with their love and encouragement. My parents have always emphasized the importance of education, which has led to my pursuit of graduate degrees. My brothers have been great examples for me to follow and are always a great source of guidance. I would like to thank my fiancée Brinkley Raynor for her invaluable help and support throughout graduate school.

# TABLE OF CONTENTS

<b>ACKNOWLEDGEMENTS</b>	<b>iv</b>
<b>LIST OF TABLES</b>	<b>ix</b>
<b>LIST OF FIGURES</b>	<b>x</b>
<b>LIST OF SYMBOLS AND ABBREVIATIONS</b>	<b>xv</b>
<b>SUMMARY</b>	<b>xviii</b>
<b>CHAPTER 1. Introduction</b>	<b>1</b>
<b>1.1 Motivation</b>	<b>1</b>
<b>1.2 Objectives</b>	<b>4</b>
1.2.1 Objective 1: Theorization and Development of Nonlinear Wave Mixing Technique with Phased Arrays	4
1.2.2 Objective 2: Scan AM Specimen for Materials Characterization	4
1.2.3 Objective 3: Verification of AM Specimens with NDE techniques	5
<b>1.3 Structure of Thesis</b>	<b>5</b>
<b>CHAPTER 2. Background and Theory</b>	<b>7</b>
<b>2.1 Linear Acoustics at Medium Boundaries</b>	<b>7</b>
2.1.1 Snell’s Law	8
2.1.2 Efficiency	9
<b>2.2 Nonlinear Elasticity Background</b>	<b>13</b>
<b>2.3 Nonlinear Wave Equation</b>	<b>15</b>
<b>2.4 Nonlinear Ultrasound</b>	<b>18</b>
<b>2.5 Nonlinear Ultrasound in Additively Manufactured Metals</b>	<b>19</b>
<b>2.6 Nonlinear Wave Mixing</b>	<b>22</b>
2.6.1 Wave Mixing Theory	22
2.6.2 Rational for Selected Mixing Condition	29
2.6.3 State of the Art in Nonlinear Wave Mixing	32
2.6.4 Benefits of Mixing Technique	34
2.6.5 Four-Way Polarity Flipping	36
<b>2.7 Phased Arrays</b>	<b>40</b>
2.7.1 Beam Steering	40
2.7.2 Beam Focusing	45
<b>2.8 Additively Manufactured Metals and Potential Defects</b>	<b>46</b>
2.8.1 Powder Bed Fusion	46
2.8.2 Scanning Speed and Power Relationship	48
2.8.3 Porosity	49
2.8.4 Dislocations	52
<b>CHAPTER 3. Materials</b>	<b>53</b>
<b>3.1 Overview</b>	<b>53</b>

<b>3.2</b>	<b>Aluminum Specimen</b>	<b>53</b>
<b>3.3</b>	<b>Powder Bed Fusion Specimens</b>	<b>54</b>
3.3.1	Nominal and Underpowered AM Specimen	55
3.3.2	Acoustically Transparent Boundary	55
3.3.3	AM Stack	58
3.3.4	Porosity Measure	60
<b>3.4</b>	<b>Concrete Specimen</b>	<b>63</b>
3.4.1	Dimensions	63
3.4.2	Embedded Damage in Concrete Specimen	64
<b>CHAPTER 4. Experimental Procedure</b>		<b>66</b>
<b>4.1</b>	<b>Overview</b>	<b>66</b>
<b>4.2</b>	<b>Phase Unwrapping Velocity Measurement</b>	<b>66</b>
<b>4.3</b>	<b>Attenuation Measurement</b>	<b>70</b>
<b>4.4</b>	<b>Nonlinear Wave Mixing with Single Element Transducers</b>	<b>73</b>
4.4.1	Single Element Nonlinear Wave Mixing in Aluminum Block	74
4.4.2	Single Element Nonlinear Wave Mixing in Concrete	78
4.4.3	Single Element Nonlinear Wave Mixing in Homogenous AM Material	80
4.4.4	Single Element Nonlinear Wave Mixing in Heterogeneous AM Material	84
<b>4.5</b>	<b>Mixing Phased Array</b>	<b>86</b>
4.5.1	Pulse Based Transducers	86
4.5.2	Verasonics System	88
4.5.3	Scanning Arc	90
4.5.4	Mode Conversion Wedge for Phased Array	92
4.5.5	Nonlinear Phased Array Scanning in Aluminum Block	94
4.5.6	Nonlinear Phased Array Scanning in Homogenous AM Materials	99
4.5.7	Nonlinear Phased Array Scanning in Heterogeneous AM Material	101
<b>4.6</b>	<b>Bulk Material Nonlinearity</b>	<b>107</b>
<b>CHAPTER 5. Results and Discussion</b>		<b>110</b>
<b>5.1</b>	<b>Overview</b>	<b>110</b>
<b>5.2</b>	<b>Phase Unwrapping Velocity Results</b>	<b>110</b>
5.2.1	Theoretical Effects of Porosity on Speed of Sound	112
5.2.2	Sensitivity of Mixing Setup to Variation in Speed of Sound	114
<b>5.3</b>	<b>Attenuation Measurement</b>	<b>116</b>
<b>5.4</b>	<b>Mixing Single Element</b>	<b>117</b>
5.4.1	Single Element Mixing Results in Homogenous AM Material	117
5.4.2	Single Element Mixing Results in Aluminum Block	122
5.4.3	Single Element Mixing Results in Concrete	127
5.4.4	Single Element Mixing Results in Heterogeneous AM Material	129
<b>5.5</b>	<b>Mixing Phased Array</b>	<b>131</b>
5.5.1	Phased Array Mixing Results in Aluminum Block	131
5.5.2	Phased Array Mixing Results in Homogenous AM Material	134
5.5.3	Phased Array Mixing Results in Heterogeneous AM Material	135
<b>5.6</b>	<b>Bulk Nonlinearity from Second Harmonic Generation</b>	<b>139</b>
<b>CHAPTER 6. Conclusion and Future Work</b>		<b>141</b>

<b>6.1</b>	<b>Summary of Results</b>	<b>141</b>
<b>6.2</b>	<b>Recommendations for Future Work</b>	<b>143</b>
<b>6.3</b>	<b>Significance and Impact</b>	<b>144</b>
<b>APPENDIX A. Ultrasonic Derivations</b>		<b>145</b>
<b>A.1</b>	<b>Nonlinear Wave Propagation</b>	<b>145</b>
A.1.1	Derivation of Nonlinearity Parameter	145
<b>A.3</b>	<b>Acoustic Attenuation</b>	<b>149</b>
A.3.1	Derivation of Acoustic Attenuation	149
<b>A.4</b>	<b>Printing Parameters of Additively Manufactured 316L PBF Specimens</b>	<b>151</b>
<b>A.4</b>	<b>Additional Additively Manufactured Specimen</b>	<b>152</b>
<b>REFERENCES</b>		<b>155</b>

## LIST OF TABLES

Table 1	Resonance Conditions for Noncollinear Interactions [28]	28
Table 2	Key for Table 3	29
Table 3	Combinations of Mixing Waves in Isotropic Solid	29
Table 4	Geometric Definitions for the Evaluation of Equation 42 for Two in Plane Shear Waves	31
Table 5	Concrete Specimen Construction Details	64
Table 6	Speed of Sound Results for Materials used in Mixing Setups	111
Table 7	Printing Parameters of AM Specimens	151

## LIST OF FIGURES

Figure 1	Geometric definition for refraction and transmission	8
Figure 2	Geometric definitions for solid-solid oblique transmission [14]	10
Figure 3	Efficiency of transmission and reflection for acrylic wedge	12
Figure 4	Frame geometric definitions of continuum [17]	13
Figure 5	Comparison of normalized $\beta$ for each specimen through heat treatment profile	20
Figure 6	Mean GND density and $\beta$ plotted concurrently of 316L PBF	20
Figure 7	Mixing of two incident waves (1,2) and the resultant scattered wave	23
Figure 8	Example of positive and negative polarity of input wave	37
Figure 9	Illustration of the four polarity combination measurements	38
Figure 10	Array geometry definition	40
Figure 11	Visualization of beam steering with phased array	41
Figure 12	Internal wedge geometry definitions for timing delay of phased array on wedge	43
Figure 13	Depiction of beam focusing	45
Figure 14	Schematic of laser powder bed fusion [62]	47
Figure 15	Scanning rate and laser power relationship	48
Figure 16	Visualization of lack-of-fusion porosity	50
Figure 17	Visualization of keyholing porosity	51
Figure 18	Images of porosity in AM. (a) Lack-of-fusion porosity [65] (b) Keyhole porosity [7]	52
Figure 19	Aluminum specimen geometry	54
Figure 20	316L PBF Specimens	55

Figure 21	Combined AM specimen	56
Figure 22	Combined AM specimen configuration	56
Figure 23	Combined AM specimen holder	57
Figure 24	Shear couplant for combined AM specimen	57
Figure 25	Additively manufactured stack specimen	59
Figure 26	Image processing steps for porosity measurement of x-CT scan. (a) Raw grayscale image. (b) Weiner adaptive noise filter (c) 2D order statistic filter (d) Fast local Laplacian filtering of images (2) Binarization of grayscale to porosity count	62
Figure 27	Schematic of a cast concrete specimen with embedded damage	64
Figure 28	Inserted damage into concrete block	65
Figure 29	Setup for measuring first through-transmitted and first reflected signal. Dashed boxes labeled 1 & 2 in specimen show path taken from first and second wave packet.	67
Figure 30	Measured signal for phase unwrapping velocity measurement	68
Figure 31	Hanning window applied for phase unwrapping velocity measurement	68
Figure 32	Unwrapped phase comparison as a function of frequency	69
Figure 33	Through transmission attenuation measurement setup. Dashed boxes labeled 1 & 2 in specimen show path taken from first and second wave packet.	72
Figure 34	Time Domain Signal for Relative Attenuation Measurement	73
Figure 35	Single element mixing setup in aluminum	75
Figure 36	Inline bandpass filter response [73]	76
Figure 37	Experimental setup for single element wave mixing in concrete	80
Figure 38	Geometric definitions for wedge angle calculation for single element mixing	81
Figure 39	Homogeneous AM single element mixing	81

Figure 40	(a) Single element mixing in nominal AM specimen (b) Single element mixing in underpowered AM specimen	85
Figure 41	Example output of pulse-based phased array system	87
Figure 42	Phillips ATL L7-4 element dimensions	89
Figure 43	Wiring diagram for nonlinear wave mixing setup using Verasonics Vantage System	90
Figure 44	Scanning arc and points for Al L7-4 mixing setup	92
Figure 45	Wedge for Phillips L7-4 phased array mixing in aluminum. Distances are marked in cm.	93
Figure 46	Wedge for Phillips L7-4 phased arrays mixing in AM specimen. Distances are marked in cm.	94
Figure 47	Experimental setup for the scanning of the aluminum block with phased arrays	96
Figure 48	Phased Array element timing needed for mixing at Point 1 in aluminum block	96
Figure 49	Scanning verification routine based on location of receiving mixed wave	98
Figure 50	Scanning arc in aluminum block with phased arrays with exact locations	98
Figure 51	Scanning arc of homogenous AM specimen with phased array	100
Figure 52	Stacked plates used to align phased array nonlinear mixing setup	102
Figure 53	Experimental setup of phased array mixing in combined AM specimen	102
Figure 54	Scanning arc for combined AM specimen with insert near boundary	104
Figure 55	Mixing packet size definition	105
Figure 56	Mixing area defined by overlapping incident waves.	106
Figure 57	Scanning arc for stacked AM specimen	107
Figure 58	Through NLU measurement schematic	108

Figure 59	Fundamental and second harmonic of through NLU measurement	109
Figure 60	$A_2$ vs $A_1^2$ . Slope is	109
Figure 61	Comparison of longitudinal wave speed between nominal and underpowered 316L PBF specimens	112
Figure 62	Comparison of transverse wave speed between nominal and underpowered 316L PBF specimens	113
Figure 63	Sensitivity of mixing angle to change in shear speed	115
Figure 64	Sensitivity of timing between elements to change in shear speed	115
Figure 65	Comparison of relative attenuation between nominal and underpowered AM	116
Figure 66	Positive-positive result with single element in nominally powered AM	119
Figure 67	All polarity combinations for single element mixing in nominally powered AM	119
Figure 68	Nominally powered AM: mixed wave following four-way polarity flipping for single element mixing	120
Figure 69	Underpowered AM: mixed wave following four-way polarity flipping for single element mixing	120
Figure 70	Comparison of relative acoustic nonlinearity measured on AM specimens with single element nonlinear wave mixing setup	121
Figure 71	Comparison of sensitivity of ultrasonic measures between material states with different porosity	122
Figure 72	Mixed wave following four-way polarity flipping for single element mixing in aluminum block	123
Figure 73	Excitation of emitting transducers independently and simultaneously	124
Figure 74	Single frame of wave propagation for single element nonlinear wave mixing in aluminum block	125
Figure 75	Laser vibrometer single frame showing reverberations in the mode conversion wedge	126

Figure 76	Corresponding particle motion of highlighted voxel in Figure 75 showing the existence of reverberations from the wedge entering the specimen.	126
Figure 77	Acoustic nonlinearity scanned in cross sections corresponding to regions with ASR damage, no damage, and fire damage	128
Figure 78	Comparison of acoustic nonlinearity at points within the concrete specimen containing no damage, ASR, and fire damage	128
Figure 79	Single element mixing polarity flipping wave result across boundary in nominal specimen	130
Figure 80	Single element mixing polarity flipping wave result across boundary in underpowered specimen	130
Figure 81	Comparison of $\beta$ for single element nonlinear mixing in heterogenous AM	131
Figure 82	Figure 82: Phased array results in aluminum when mixing at Point 1 (a) measured at Point 1 (b) measured at Point 2	133
Figure 83	Phased array results in aluminum when mixing at Point 2 (a) measured at Point 1 (b) measured at Point 2	133
Figure 84	50% of scanning arc in AM 1 with phased arrays	135
Figure 85	40% of scanning arc in AM 1 with phased arrays	135
Figure 86	Measured Signal of 55% of scanning arc for combined AM specimen	136
Figure 87	Comparison of relative acoustic nonlinearity measured with phased arrays on combined AM specimen	137
Figure 88	45% of scanning arc in combined specimen across acoustic boundary when speed of sound differences are	138
Figure 89	Measure of middle layer in stack AM	139
Figure 90	Comparison of relative $\beta$ in AM specimens	140
Figure 91	Additional 316L PBF specimen	154
Figure 92	Cross cut of additional 316L PBF specimen	154

## LIST OF SYMBOLS AND ABBREVIATIONS

AM	Additive manufacturing
NDE	Non-destructive evaluation
$z$	Characteristic acoustic independence
$\rho$	Density
$c$	Speed of sound
$p$	Acoustic pressure
<b>P</b>	Complex pressure amplitude, Piola-Kirchhoff stress tensor
$\omega$	Angular frequency
$t$	Time
$k$	Wave number
$\theta$	Propagation angle
R	Reflected wave, reflection coefficient
T	Transmitted wave, transmission coefficient
Z	Acoustic independence
A	Area
$B_0$	Lagrangian frame
$B_t$	Eulerian frame
$\mathbf{x}$	Eularian coordinate description
<b>X</b>	Lagrangian coordinate description
<b>F</b>	Deformation gradient
$\delta_{i,j}$	Kronecker delta
$\hat{\mathbf{n}}$	Unit normal vector

$b_0$	Gravitation body forces
$\chi$	Mapping function
$W$	Strain-energy density function
$C_{ij}$	Stiffness tensor
$\lambda, \mu$	Lamé constants
$l, m, n$	Third order Murnaghan constants
$\beta$	Acoustic non-linearity parameter
$\sigma$	Stress
$\varepsilon$	Strain
$E$	Elastic modulus; Energy density per volume
$\delta$	Cubic classical non-linearity parameter
$\alpha$	Hysteretic nonlinearity parameter; Attenuation
$A_1, A_2, A_3$	Wave amplitudes
PBF	Powder bed fusion
LENS	Laser engineered net shaping
GNDs	Geometrically Necessary Dislocations
EBSD	Electron backscatter diffraction
LOF	Lack of fusion
ASR	Alkali-silica reaction
SHG	Second Harmonic Generation
$U$	Wave amplitude
$a$	Frequency ratio; radius of piston
$C_T$	Transverse wave speed
$C_L$	Longitudinal wave speed
(SV)	Shear waves polarized in the plane of wave vector

- (SH) Shear waves polarized orthogonal of wave vector
- TOEC Third order elastic constants
- $\delta_x$  Element pitch
- $\theta_s$  Steering angle
- $P_{\text{laser}}$  Laser power
- $V_{\text{scan}}$  Scan speed
- $h$  Hatch spacing
- $I$  Spectra
- $D$  Diffraction coefficients
- $\varphi_0$  Phase offset
- $V$  Measured voltage
- $J_0, J_1$  Zeroth and first order Bessel function of the 1<sup>st</sup> kind

## SUMMARY

This research details the theorization and development of a novel phased array based measurement technique for nonlinear wave mixing. This measurement technique can uniquely provide localized values of the acoustic nonlinearity parameter,  $\beta$ , which is scanned from multiple points in a material of interest. Under certain resonance conditions, cross interaction between two elastic waves can generate a scattered wave whose amplitude is dependent upon the material nonlinearity at the point of mixing. A relative measure of  $\beta$  can then be used as an assessment of the local material state. Phased arrays are used in this work to generate the incident waves. In doing so, the material state of multiple localized volumes can be interrogated from the same experimental setup and contact conditions. The development of this technique is demonstrated from the various experimental iterations before arriving at a successful phased array based nonlinear wave mixing measurement method. Embedded ASR and fire damage are detected with single element nonlinear wave mixing in a concrete structure. A heterogeneous 316L AM specimen is characterized along a scanning path through different material states with phased arrays. The results from the phased array measurement show sensitivity to the change in lack-of-fusion porosity. This is the first known result showing the potential for the use of phased array for the nonlinear wave mixing to characterization a material microstructure.

# CHAPTER 1. INTRODUCTION

## 1.1 Motivation

This work details the theorization and development of a novel nonlinear ultrasonic technique for the characterization of microstructure. The technique is based on a noncollinear nonlinear wave mixing setup with phased arrays that provides a scanning capability for the mapping of acoustic nonlinearity within a specimen. Acoustic nonlinearity is measured for multiple materials including a concrete structure with known damage, but the primary measurements are focused on additively manufactured (AM) metal parts.

Linear ultrasound is a widely used tool in nondestructive evaluation (NDE). The key principles of most linear ultrasound NDE techniques is based on the scattered wave field for quantitative inversion and imaging. The ultrasonic wave is scattered by features at the same length scale as the dominant frequency of the interrogating wave. Microstructural characteristics of metals including precipitates, grains, and pores are typically on the micrometer length scale. Potential failure modes from these microstructural features typically become prominent when the damage combines and becomes significantly larger at hundreds of micrometers. Linear ultrasound in the MHz range is at the scale of hundreds of micrometers. Therefore, with linear ultrasound it is possible to effectively penetrate and to be sensitive to large scale (hundreds of micrometers) damage in metal.

Earlier detection of damage and the characterization of microstructural features below the wavelength scale is possible with nonlinear ultrasound. The quadratic nonlinear response of an acoustic wave traveling through a media is sensitive to microstructural

characteristics below the fundamental wavelength. Nonlinear ultrasound techniques have been previously shown to be sensitive to microstructural defects including in AM metals [1]. Characterization of microstructural features before the accumulation of damage is proposed here as a component in the qualification of AM parts.

Modern additive manufacturing (AM) technology has been in development for approximately 40 years [2]. Despite the constant technological improvements, uncertainty in the performance of AM parts has limited its widespread implementation, particularly in critical scenarios including in the aerospace, defense, and energy industries [3]. The uncertainty plaguing AM in critical scenarios includes material modeling challenges as AM parts are often treated as novel materials compared to their wrought counterparts [4], [5]. Further complications arise from variability in material performance due to inconsistencies in the manufacturing process [6].

Manufacturing settings and errors can have significant effects on the thermal history of a part [5]. These variables can include powder deposition rate, laser scanning velocity, layer timing, and laser power. Changes in these variables may be inadvertent. For example, smudging or scratching on lenses can lead to an effective reduction in laser power. Poor airflow in the build chamber can lead to vaporized powder which absorbs energy and causes improper fusion. Imbalance between scanning rate and laser power can cause too large of melt pools [7]. Processing errors can result in significant microstructural effects include lack-of-fusion and keyhole porosity. Conventional analysis of these defects is done by x-ray microtomography [8]–[10].

Nonlinear wave mixing techniques give a measure of acoustic nonlinearity which is localized to a defined volume of mixing. Material nonlinearities cause the cross-mixing of two incident intersecting ultrasonic waves to generate a third resulting wave. The amplitude of this third wave is dependent upon the material within the mixing zone. Therefore, it is possible to use the mixing of two ultrasonic waves for the characterization of a localized area within a test subject. This contrasts with other nonlinear ultrasound techniques which provide an averaged value over the propagation distance [11], [12]. A localized value of acoustic nonlinearity can be used to characterize a test material with inhomogeneous distribution of damage. Location specific information can lead to a better understanding of not only if a part is damaged, but the mechanism causing this damage. In the context of AM metals, a localized measure of nonlinearity would provide a more robust assessment of print quality and in the determination of whether a printing parameter is detrimentally affecting the outcome of a print.

A benefit of the nonlinear wave mixing method that is shared with other nonlinear ultrasound techniques is the sensitivity of microstructural features that are at significantly smaller scales than the input wavelength. This allows for the input wave to be a lower frequency that is less attenuated in highly dispersive media. This advantage is of particular importance in heterogeneous materials like concrete where high frequency waves are easily scattered by aggregate and in coarse grained material like cast austenitic stainless steel (CASS). The benefits to the interrogation of highly attenuative media is increased in nonlinear wave mixing setups as the propagation distance of the higher harmonic wave carrying nonlinear acoustic information is limited from the point of mixing to the receiver.

No preexisting measurement techniques can provide a similar localized value of acoustic nonlinearity. By exploiting the capabilities of ultrasonic phased array in this work, the capabilities of a nonlinear wave mixing measurement method are enhanced. The phased arrays can be configured to generate multiple input waves that meet the resonance conditions required for nonlinear wave mixing at a range of scanning locations. This allows for the scanning of a test specimen without the movement of the input setup. In large scale civil structures, this could significantly reduce scanning times. In smaller AM specimens, this can be used for a localized nonlinearity assessment of print quality for qualification of a part before it is used.

## **1.2 Objectives**

### *1.2.1 Objective 1: Theorization and Development of Nonlinear Wave Mixing Technique with Phased Arrays*

This portion of research is focused on the theorization and development of a noncollinear nonlinear wave mixing technique using phased arrays to generate the incident ultrasonic waves. With phased arrays, this setup would allow for the scanning and mapping of nonlinearity within a specimen without changing the emitting coupling condition. The limitations and possibilities of such a setup are theoretically determined and validated by experimentation.

### *1.2.2 Objective 2: Scan AM Specimen for Materials Characterization*

The next objective of this work is the adaption of the phased array based nonlinear wave mixing technique to a set of additively manufactured stainless steel specimens. These specimens are intentionally made with variations to the printing process to cause a change in the microstructure. The geometric constraint associated with the given specimens

presents a few challenges in adapting the mixing setup. Once a working system for the AM parts is tested, each AM specimen is mapped for nonlinearity using the wave mixing technique.

### *1.2.3 Objective 3: Verification of AM Specimens with NDE techniques*

The final objective of this work is validation of the nonlinear wave mixing measurement set. A ground truth of the material state is established from other ultrasonic measurements as well as imaging assessment to observe and quantify the sources of nonlinearity within the specimens. By establishing a baseline for the material state, a comparative analysis can be used to validate the effectiveness and theory of phased array based nonlinear wave mixing.

## **1.3 Structure of Thesis**

This dissertation is organized as follows. Chapter 1 provides the motivation and need for a novel nonlinear ultrasonic characterization technique and why its adaption to additively manufactured metals is fitting. Chapter 2 provides the essential background and theory needed for an understanding of this work. As nondestructive evaluation stands at the crossroads of many different engineering disciplines, the background topics are varied. They include linear and nonlinear acoustics, nonlinear wave mixing theory, phased arrays, additive manufacturing techniques, and defects associated with this manufacturing method. Chapter 3 includes an overview of all the test materials studied with this novel characterization technique. Aluminum and concrete blocks are used in parallel work that helped in the development of this measurement method. The manufacturing and materials characterization of the stainless steel additive specimens are given in this chapter. Chapter 4 contains the experimental procedures used in each of the measurements discussed in this

work. This includes linear ultrasonic measurements as well as the numerous iterations of nonlinear wave mixing setups. Chapter 5 provides the results for each of these experimental setups as well as the necessary analysis to frame the results into the context of the technique's development. Chapter 6 provides a conclusion of the works performed in this dissertation as well as provides an overview of the significance of this work and the potential future work that can be performed to continue this body of work. The Appendix contains additional and thoroughly detailed information that may be of importance to the reader but would distract from the principal story of this work.

## CHAPTER 2. BACKGROUND AND THEORY

This chapter will provide a background of the necessary concepts pertaining to this work. First detailed are the equations and laws of linear acoustics that are fundamental to the wave motion behind the main experimental setup. Then a brief background on nonlinear elasticity is introduced in order to derive the nonlinear wave equation. The nonlinear wave equation is fundamental to nonlinear ultrasonic NDE techniques. The concepts behind nonlinear ultrasonics are explained including a recap of previous work employing nonlinear ultrasound for the characterization of AM metals. The conditions required for nonlinear wave mixing are then derived. A history of nonlinear wave mixing is provided including a literature review of the state-of-the-art research in this field. Fundamental concepts to the phased arrays used in this work are then detailed. The chapter then focuses on the background of the AM materials used as test specimens in this work, including the manufacturing techniques and material defects of interest.

### 2.1 Linear Acoustics at Medium Boundaries

Important to this work are the fundamental laws describing the acoustic wave motion at the boundary of different mediums. When an acoustic wave passes across the boundary of a different medium, both reflected and transmitted waves are generated [13]. The amount of acoustic energy transmitted into the second medium instead of reflected back into the initial medium is dependent on the material properties (characteristic acoustic impedance,  $z=\rho c$ , where  $\rho$  is the mass density and  $c$  is the speed of sound) as well as the angle of incidence [13].

### 2.1.1 Snell's Law

Independently discovered throughout history, a formula describing the relationship between angles of incidence and refraction is now known as Snell's law. A derivation of this law is as follows. The case is that of a vertical boundary at  $x=0$  between two materials:

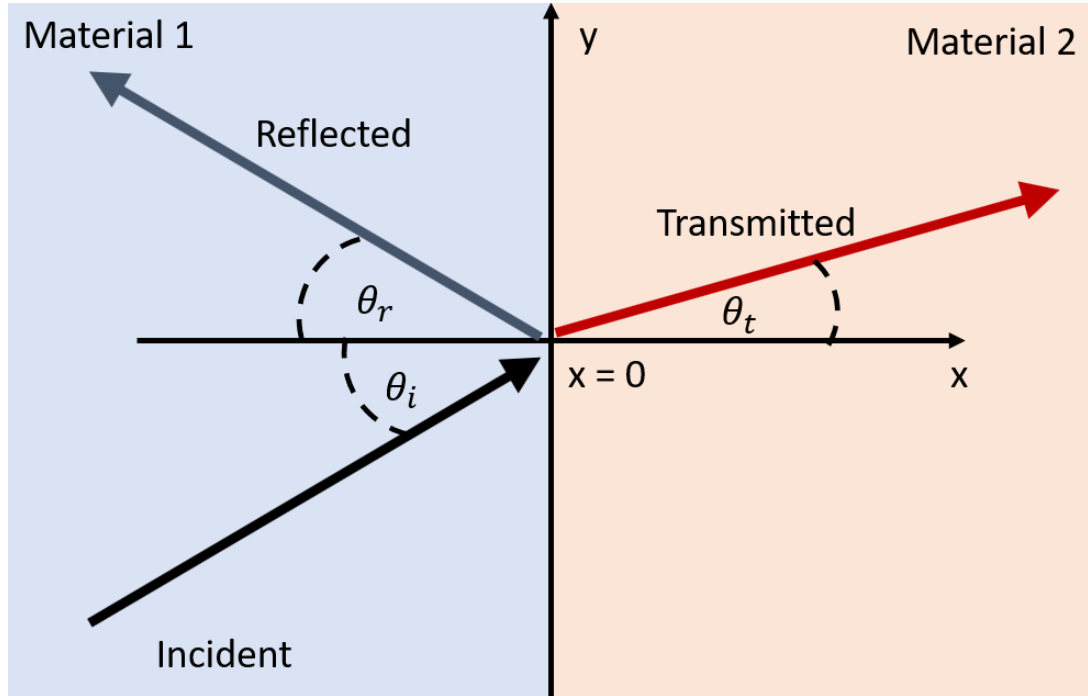


Figure 1: Geometric definition for refraction and transmission

The incident, reflected, and transmitted waves are defined as:

$$p_i = \mathbf{P}_i e^{j(\omega t - k_1 x \cos \theta_i - k_1 y \sin \theta_i)} \quad (1)$$

$$p_r = \mathbf{P}_r e^{j(\omega t + k_1 x \cos \theta_r - k_1 y \sin \theta_r)} \quad (2)$$

$$p_t = \mathbf{P}_t e^{j(\omega t - k_2 x \cos \theta_t - k_2 y \sin \theta_t)} \quad (3)$$

where the subscripts  $i$ ,  $r$ , and  $t$  refer to the incident, reflected, and transmitted waves, respectively.  $p$  is the acoustic pressure,  $\mathbf{P}$  is the complex pressure amplitude,  $\omega$  is the

angular frequency,  $t$  is time,  $k$  is wavenumber, and  $\theta$  is the propagation angle with respect to the x-axis. In keeping with continuity of pressure at the boundary ( $x=0$ ) it follows that:

$$\mathbf{P}_i e^{-jk_1 y \sin \theta_i} + \mathbf{P}_r e^{-jk_1 y \sin \theta_r} = \mathbf{P}_t e^{-jk_2 y \sin \theta_t} \quad (4)$$

Equation 4 applies at all points of the interface (at all  $y$ ), therefore the exponents must be equal and the following two statements can be made:

$$\sin \theta_i = \sin \theta_r \quad (5)$$

$$\frac{\sin \theta_i}{c_1} = \frac{\sin \theta_t}{c_2} \quad (6)$$

where Equation 6 is Snell's law and  $c$  is the speed of sound in the respective material.

### 2.1.2 Efficiency

For the effective generation of second harmonics, a sufficiently large amplitude of the fundamental harmonic must be emitted into the test material. The maximum input amplitude is set by limitations on the driving amplitude from the source and emitting elements. Losses occur at all interfaces due to imperfections in coupling. A predictable form of loss occurs from the efficiency rates for transmission through a given setup. This efficiency can be calculated and should be regarded in the development of experimental setups.

For the efficiency of reflection and transmission of both oblique longitudinal and shear waves between two solids, the following geometric definitions in Figure 2 are used where  $\theta$  defines the angle of the wave,  $R$  is the reflected component of the wave, and  $T$  is the transmitted component of the wave. Subscript  $s$  is used for shear waves,  $d$  for

longitudinal (dilatational) waves,  $i$  for the incident angle,  $l$  for the reflected angles, and 2 for the transmitted angles.

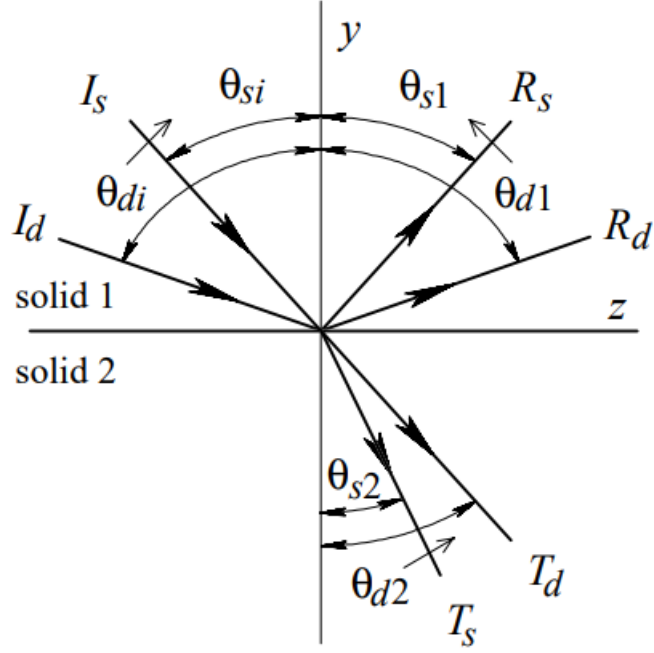


Figure 2: Geometric definitions for solid-solid oblique transmission [14]

In the case of a longitudinal transducer on a mode conversion wedge, the wedge angle is equal to  $\theta_{di}$  and the desired transmitted shear wave,  $T_s$ , is propagating at the angle  $\theta_{s2}$ . Snell's law can be applied to each angle as such:

$$\frac{\sin \theta_{di}}{c_{d1}} = \frac{\sin \theta_{si}}{c_{s1}} = \frac{\sin \theta_{d1}}{c_{d1}} = \frac{\sin \theta_{s1}}{c_{s1}} = \frac{\sin \theta_{d2}}{c_{d2}} = \frac{\sin \theta_{s2}}{c_{s2}} \quad (7)$$

The acoustic impedance is conceptualized as the amount of resistance a sound wave encounters as it passes through a material [13]. It can be defined for each material as:

$$Z = \frac{\rho \times c}{A} \quad (8)$$

where the acoustic impedance is  $Z$ ,  $\rho$  is density, and  $A$  is the cross-sectional area. The boundary conditions of two solids requires continuity of normal velocity, transverse velocity, and stress components ( $u$ ):

$$\begin{bmatrix} -u_y^{(d1)} + u_y^{(d2)} - u_y^{(s1)} + u_y^{(s2)} \\ -u_z^{(d1)} + u_z^{(d2)} - u_z^{(s1)} + u_z^{(s2)} \\ -\tau_{yy}^{(d1)} + \tau_{yy}^{(d2)} - \tau_{yy}^{(s1)} + \tau_{yy}^{(s2)} \\ -\tau_{zy}^{(d1)} + \tau_{zy}^{(d2)} - \tau_{zy}^{(s1)} + \tau_{zy}^{(s2)} \end{bmatrix} = \begin{bmatrix} u_y^{(i)} \\ u_z^{(i)} \\ \tau_{yy}^{(i)} \\ \tau_{zy}^{(i)} \end{bmatrix} \quad (9)$$

which can be simplified if the incident wave is shear ( $I_s = 1, I_d = 0$ ) or longitudinal ( $I_d = 1, I_s = 0$ ). Equation 10 can be written with displacement amplitudes as follows:

$$\begin{bmatrix} a_{11} & a_{12} & a_{13} & a_{14} \\ a_{21} & a_{22} & a_{23} & a_{24} \\ a_{31} & a_{32} & a_{33} & a_{34} \\ a_{41} & a_{42} & a_{43} & a_{44} \end{bmatrix} \begin{bmatrix} R_d \\ T_d \\ R_s \\ T_s \end{bmatrix} = \begin{bmatrix} b_1 \\ b_2 \\ b_3 \\ b_4 \end{bmatrix} \text{ or } \begin{bmatrix} c_1 \\ c_2 \\ c_3 \\ c_4 \end{bmatrix} \quad (10)$$

where vector  $\mathbf{b}$  is used for longitudinal incidence waves and vector  $\mathbf{c}$  for shear. The elements of  $\mathbf{a}$ ,  $\mathbf{b}$ , and  $\mathbf{c}$  are defined as:

$$\mathbf{a} = \begin{bmatrix} -\cos \theta_{d1} & -\cos \theta_{d2} & -\sin \theta_{s1} & \sin \theta_{s2} \\ -\sin \theta_{d1} & \sin \theta_{d2} & \cos \theta_{s1} & \cos \theta_{s2} \\ -Z_{d1} \cos 2\theta_{s1} & Z_{d2} \cos 2\theta_{s2} & -Z_{s1} \sin 2\theta_{s1} & -Z_{s2} \sin 2\theta_{s2} \\ -Z_{s1} \frac{c_{s1}}{c_{d1}} \sin 2\theta_{d1} & -Z_{s2} \frac{c_{s2}}{c_{d2}} \sin 2\theta_{d2} & Z_{s1} \cos 2\theta_{s1} & -Z_{s2} \cos 2\theta_{s2} \end{bmatrix} \quad (11)$$

$$\mathbf{b} = \begin{bmatrix} -\cos \theta_{di} \\ \sin \theta_{di} \\ Z_{d1} \cos 2\theta_{si} \\ -Z_{s1} \frac{c_{s1}}{c_{d1}} \sin 2\theta_{di} \end{bmatrix} \quad (12)$$

$$\mathbf{c} = \begin{bmatrix} \sin \theta_{si} \\ \cos \theta_{si} \\ -Z_{s1} \sin 2\theta_{si} \\ -Z_{s1} \cos 2\theta_{si} \end{bmatrix} \quad (13)$$

The reflection and transmission coefficients can then be determined by applying Cramer's rule:

$$R_d = \frac{\det[\mathbf{a}^{(1)}]}{\det[\mathbf{a}]}, T_d = \frac{\det[\mathbf{a}^{(2)}]}{\det[\mathbf{a}]}, R_s = \frac{\det[\mathbf{a}^{(3)}]}{\det[\mathbf{a}]}, R_d = \frac{\det[\mathbf{a}^{(4)}]}{\det[\mathbf{a}]} \quad (14)$$

where  $\mathbf{a}^{(i)}$  indicates that the  $i^{\text{th}}$  column of  $\mathbf{a}$  is replaced by the corresponding vector  $\mathbf{b}$  or  $\mathbf{c}$ . The transmission and reflection coefficients for the experimental setup used in this work as detailed in later sections is plotted below for a range of potential wedge angles. The chosen wedge angle is marked with a vertical line. From this analysis, the chosen angles of transmission for this work are considered good as they trend towards the maximum possible shear transmission coefficient in these materials.

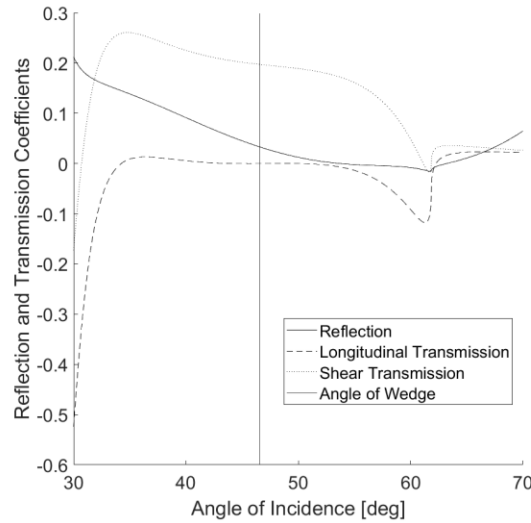


Figure 3: Efficiency of transmission and reflection for acrylic wedge

## 2.2 Nonlinear Elasticity Background

The underlying mechanics behind the nonlinear wave mixing phenomenon are dependent upon the nonlinear wave equation. Before the nonlinear wave equation can be derived, a brief summation on nonlinear elasticity must first be introduced following the works of Hamilton & Blackstock and Murnaghan [15], [16]. The nonlinear elastic behavior described in this section holds when the linear stress-strain relationship is no longer met. The defining frame and corresponding notation between the reference frame or Lagrangian,  $B_0$ , and the distorted frame or Eulerian,  $B_t$ , are shown in Figure 4. By notation, the Lagrangian frame is demarked with the capital  $X$  and the Eulerian is demarked with the lowercase  $x$ .

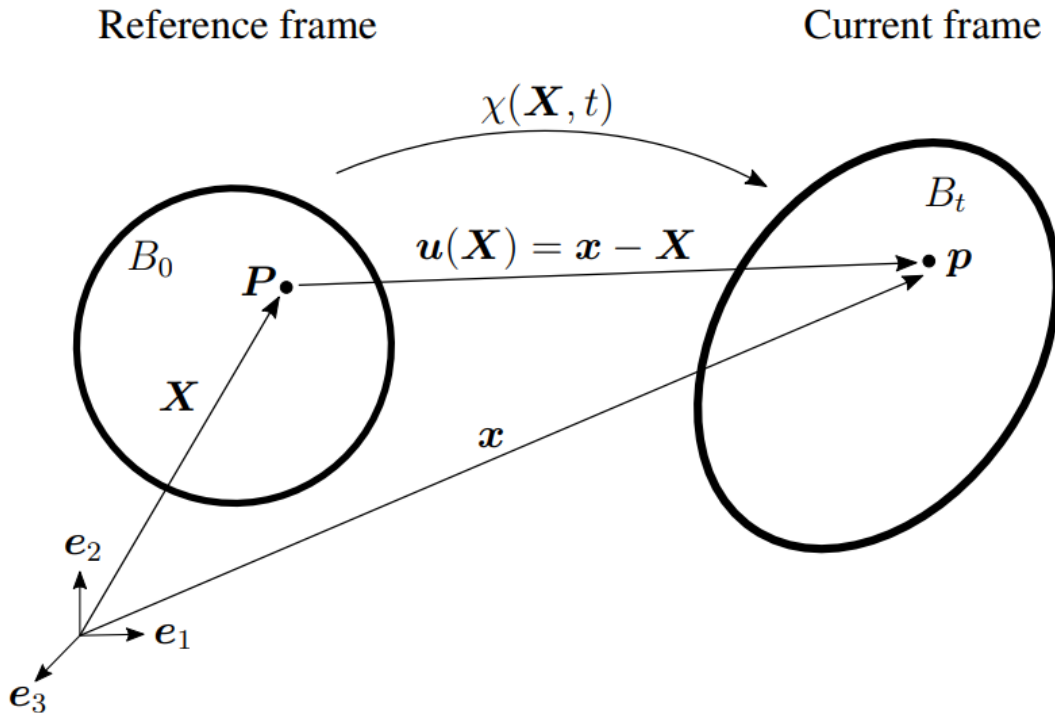


Figure 4: Frame geometric definitions of continuum [17]

As shown in Figure 4, the Lagrangian coordinates are mapped to the Eulerian coordinates by:

$$\mathbf{x} = \boldsymbol{\chi}(\mathbf{X}, t) \quad (15)$$

Further shown in Figure 4 is the particle displacement which is defined below with the substitution from Equation 15.

$$\mathbf{u}(\mathbf{X}) = \mathbf{x} - \mathbf{X} = \boldsymbol{\chi}(\mathbf{X}, t) - \mathbf{X} \quad (16)$$

The deformation gradient,  $\mathbf{F}$ , is defined as:

$$\mathbf{F} = \frac{\partial \boldsymbol{\chi}(\mathbf{X}, t)}{\partial \mathbf{X}} = \text{Grad} \boldsymbol{\chi}(\mathbf{X}, t) \quad (17)$$

The particle displacement can then be redefined using the deformation gradient as

$$F_{ij} = \frac{\partial u_i}{\partial X_j} + \delta_{ij} \quad (18)$$

where the Kronecker delta is defined as:

$$\delta_{ij} = \begin{cases} 1, & \text{for } i = j \\ 0, & \text{else} \end{cases} \quad (19)$$

where the indicial notation is expressed by the definitions of  $i, j = \{1, 2, 3\}$ . The strain tensor in the Lagrangian frame,  $E_{ij}$ , is defined as follows using the defined particle displacement.

$$E_{ij} = \frac{1}{2} \left( \frac{\partial u_i}{\partial X_j} + \frac{\partial u_j}{\partial X_i} + \frac{\partial u_m}{\partial X_i} \frac{\partial u_m}{\partial X_j} \right) \approx \frac{1}{2} \left( \frac{\partial u_i}{\partial X_j} + \frac{\partial u_j}{\partial X_i} \right) \quad (20)$$

Quadratic terms are neglected in the equation above when small displacements,  $u$ , are applied as in the case of ultrasonic measurements. Index notation is used in Equation 20 which is made briefer following Einstein summation conventions [15].

### 2.3 Nonlinear Wave Equation

Newton's second law for the balance of linear momentum is written in Lagrangian coordinates as:

$$\frac{d}{dt} \int_{B_0} \rho \dot{\chi}(\mathbf{X}, t) dV = \int_{\partial B_0} P \hat{\mathbf{n}} dA + \int_{B_0} b_0 dV \quad (21)$$

The left-hand side is the change in linear momentum. The first term on the right-hand side is the integral of surface forces in the direction of the unit normal,  $\hat{\mathbf{n}}$ , which is normal to the surface considered.  $P$  is the internal stress. The second term on the right-hand side is the integral over the gravitation body forces,  $b_0$ , over the volume. These gravitation forces are negligible in the application of acoustic waves traveling through solids.

The following steps are taken in order to find the equilibrium equation in continuum mechanics. The surface force term, first term of right-hand side in Equation 21, is rewritten as a volume integral of the stress divergence:

$$\int_{\partial B_0} P \hat{\mathbf{n}} dA = \int_{B_0} \text{Div}(P) dV \quad (22)$$

This substitution is made into Equation 21 and the expression is evaluated for all subsets of  $B_0$  as:

$$\int_{B_0} (\rho \ddot{\chi}(\mathbf{X}, t) - \text{Div}(P)) dV = 0 \quad (23)$$

$$\Rightarrow \rho \ddot{\chi}(\mathbf{X}, t) = \text{Div}(\mathbf{P})$$

This is the equilibrium equation in continuum mechanics. The time derivative of the mapping function  $\chi$  is evaluated as:

$$\ddot{\chi}(\mathbf{X}, t) = \frac{\partial^2 u}{\partial t^2} = \frac{\partial^2 (\chi(\mathbf{X}, t) - \mathbf{X})}{\partial t^2} \quad (24)$$

The time derivative is substituted into Equation 23. The expression is further evaluated with an expression for the stress tensor,  $\mathbf{P}$ . The Piola-Kirkoff stress tensor is defined as

$$\mathbf{P} = \mathbf{F} \left( \frac{\partial W(\mathbf{E})}{\partial \mathbf{E}} \right)^T \quad (25)$$

where the tensor  $\mathbf{F}$  relates Lagrangian and Eulerian quantities, and  $W$  is the strain-energy density function that can be approximated with the following Taylor Series:

$$W \approx C_o + C_{ij} E_{ij} + \frac{1}{2!} C_{ijkl} E_{ij} E_{kl} + \dots \quad (26)$$

This strain-energy density function is substituted into the expression for the Piola-Kirkoff stress tensor. Using the expression for the tensors  $\mathbf{F}$  (Equation 18) and  $\mathbf{E}$  (Equation 20) the stress tensor is found to be:

$$P_{ij} \approx C_{ijkl} \frac{\partial u_k}{\partial X_t} + \frac{1}{2} M_{ijklmn} \frac{\partial u_k}{\partial X_t} \frac{\partial u_m}{\partial X_n} + \dots \quad (27)$$

where  $C_{ij}$  is the stiffness tensor defined by the second order elastic constants and  $M_{ijklmn}$  is defined by the following second and third order elastic constants:

$$M_{ijklmn} = C_{ijklmn} + C_{ijln}\delta_{km} + C_{jnkl}\delta_{im} + C_{jlmn}\delta_{ik} \quad (28)$$

With the now defined expression for stress tensor  $\mathbf{P}$ , Equation 23 is further evaluated into the nonlinear wave equation used for nonlinear mixing as:

$$\rho \frac{\partial^2 u_i}{\partial t^2} - \mu \frac{\partial^2 u_i}{\partial X_k \partial X_k} - (\lambda + \mu) \frac{\partial^2 u_l}{\partial X_l \partial X_i} = G_i(\mathbf{u}) \quad (29)$$

where the  $\mu$  and  $\lambda$  are the Lamé parameters and  $G_i(\mathbf{u})$  is defined as

$$\begin{aligned} G_i(\mathbf{u}) = & \left(\mu + \frac{n}{4}\right) \left( \frac{\partial^2 u_l}{\partial X_k \partial X_k} \frac{\partial u_l}{\partial X_i} + \frac{\partial^2 u_l}{\partial X_k \partial X_k} \frac{\partial u_i}{\partial X_l} + 2 \frac{\partial^2 u_i}{\partial X_l \partial X_k} \frac{\partial u_l}{\partial X_k} \right) \\ & + \left(\lambda + \mu + m - \frac{n}{4}\right) \left( \frac{\partial^2 u_l}{\partial X_i \partial X_k} \frac{\partial u_l}{\partial X_k} + \frac{\partial^2 u_k}{\partial X_l \partial X_k} \frac{\partial u_i}{\partial X_l} \right) \\ & + \left(\lambda + m - \frac{n}{2}\right) \left( \frac{\partial^2 u_i}{\partial X_k \partial X_k} \frac{\partial u_l}{\partial X_l} \right) \\ & + \left(m - \frac{n}{4}\right) \left( \frac{\partial^2 u_k}{\partial X_l \partial X_k} \frac{\partial u_l}{\partial X_i} + \frac{\partial^2 u_l}{\partial X_i \partial X_k} \frac{\partial u_k}{\partial X_l} \right) \\ & + \left(2l - m + \frac{n}{2}\right) \left( \frac{\partial^2 u_k}{\partial X_i \partial X_k} \frac{\partial u_l}{\partial X_l} \right) \end{aligned} \quad (30)$$

where  $l$ ,  $m$ , and  $n$  are the third order elastic Murnaghan constants [16]. These constants are a function of the strain relation, Lamé parameters, and Poisson's ratio. They have been found to be useful in the characterization of material state [18].

## 2.4 Nonlinear Ultrasound

Nonlinear ultrasound is a useful nondestructive evaluation technique sensitive to microstructural features at significantly smaller length scales than the input wavelength [19]. This allows for the inspection and characterization of material state at finer detail and for earlier indicator than traditional ultrasound which is limited to discontinuity type defect detection of wavelength sized features such as fatigue cracks [20]. To achieve comparable levels of resolution with linear ultrasound, high frequencies must be used which limits depth penetration due to increases in attenuation. Nonlinear ultrasound has been extensively used to detect microstructural changes [11], [12], [20], [21].

In the nonlinear constitutive relationship, Equation (31), the quadratic classical nonlinearity parameter,  $\beta$ , is shown [15].

$$\sigma = \varepsilon \cdot K_0(1 + \beta\varepsilon + \delta\varepsilon^2 + \dots) + K_0 \frac{\alpha}{2} [(sgn(\dot{\varepsilon}) ((\Delta\varepsilon)^2 - \varepsilon^2) - 2(\Delta\varepsilon)\varepsilon)] \quad (31)$$

where  $\sigma$  is stress,  $\Delta\varepsilon$  is local strain amplitude and  $\dot{\varepsilon}$  is the strain rate,  $E_0$  is the linear elastic modulus,  $\delta$  is the cubic classical nonlinearity parameter, and  $\alpha$  is the hysteretic nonlinearity parameter. A relationship for  $\beta$  can be found by inserting the nonlinear constitutive relationship into the standard one-dimensional equation of wave motion:

$$\rho \frac{\partial^2 \mathbf{u}}{\partial t^2} = \nabla \cdot \boldsymbol{\sigma} \quad (32)$$

Depending on the type and motion of the ultrasonic wave, an equation for the amplitude of  $\beta$  can then be determined. The derivation of  $\beta$  is found in APPENDIX A. Ultrasonic Derivations. In this work,  $\beta$  is used as a comparative measure to assess the microstructural state at different points along a scanning path within a test specimen. Therefore, a relative

acoustic nonlinearity parameter,  $\beta$ , is used that is proportional to the amplitude of the measured waves.

$$\beta_{rel} \propto \frac{A_3}{A_1 A_2} \quad (33)$$

where  $A_1$ , and  $A_2$  are the amplitudes of the input waves of the nonlinear wave mixing setup and  $A_3$  is the amplitude of the measured wave. Detail regarding diffraction corrections to this relative measure of nonlinearity are discussed in Section 4.4.3.1.

## **2.5 Nonlinear Ultrasound in Additively Manufactured Metals**

In previous work, the acoustic nonlinearity parameter was shown to be sensitive to microstructural changes in AM specimens [1]. A comparison and progression of four specimens through a series of annealing heat treatments was performed. 316L powder bed fusion (PBF) and 304L laser engineered net shaping (LENS) specimens were compared with wrought manufactured counterparts. The specimens were measured with a nonlinear Rayleigh wave experimental setup through a heat treatment designed for the reduction of dislocation density. The number of dislocations was approximated with geometrically necessary dislocations (GNDs) from electronic backscatter diffraction (EBSD) images [22]. The results of this work are shown in Figure 5 and Figure 6 [1]:

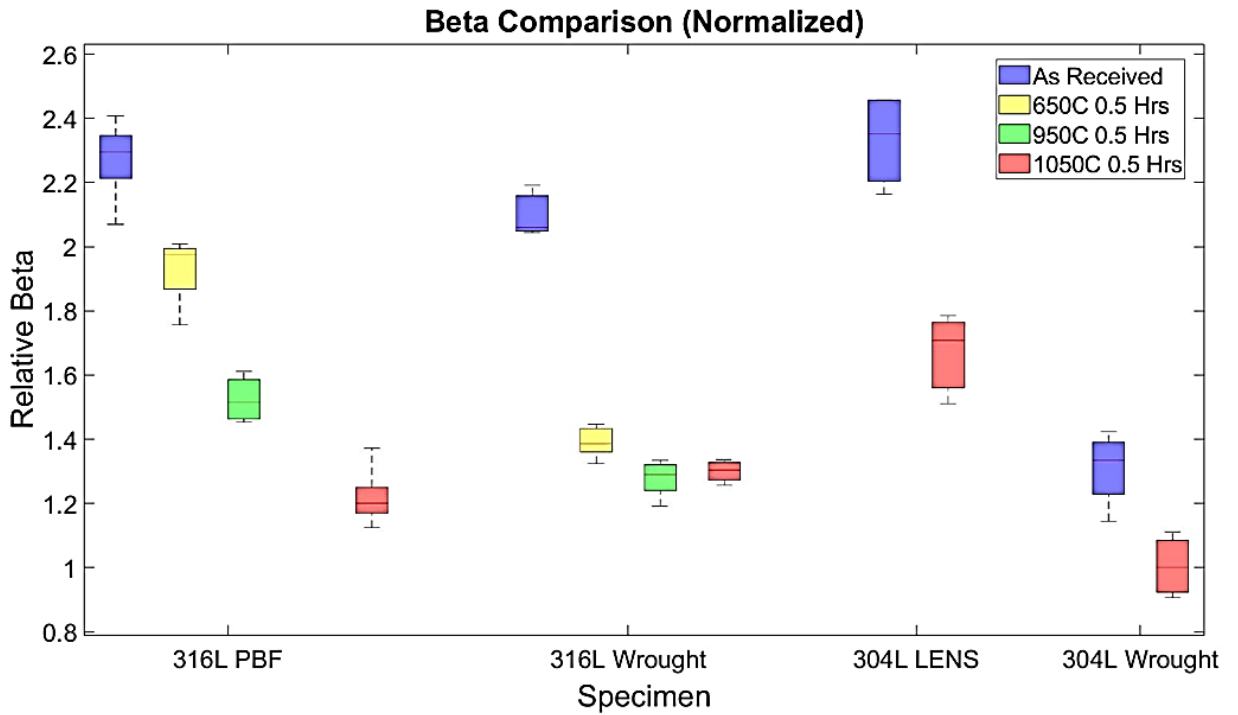


Figure 5: Comparison of normalized  $\beta$  for each specimen through heat treatment profile

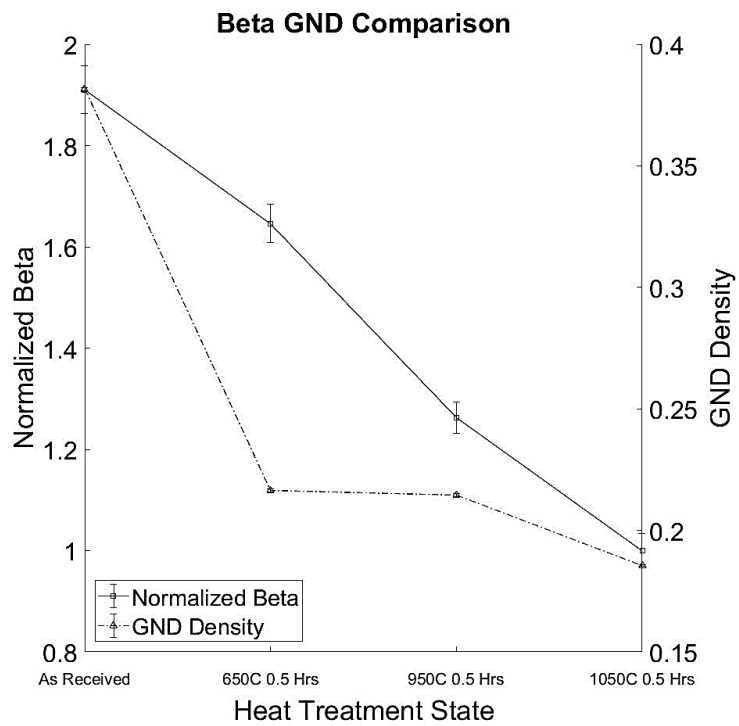


Figure 6: Mean GND density and  $\beta$  plotted concurrently of 316L PBF

The correlation coefficient between the density of GNDs and  $\beta$  is 0.85. These results show the sensitivity of nonlinear ultrasound to dislocations as predicted by Hikata [23], but the parameter is also sensitive to other microstructural features [19] and is not a unique measure of dislocation density.

Since then, other researchers have shown the sensitivity of  $\beta$  to microporosity caused by lack of fusion (LOF) [24], [25]. The AM specimens studied in these works are thought to share a similar microstructural state to the samples tested in this thesis as described in Section 3.3. These results differ from traditional ultrasonic measures of porosity in AM which are primarily based on wave speed [26], [27]. Linear techniques are not sensitive to microporosity much smaller than the signal wave length [25].

The second harmonic generation (SHG) techniques commonly used in nonlinear ultrasound measures an average  $\beta$  along the propagation path of the primary wave. These setups are adequate under the assumption of a homogenous microstructure. In cases of localized damage, the SHG approach is ineffective at mapping the location of damage. The proposed nonlinear wave mixing technique in this work is a measure of localized nonlinearity and can be used to map heterogenous damage. This damage is of particular concern in AM since the construction time and history can vary within a specimen.

## 2.6 Nonlinear Wave Mixing

### 2.6.1 Wave Mixing Theory

Under the assumption of linear elasticity, the principle of superposition would hold that any solution to the propagation of waves can be written as a linear combination of individual monochromatic waves [28]. When including nonlinear elastic terms, cross interactions between two elastic waves arise, as first described by Jones and Kobett [28].

This first work and the work detailed in this thesis are described in wave theory, but Taylor and Rollins [29] explain the principle based on a three-phonon interaction in quantum mechanics. Transition probabilities between available phonon states are calculated from first-order time-dependent perturbation theory [29].

In the description of wave theory, Korneev and Demčenko [30] expanded upon the work of Jones and Kobett [28]. The description of the cross interactions that occur between two elastic waves is found from the nonlinear wave equation (Equation 29) which was derived in Section 2.3. A solution to this nonlinear wave equation is assumed to have the following form:

$$\mathbf{u} = \mathbf{u}^{(h)} + \mathbf{u}^{(p)} \quad (34)$$

$\mathbf{u}^{(h)}$  is the solution to the linear wave equation and  $\mathbf{u}^{(p)}$  is the component of the solution to satisfy the conditions in which  $G_i(\mathbf{u}) \neq 0$  in Equation 29. For the cases in which  $G_i(\mathbf{u}) = 0$  in Equation 29, the equation corresponds to the linear wave equation and is solved by  $\mathbf{u}^{(h)}$ . The solution of the linear equation,  $\mathbf{u}^{(h)}$  for two monochromatic incident waves is as follows:

$$\mathbf{u}^{(h)}(\mathbf{X}, t) = \mathbf{U}^{(1)} \cos(\omega_1 t - \mathbf{k}_1 \cdot \mathbf{X}) + \mathbf{U}^{(2)} \cos(\omega_2 t - \mathbf{k}_2 \cdot \mathbf{X}) \quad (35)$$

where  $\omega_1$  and  $\omega_2$  are the angular frequencies of the two incident waves,  $\mathbf{k}_1$  and  $\mathbf{k}_2$  are the corresponding wave vectors, and  $\mathbf{U}^{(1)}$  and  $\mathbf{U}^{(2)}$  are the wave amplitudes.  $\mathbf{k}_i = k_i \mathbf{p}$  ( $i=1,2$ ) where  $k_i$  is the wavenumber and  $\mathbf{p}$  is the unit vector in the direction of propagation. The wavenumbers of the waves can be found from:

$$k_i = \frac{\omega_i}{c} \quad (36)$$

where the index  $i$  corresponds to the two incident waves and  $c$  is the speed of sound of the wave at mixing. The solution to the wave equation is valid for both longitudinal and transverse waves. Therefore, the incident waves can be of longitudinal or shear mode, and the corresponding wave velocity should be used. The definitions for the wave vectors, angular frequencies, and amplitudes of the participating waves are given in Figure 7.

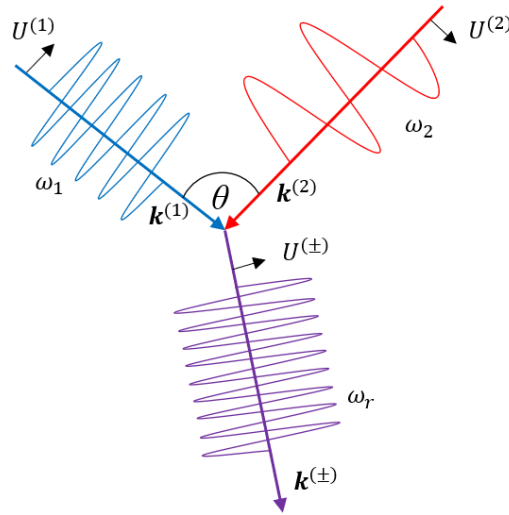


Figure 7: Mixing of two incident waves (1,2) and the resultant scattered wave

Following the assumed form of the solution, the solution to the nonlinear wave equation (Equation 29) is found to be:

$$L_i(u^{(h)}) + L_i(u^{(p)}) = G_i(u^{(h)}) + G_i(u^{(p)}) \quad (37)$$

where the differential operator  $L_i$  is defined as the left-hand side of Equation 29:

$$L_i = \rho \frac{\partial^2 u_i}{\partial t^2} - \mu \frac{\partial^2 u_i}{\partial X_k \partial X_k} - (\lambda + \mu) \frac{\partial^2 u_i}{\partial X_l \partial X_l} \quad (38)$$

From the presumed solution of the nonlinear wave equation,  $G_i(u^{(p)}) \approx 0$  as the magnitude of  $u^{(p)}$  is much smaller than  $u^{(h)}$  and thus will trend towards zero due to the higher order terms. The first term in Equation 38 is the solution to the homogenous equation therefore:

$$L_i(u^{(h)}) = 0 \quad (39)$$

This leaves the proposed solution to the nonlinear wave equation to be:

$$L_i(u^{(p)}) = G_i(u^{(h)}) \quad (40)$$

where  $G_i(u^{(h)})$  from Equation 30 is defined in 2D as:

$$G_i(u^{(h)}) = b_i^+ \sin(\omega_+ t - k^+ \cdot \mathbf{X}) + b_i^- \sin(\omega_- t - k^- \cdot \mathbf{X}) \quad (41)$$

The amplitudes  $b_i^+$  and  $b_i^-$  are defined as [17], [28]:

$$\begin{aligned}
\mathbf{b}^\pm = & \frac{-U^{(1)}U^{(2)}}{2} \left[ \left( \mu + \frac{n}{4} \right) \{ (\hat{\mathbf{U}}^{(1)} \cdot \hat{\mathbf{U}}^{(2)}) (\mathbf{k}^{(2)} \cdot \mathbf{k}^{(2)}) \mathbf{k}^{(1)} \pm (\hat{\mathbf{U}}^{(1)} \cdot \hat{\mathbf{U}}^{(2)}) (\mathbf{k}^{(1)} \cdot \mathbf{k}^{(1)}) \mathbf{k}^{(2)} \right. \\
& + (\hat{\mathbf{U}}^{(2)} \cdot \mathbf{k}^{(1)}) (\mathbf{k}^{(2)} \cdot \mathbf{k}^{(2)}) \hat{\mathbf{U}}^{(1)} \pm (\hat{\mathbf{U}}^{(1)} \cdot \mathbf{k}^{(2)}) (\mathbf{k}^{(1)} \cdot \mathbf{k}^{(1)}) \hat{\mathbf{U}}^{(2)} \\
& \left. \pm (\hat{\mathbf{U}}^{(2)} \cdot \mathbf{k}^{(1)}) (\mathbf{k}^{(1)} \cdot \mathbf{k}^{(2)}) \hat{\mathbf{U}}^{(1)} \pm 2(\hat{\mathbf{U}}^{(1)} \cdot \mathbf{k}^{(2)}) (\mathbf{k}^{(1)} \cdot \mathbf{k}^{(2)}) \hat{\mathbf{U}}^{(2)} \right] \\
& \left( \lambda + \mu - \frac{n}{4} + m \right) \{ (\hat{\mathbf{U}}^{(1)} \cdot \hat{\mathbf{U}}^{(2)}) (\mathbf{k}^{(1)} \cdot \mathbf{k}^{(2)}) \mathbf{k}^{(1)} \pm (\hat{\mathbf{U}}^{(1)} \cdot \hat{\mathbf{U}}^{(2)}) (\mathbf{k}^{(1)} \cdot \mathbf{k}^{(1)}) \mathbf{k}^{(2)} \\
& + (\hat{\mathbf{U}}^{(2)} \cdot \mathbf{k}^{(2)}) (\mathbf{k}^{(1)} \cdot \mathbf{k}^{(2)}) \hat{\mathbf{U}}^{(1)} \pm (\hat{\mathbf{U}}^{(1)} \cdot \mathbf{k}^{(1)}) (\mathbf{k}^{(1)} \cdot \mathbf{k}^{(2)}) \hat{\mathbf{U}}^{(2)} \} \quad (42) \\
& \left( \lambda - \frac{n}{2} + m \right) \{ \pm (\hat{\mathbf{U}}^{(2)} \cdot \mathbf{k}^{(2)}) (\mathbf{k}^{(1)} \cdot \mathbf{k}^{(1)}) \hat{\mathbf{U}}^{(1)} \pm (\hat{\mathbf{U}}^{(1)} \cdot \mathbf{k}^{(1)}) (\mathbf{k}^{(2)} \cdot \mathbf{k}^{(2)}) \hat{\mathbf{U}}^{(2)} \} \\
& \left( m - \frac{n}{4} \right) \{ (\hat{\mathbf{U}}^{(2)} \cdot \mathbf{k}^{(2)}) (\hat{\mathbf{U}}^{(1)} \cdot \mathbf{k}^{(2)}) \mathbf{k}^{(1)} \pm (\hat{\mathbf{U}}^{(2)} \cdot \mathbf{k}^{(2)}) (\hat{\mathbf{U}}^{(1)} \cdot \mathbf{k}^{(1)}) \mathbf{k}^{(2)} \\
& \pm (\hat{\mathbf{U}}^{(1)} \cdot \mathbf{k}^{(2)}) (\hat{\mathbf{U}}^{(2)} \cdot \mathbf{k}^{(1)}) \mathbf{k}^{(1)} \pm (\hat{\mathbf{U}}^{(1)} \cdot \mathbf{k}^{(2)}) (\hat{\mathbf{U}}^{(2)} \cdot \mathbf{k}^{(1)}) \mathbf{k}^{(2)} \} \\
& \left( \lambda - \frac{n}{2} + m \right) \{ \pm (\hat{\mathbf{U}}^{(1)} \cdot \mathbf{k}^{(1)}) (\hat{\mathbf{U}}^{(2)} \cdot \mathbf{k}^{(2)}) \mathbf{k}^{(1)} \pm (\hat{\mathbf{U}}^{(1)} \cdot \mathbf{k}^{(1)}) (\hat{\mathbf{U}}^{(2)} \cdot \mathbf{k}^{(2)}) \mathbf{k}^{(2)} \}
\end{aligned}$$

Reduced expression for  $\mathbf{b}^\pm$  exist depending on the form of the two incident waves. A specified solution to Equation 40 which is situationally dependent thereby reducing  $\mathbf{b}^\pm$  is of the form:

$$u_i^{(p)} = a_i^+ \sin(\omega_+ t - k_j^+ \cdot \mathbf{X}_j) + a_i^- \sin(\omega_- t - k_j^- \cdot \mathbf{X}_j) \quad (43)$$

where  $a_i^+$  and  $a_i^-$  are situation dependent amplitudes of  $\mathbf{b}^\pm$ . This solution is used in Equation 40 for which the derivatives are evaluated leading to the following linear system of equations:

$$\rho \mathbf{A}^\pm \mathbf{a}^\pm = \mathbf{b}^\pm \quad (44)$$

where  $\mathbf{A}^\pm$  is defined as

$$\mathbf{A}^\pm = \begin{bmatrix} -\omega_\pm^2 + c_L^2 k_1^{\pm 2} + c_T^2 k_2^{\pm 2} & (c_L^2 - c_T^2) k_1^\pm k_2^\pm \\ (c_L^2 - c_T^2) k_1^\pm k_2^\pm & -\omega_\pm^2 + c_L^2 k_2^{\pm 2} + c_T^2 k_1^{\pm 2} \end{bmatrix} \quad (45)$$

When the solution to the linear system of equations, Equation 44, does not exist, the form of Equation 43 cannot be used to define the resultant wave. Instead, the resultant wave is defined by the volume of interaction and is called the scattered or mixed wave. In all other cases, the resultant solution is a diffracted wave. For resonance to occur (i.e. no solution to the linear system of equations), the following expressions must be true. First,  $\mathbf{b}^\pm$  must not be contained within  $\mathbf{A}^\pm$ .

$$\text{rank}(\mathbf{A}^\pm | \mathbf{b}^\pm) \neq \text{rank}(\mathbf{A}^\pm) \quad (46)$$

Second, no trivial solutions to Equation 44 can exist:

$$\det(\mathbf{A}^\pm) = c_L^2 c_T^2 \left( k_j^\pm k_j^\pm - \frac{\omega_\pm}{c_L^2} \right) \left( k_j^\pm k_j^\pm - \frac{\omega_\pm}{c_T^2} \right) = 0 \quad (47)$$

The third condition defines that the scattered or mixed wave must propagate according to:

$$\left(\frac{\omega_1 \pm \omega_2}{c^{(r)}}\right)^2 = \|k^{(1)} \pm k^{(2)}\| \quad (48)$$

This equation is defined as the resonance condition and is what defines the amplitude of the scattered wave that is proportional to the volume of interaction. The resonance condition can be used to define a necessary incident angle for the two mixing waves, given the types of participating waves:

$$\begin{aligned} \|k^{(1)} \pm k^{(2)}\| &= k^{(1)2} + k^{(2)2} \pm 2(k^{(1)} \cdot k^{(2)}) \\ &= \frac{\omega_1^2}{c^{(1)}} + \frac{\omega_2^2}{c^{(2)}} \pm 2 \frac{\omega_1 \omega_2}{c^{(1)} c^{(2)}} \cos(\theta) \end{aligned} \quad (49)$$

From this, the necessary resonance angle of incidence between the two mixing waves is defined as:

$$\cos(\theta) = \pm \frac{1}{2} \left[ \frac{c^{(2)}}{c^{(1)}} \frac{1}{a} + \frac{c^{(2)}}{c^{(1)}} a - \frac{c^{(1)} c^{(2)}}{c^{(r)}} \left( \frac{1}{a} + a \pm 2 \right) \right] \quad (50)$$

where  $a$  is defined as the frequency ratio  $\frac{\omega_2}{\omega_1}$  and  $c$  is the acoustic velocity corresponding to the material of each wave. In addition to the required mixing angle condition, the limits of the cosine function can be used to limit the range of the frequency ratio,  $a$ , such that:

$$-1 < \cos(\theta) < 1 \quad (51)$$

The frequency and direction of the scattered wave are determined from the initial two elastic waves:

$$\omega_r = \omega_1 \pm \omega_2 \quad (52)$$

$$\mathbf{k}_r = \mathbf{k}_1 \pm \mathbf{k}_2 \quad (53)$$

From the initial work of Jones and Kobett [28], five possible resonant interaction cases are defined. Table 1 is adopted from this work with the following definitions of frequency ratio and speed of sound ratio:

$$a = \omega_2/\omega_1 \quad (54)$$

$$c = c_T/c_L \quad (55)$$

$c_T$  is the transverse, or shear wave speed and  $c_L$  is the longitudinal wave speed.

Table 1: Resonance Conditions for Noncollinear Interactions [28]

Initial Waves	Resonant Wave Type	$\omega_r$	$\mathbf{k}_r$	$\cos \theta$	Frequency limits
Two shear	Longitudinal	$\omega_1 + \omega_2$	$\mathbf{k}_1 + \mathbf{k}_2$	$c^2 + \left[ \frac{(c^2 - 1)(a^2 + 1)}{2a} \right]$	$\frac{1 - c}{1 + c} < a < \frac{1 + c}{1 - c}$
Two longitudinal	Shear	$\omega_1 - \omega_2$	$\frac{(\mathbf{k}_1 - \mathbf{k}_2)}{\omega_1 - \omega_2}$	$\frac{1}{c^2} + \left[ \frac{(c^2 - 1)(a^2 + 1)}{2ac^2} \right]$	$\frac{1 - c}{1 + c} < a < \frac{1 + c}{1 - c}$
One longitudinal and one shear	Longitudinal	$\omega_1 + \omega_2$	$\mathbf{k}_1 + \mathbf{k}_2$	$c + \left[ \frac{a(c^2 - 1)}{2c} \right]$	$0 < a < \frac{2c}{1 - c}$
One longitudinal and one shear	Longitudinal	$\omega_1 - \omega_2$	$\frac{(\mathbf{k}_1 - \mathbf{k}_2)}{\omega_1 - \omega_2}$	$c + \left[ \frac{a(c^2 - 1)}{2c} \right]$	$0 < a < \frac{2c}{1 + c}$
One longitudinal and one shear	Shear	$\omega_1 - \omega_2$	$\frac{(\mathbf{k}_1 - \mathbf{k}_2)}{\omega_1 - \omega_2}$	$\frac{1}{c} + \left[ \frac{(c^2 - 1)}{2ac} \right]$	$\frac{1 - c}{2} < a < \frac{1 + c}{2}$

The work of Jones and Kobett [28] does not consider the polarization of primary shear waves. Korneev and Demčenko [30] expand upon this topic to differentiate shear waves polarized in the interaction plane (SV) and orthogonal to the interaction plane (SH).

Table 3 compares the 9 different input cases (L, SV, SH) with six total resultant mixed waves ( $[L, SV, SH]_{\omega_1+\omega_2}$  and  $[L, SV, SH]_{\omega_1-\omega_2}$ ). Each combination is marked with a symbol from the key in Table 2. Later work shows that additional conditions are needed depending on the type of resonance wave generated [31].

Table 2: Key for Table 3

=	Possible only for collinear mixing
x	Possible if conditions are met
$\bar{x}$	Possible if conditions are met with waves propagating in opposite direction
O	Polarization restriction
	Interaction is not possible

Table 3: Combinations of Mixing Waves in Isotropic Solid

N	Interaction Waves	Scattered Waves					
		$\omega_r = \omega_1 + \omega_2$			$\omega_r = \omega_1 - \omega_2$		
		L	SV	SH	L	SV	SH
1	L( $\omega_1$ ) and L( $\omega_2$ )	=			=	$\bar{x}$	O
2	L( $\omega_1$ ) and SV( $\omega_2$ )	$\bar{x}$			X	$\bar{x}$	O
3	SV( $\omega_1$ ) and L( $\omega_2$ )	x					
4	SV( $\omega_1$ ) and SV( $\omega_2$ )	$\bar{x}$	O	O		O	O
5	SH( $\omega_1$ ) and SH( $\omega_2$ )	$\bar{x}$	O	O		O	O
6	L( $\omega_1$ ) and SH( $\omega_2$ )	O			O	O	$\bar{x}$
7	SH( $\omega_1$ ) and L( $\omega_2$ )	O					
8	SH( $\omega_1$ ) and SV( $\omega_2$ )	O	O	O		O	O
9	SV( $\omega_1$ ) and SH( $\omega_2$ )	O	O	O		O	O

### 2.6.2 Rational for Selected Mixing Condition

The nonlinear wave mixing measurements in this work are based on the mixing of two shear waves as listed in the first entry in Table 1. The resultant mixed wave is a longitudinal wave which is easier to measure with a receiving piezoelectric transducer. Furthermore, the mixed wave travels in an easily accessible manner ( $\mathbf{k}_r = \mathbf{k}_1 + \mathbf{k}_2$ ). The general form of experimental setups in this work consists of two emitting waves on one

side of a test object. Therefore, the mixed wave will propagate away from the two emitting waves and toward the opposing side of the test specimen. As discussed in future sections based on the measurement of large concrete structures, a nonlinear mixed wave setup can still be single sided by measuring the reflection of the mixed wave off the bottom surface. A key equation given in Table 1 is for the mixing angle required for resonance condition which is restated below:

$$\cos(\theta_{mix}) = c^2 + \left[ \frac{(c^2 - 1)(a^2 + 1)}{2a} \right] \quad (56)$$

Korneev and Demčenko [30] first explored the effect of incident wave polarization on the outcome of the resultant scattered wave. In the case of two incident shear waves mixing, only two possible polarization combinations are possible. From Table 3, the following two pairs [(SV), (SV)] and [(SH), (SH)] can result in the generation of a third scattered wave. (SV) waves are shear waves polarized in the plane of the two incident wave vectors  $\mathbf{k}^{(1)}$ ,  $\mathbf{k}^{(2)}$ . (SH) waves are shear waves polarized orthogonal to the plane of the two incident wave vectors. All other combinations involving shear waves are described by Korneev and Demčenko as restricted by polarization.

Shear waves produced by mode conversion from longitudinal waves at the wedge/specimen surface are (SV) polarized. This restriction on the generation of shear waves from longitudinal transducers led to the use of the [(SV), (SV)] polarization case for two incident shear waves. Shear wave transducers can generate incident waves with either polarization and therefore both polarization combinations could be used for nonlinear wave mixing [17]. However, in practice, generating sufficiently large amplitude incident shear waves with a shear transducer can be difficult.

For both permissible polarization resonance conditions, the amplitude of the mixed wave has the following form [17], [30]:

$$\mathbf{U}^+ = \frac{(\mathbf{b}^+ \cdot \hat{\mathbf{k}}^+)}{4\pi c_L^2 \rho_0 r} V \hat{\mathbf{k}}^+ \quad (57)$$

where  $\mathbf{b}^+$  is defined by Equation 42, and  $r$  is the propagation path length of the scattered wave from the mixing volume to the measurement point. When only considering the [(SV), (SV)] polarization combination, Equation 42 can be evaluated with the following geometric definitions which are categorized in Table 4.

Table 4: Geometric Definitions for the Evaluation of Equation 42 for Two in Plane Shear Waves

$\mathbf{k}^{(1)} \cdot \mathbf{k}^{(1)} = \frac{\omega_1^2}{c_T^2}$	$\mathbf{k}^{(2)} \cdot \mathbf{k}^{(2)} = \frac{\omega_2^2}{c_T^2}$	$\mathbf{k}^{(1)} \cdot \mathbf{k}^{(2)} = \frac{\omega_1 \omega_2}{c_T^2} \cos \theta$
$\hat{\mathbf{U}}^{(1)} \cdot \hat{\mathbf{U}}^{(1)} = 1$	$\hat{\mathbf{U}}^{(2)} \cdot \hat{\mathbf{U}}^{(2)} = 1$	$\hat{\mathbf{U}}^{(1)} \cdot \hat{\mathbf{U}}^{(2)} = \cos \theta$
$\hat{\mathbf{U}}^{(1)} \cdot \mathbf{k}^{(2)} = 0$		$\hat{\mathbf{U}}^{(2)} \cdot \mathbf{k}^{(2)} = 0$
$\hat{\mathbf{U}}^{(1)} \cdot \mathbf{k}^{(1)} = \frac{\omega_2}{c_T} \cos \left( \theta + \frac{\pi}{2} \right)$	$\hat{\mathbf{U}}^{(2)} \cdot \mathbf{k}^{(1)} = \frac{\omega_1}{c_T} \cos \left( \theta - \frac{\pi}{2} \right)$	
$\mathbf{U}^{(1)} = \begin{bmatrix} 0 & -1 \\ 1 & 0 \end{bmatrix} \mathbf{k}^{(1)}$	$\mathbf{U}^{(2)} = \begin{bmatrix} \sin \theta & -\cos \theta \\ \cos \theta & \sin \theta \end{bmatrix} \mathbf{k}^{(1)}$	
$\mathbf{k}^{(2)} = \begin{bmatrix} \cos \theta & \sin \theta \\ -\sin \theta & \cos \theta \end{bmatrix} \mathbf{k}^{(1)}$		

Following the evaluation of  $\mathbf{b}^+$  under the geometric constraints for mixing two in plane shear waves a simplified expression is found as:

$$\mathbf{b}^+ = -\frac{U^{(1)}U^{(2)}\omega_1\omega_2}{4c_T^2}[\lambda + \mu + \cos(2\theta)(\lambda + 3\mu + 2m)]\mathbf{k}^+ \quad (58)$$

which can be used to specify Equation 57 under the condition of two in plane shear waves.

The evaluation of this substitution is:

$$U^+ = -\frac{U^{(1)}U^{(2)}\omega_1^3V}{16\pi r\rho_0} \frac{1}{c_L^3c_T^3} [(\lambda + 2\mu)\{(1 - c^2)(a + a^2)\} \\ + (\lambda + 3\mu + 2m) \left\{ 2 \left( \left( a + \frac{1}{a} \right) \frac{c^2 - 1}{2} + c^2 \right)^2 - 1 \right\}] \quad (59)$$

Equation 59 is the expression for the amplitude of the third wave generated by the nonlinear mixing of two in plane shear waves. This incident wave combination is used in this work and for the development of the phased array based technique. Equation 59 contains a few terms that shows the value of this mixing technique for the characterization of porosity in additively manufactured metals.  $\rho_0$  is the density of the undeformed material which is inherently connected to the porosity percentage. Increase in porosity leads to a decrease in density which will, holding all other terms constant, cause an increase in the amplitude of the mixed wave. Additionally contained within Equation 59 is Murnaghan constant ( $m$ ) which is sensitive to the material state.

### 2.6.3 *State of the Art in Nonlinear Wave Mixing*

In the cases of resonance, the amplitude of the mixed wave depends on the third-order elastic constants (TOEC) [28], [29]. This relation allows for the measurement of

TOECs by the mixing of two waves as first shown by Rollins [32]. Early microstructural indicators of material state and damage can be detected when nonlinear elasticity terms are included in material descriptions. This provides a viable avenue for the use of nonlinear wave mixing for microstructural characterization.

The seminal work showing the sensitivity of the amplitude of the mixed wave to plasticity and fatigue damage was conducted by Croxford et al [33]. This confirmed the relation between the contributing TOECs to the mixed wave and the material state. Subsequent works in this area have focused on refinements of experimental setup for improvements of sensitivity and resolution [34]. Rudimentary scanning capabilities have been implemented by varying the separation of the emitting transducers [35]. In such configurations, a mapping of material nonlinearity is possible, but requires the recoupling of the emitting transducers for each scanning point. Scanning capabilities have been implemented through the use of immersion techniques in which two transmitting water-coupled transducers and a receiving water-coupled transducer are able to translate together and receive the mixed wave signal at multiple mixing locations [34]. Limitations to this setup may arise when specimen constraints prohibit complete submersion in water. Physical aging of PVC polymers has been investigated with nonlinear wave mixing techniques, showing the sensitivity of this work to degradation of the polymer from heat and use [36]–[38].

Extensive work has gone into the use of noncollinear nonlinear wave mixing techniques for the characterization and inspection of cracks and bonds. This includes the characterization [39] and orientation analysis [40] of fatigue cracks. Kissing bonds are sources of high nonlinearity that are well characterized by this technique [41]–[43].

Similarly, interface inspection of titanium diffusion bonds is improved with nonlinear wave mixing techniques [44]. Cracks [45] and imperfect interfaces [46] have also been used as sources of nonlinearity in simulations and models of mixing.

Sharing similarities with the aforementioned noncollinear bulk wave techniques, collinear and guided wave mixing setups have also been used for NDE applications. Collinear setups have been used to measure the acoustic nonlinearity parameter common in other nonlinear ultrasound techniques and is separate from the material nonlinearity measured in many mixing setups [47], [48]. The mixing of collinear propagating sinusoidal pulses shows that the amplitude of the mixed pulse is proportional to the mixing zone size as determined by the spatial lengths of the initial pulses [49]. Scanning setups have been demonstrated with collinear mixing by varying the timing of the emitting pulses, which changes the area of interaction between the pulses [50]. Mixing techniques using Lamb [51]–[54], and Rayleigh waves [55] have also been developed.

There are currently no ultrasonic techniques capable of scanning and mapping localized internal micro- and nano- scale damage. Localized values of damage are currently only nondestructively obtainable with expensive computed tomography scanning. The theorization and development of a phased array based nonlinear wave mixing technique can provide location specific characterization of damage with the cost, speed, and ease of use benefits common to many ultrasound based measurements.

#### *2.6.4 Benefits of Mixing Technique*

In comparison to the many nonlinear ultrasonic techniques reliant on second harmonic generation, nonlinear mixing provides a few key advantages. The amplitude of the mixed wave is dependent on the nonlinearity within the mixing area [33], [56]. This

spatial selectivity provides two individual benefits. The first is an increase in isolation from system nonlinearity as the amplitude of the mixed wave does not depend on the nonlinearities of the system setup. The second is the ability to map regions of nonlinearity which can be used to assess inhomogeneous sources of damage.

The introduction of phased arrays to nonlinear wave mixing in this work emphasizes the importance of localized value of nonlinearity. With a phased array-based technique, multiple localized values of material nonlinearity can be obtained at specific desired location without moving or recoupling the emitting transducers. This ability to scan localized volumes can be beneficial in practical application. If only a small portion of a test area is of concern, a scanning routine with phased arrays can be developed which limits the amount of time and resources dedicated to the study of unimportant regions in a material.

In some of the possible mixing combinations in Table 3, the mode of the mixed wave is different from the mode of the incident waves in the material [28]. Again, this may be used to isolate from other sources of nonlinearity, including the generation of higher harmonics from the incident waves outside of the mixing area [33], [56]. In practice, as discussed in the findings of this work, modal selectivity is difficult to apply as the generation of the incident waves in the material is often accompanied by unwanted modes also entering the specimen. Looking again at the possible mixing combinations [28], if incident waves of differing frequencies are selected, a mixed wave away from the higher harmonics of the initial waves can be generated. This frequency selectivity could be used to separate the frequency of the mixed wave from nonlinearities of the incident wave occurring at higher harmonics.

In the case of noncollinear mixing, the propagation of the mixed wave can occur in different directions depending on the resonance condition [28]. Common cases include the forward propagation in the direction combined from the two incident waves. Depending on the geometry, this direction may result in a receiver placement that is spatially isolated from receiving non-mixed nonlinearities from the incident waves. Other mixing cases can result in a “backward” propagation of the mixed wave allowing for single sided measurements without the reliance on reflections within the specimen.

Mixing techniques are also of particular benefit in heterogeneous and multiphase materials like concrete [57]. In such materials, the highly dispersive nature makes measurement at high frequencies difficult. The propagation path of the higher frequency mixed wave does not include the propagation distance from the emitting transducers to the point of mixing. Instead, the propagation path is limited from the region of mixing to the receiver, thereby reducing the effects of the highly attenuative material on the mixed wave. The benefits of this application are shown in Section 4.4.2 on the measurement of damage in cement-based materials.

### *2.6.5 Four-Way Polarity Flipping*

A useful technique applied in this work is the four-way polarity flipping method [34]. This technique is used to suppress components of the received signal that are generated from nonlinear sources not associated with wave mixing. These unwanted nonlinear contributions to the measured signal may include the generation of higher harmonics of spurious waves inserted into the material that have similar temporal and geometric arrivals to the receiver. While these effects could be suppressed using the advantages described in Section 4.5, common limitations from equipment prevent the

application of frequency selectivity. For example, the mixing of two waves of frequencies 4.5 MHz and 5.5 MHz or of two waves of equal 5 MHz frequency would generate a mixed wave of frequency 10 MHz. Second harmonic generation of the incident waves would be between 9 MHz, 11 MHz, or 10 MHz respectively. These frequencies may be difficult or impossible to separate from the mixed wave frequency.

To implement the four-way polarity flipping technique, four independent measurements containing the four possible polarity combinations (positive-positive:  $pp$ , positive-negative:  $pn$ , negative-positive:  $np$ , negative-negative:  $nn$ ) of the two incident waves are measured. An example of the input wave with both positive polarity ( $P = A \sin(\omega t)$ ) in red and negative polarity ( $P = -A \sin(\omega t)$ ) in blue is shown in Figure 8. An illustration of the four independent measures and the corresponding response is shown in Figure 9.

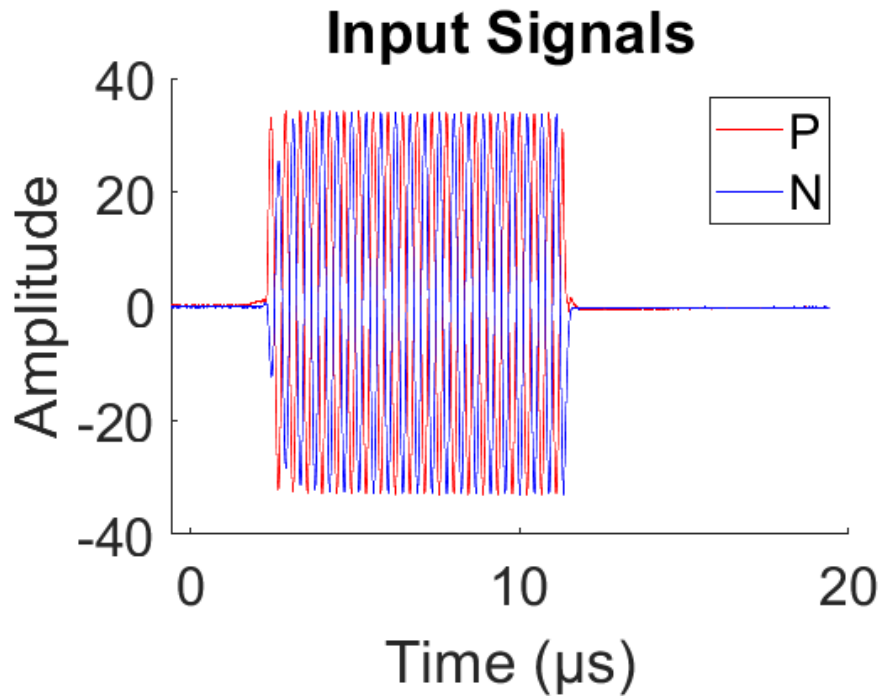


Figure 8: Example of positive and negative polarity of input wave

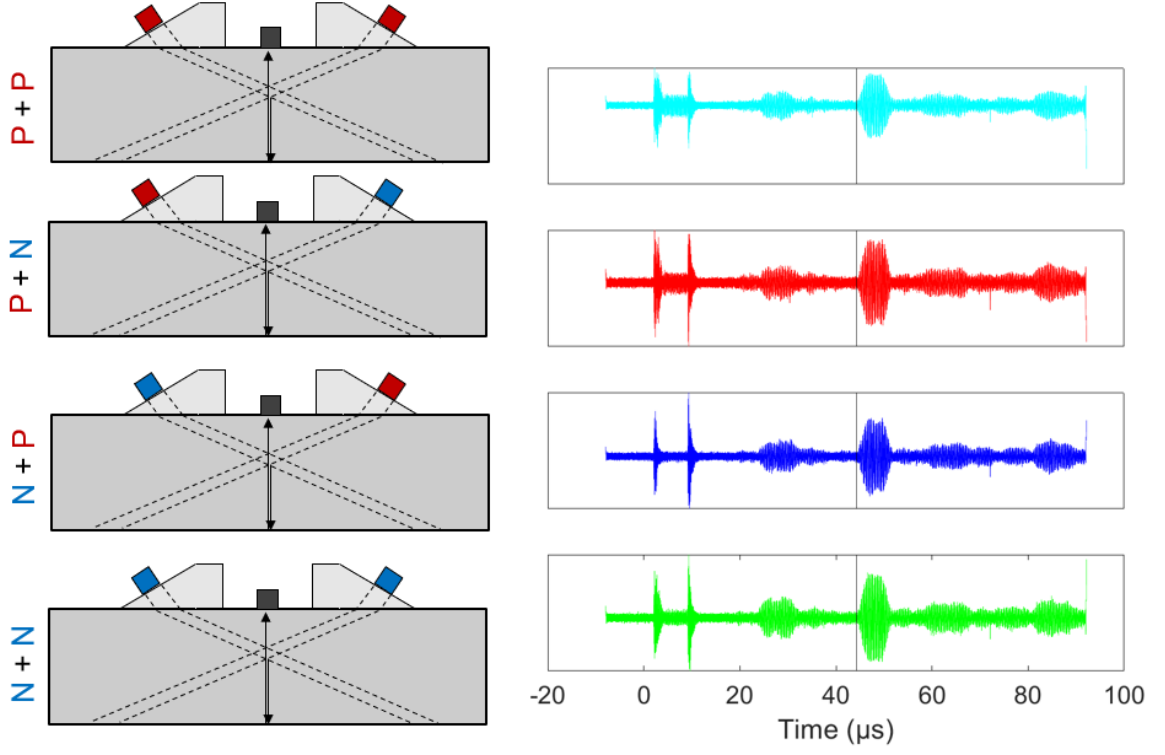


Figure 9: Illustration of the four polarity combination measurements

In the example of two incident shear waves mixing, the four polarity combinations (left hand side) and the resultant received signals (right hand side) are defined below:

$$\begin{aligned}
 pp \text{ case: } \quad & (A_0^{\omega_1}, B_0^{\omega_2}) \rightarrow \eta A_1 B_1 \\
 & + (A_1^{\omega_1}, B_1^{\omega_2}) + (C_1^{\omega_1}, D_1^{\omega_2}) +, \dots \\
 & + (\alpha(A_1^{\omega_1})^2, \beta(B_1^{\omega_2})^2) + (\gamma(C_1^{\omega_1})^2, \delta(D_1^{\omega_2})^2), \dots
 \end{aligned} \tag{60}$$

$$\begin{aligned}
 pn \text{ case: } \quad & (A_0^{\omega_1}, -B_0^{\omega_2}) \rightarrow -\eta A_1 B_1 \\
 & + (A_1^{\omega_1}, -B_1^{\omega_2}) + (C_1^{\omega_1}, -D_1^{\omega_2}) +, \dots \\
 & + (\alpha(A_1^{\omega_1})^2, \beta(-B_1^{\omega_2})^2) + (\gamma(C_1^{\omega_1})^2, \delta(-D_1^{\omega_2})^2), \dots
 \end{aligned} \tag{61}$$

$$\begin{aligned}
np \text{ case: } \quad & (-A_0^{\omega_1}, B_0^{\omega_2}) \rightarrow -\eta A_1 B_1 \\
& + (-A_1^{\omega_1}, B_1^{\omega_2}) + (-C_1^{\omega_1}, D_1^{\omega_2}) +, \dots \\
& + \left( \alpha (-A_1^{\omega_1})^2, \beta (B_1^{\omega_2})^2 \right) + \left( \gamma (-C_1^{\omega_1})^2, \delta (D_1^{\omega_2})^2 \right), \dots
\end{aligned} \tag{62}$$

$$\begin{aligned}
nn \text{ case: } \quad & (A_0^{\omega_1}, B_0^{\omega_2}) \rightarrow \eta A_1 B_1 \\
& + (-A_1^{\omega_1}, -B_1^{\omega_2}) + (-C_1^{\omega_1}, -D_1^{\omega_2}) +, \dots \\
& + \left( \alpha (-A_1^{\omega_1})^2, \beta (-B_1^{\omega_2})^2 \right) + \left( \gamma (-C_1^{\omega_1})^2, \delta (-D_1^{\omega_2})^2 \right), \dots
\end{aligned} \tag{63}$$

where the terms of the received signal (RHS) following the first term are unwanted signal that are not associated with wave mixing.  $A_0^{\omega_1}$  and  $B_0^{\omega_2}$  are the initial shear waves input into the system at the respective frequencies  $\omega_1$  and  $\omega_2$ .  $A_1$  and  $B_1$  are the received components with the nonlinear parameters  $\alpha$ ,  $\beta$ ,  $\gamma$ , and  $\delta$ . Note, the received signal written in Equations 60-63 include both linear and nonlinear components. The mixed component of the received signal is then found by:

$$\eta A_1 B_1 = \frac{Eq \ 60 - Eq \ 61 - Eq \ 62 + Eq \ 63}{4} \tag{64}$$

From Equation 64, the linear components and non-mixing nonlinear components are eliminated. This technique is found to be highly beneficial in low nonlinear systems.

## 2.7 Phased Arrays

A key component of this work is the application of phased array technology to the wave mixing technique. A significant amount of theory exists in the literature on the study of the acoustic pressure distribution radiated from linear phased arrays [58]. In brief, phased arrays are composed of multiple individual ultrasonic elements separated by a fixed distance or pitch. The geometric definition of a phased array can be seen below in Figure 10. The number of elements and pitch are essential values in determination of the necessary time delays. The specifics of the arrays used in this work are later detailed in Figure 42.

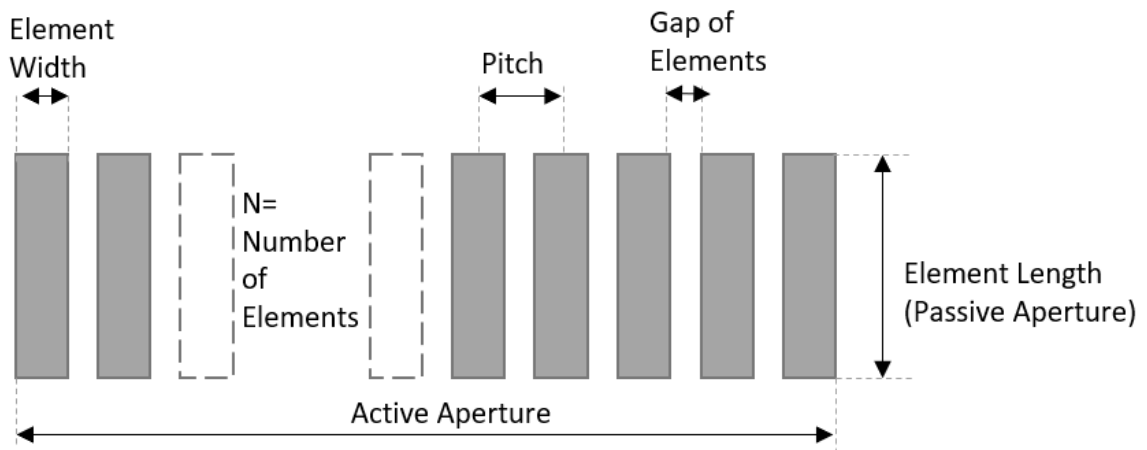


Figure 10: Array geometry definition

### 2.7.1 Beam Steering

A novelty of this work is dependent upon the scanning capabilities provided by phased array emitting transducers. Beam steering is possible by delaying the firing time for subsequent elements such that the effective wave front emanating from the beam is angled in the desired direction. Each element of the phased array is treated as a point source radiating the pressure wave. The effective wave front is created by the superposition of each emitted wave in the far field as shown in the general depiction below:

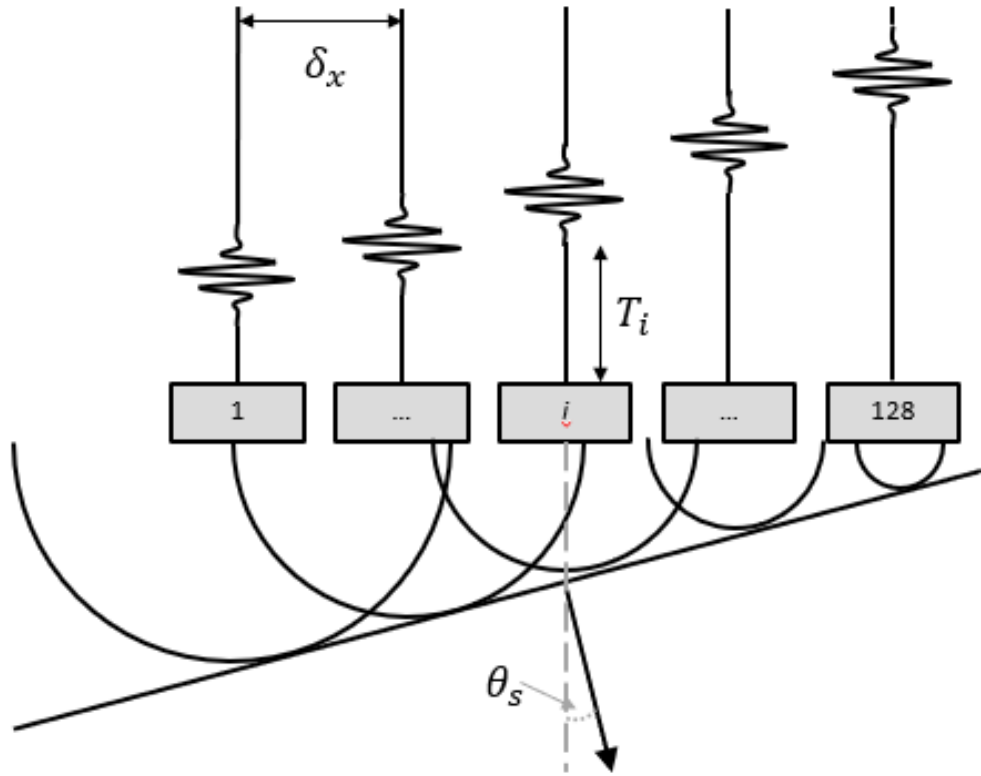


Figure 11: Visualization of beam steering with phased array

For a phased array normal to the material surface, the time delay  $\Delta T_i$  for the  $i$ -th element can be found from:

$$\Delta T_i = \frac{i \times \delta_x \times \sin \theta_s}{c} \quad (65)$$

where  $\delta_x$  is the intra-element pitch,  $\theta_s$  is the desired steering angle, and  $c$  is the wave velocity of the correct mode in the material. This equation is significantly complicated with the introduction of multimodal propagation, multiple materials, emitting angles, focusing algorithms, and side lobe reduction.

To meet the mixing condition of two incident shear waves as described in Table 3 conversion wedges are used to convert the incident longitudinal waves from the phased array into the necessary shear waves. Phased arrays with incident shear waves are rare in industry and are more cost prohibitive in application. The mode conversion principles for a phased array are the same as a single element and the individual phased array elements can be ray traced to model the propagation path from each element. The necessary delay timing for a phased array on a wedge is slightly more complicated.

#### 2.7.1.1 Delay Time of Phased Array on Wedge

The necessary delay time between individual elements of a phased array on a wedge are best determined using ray tracing. [59] The waves emanating from each element is modeled independently. The individual waves combine by superposition principle of acoustics to form the greater wave front emanating from the phased array. The geometric definitions required for this calculation are found in Figure 12.

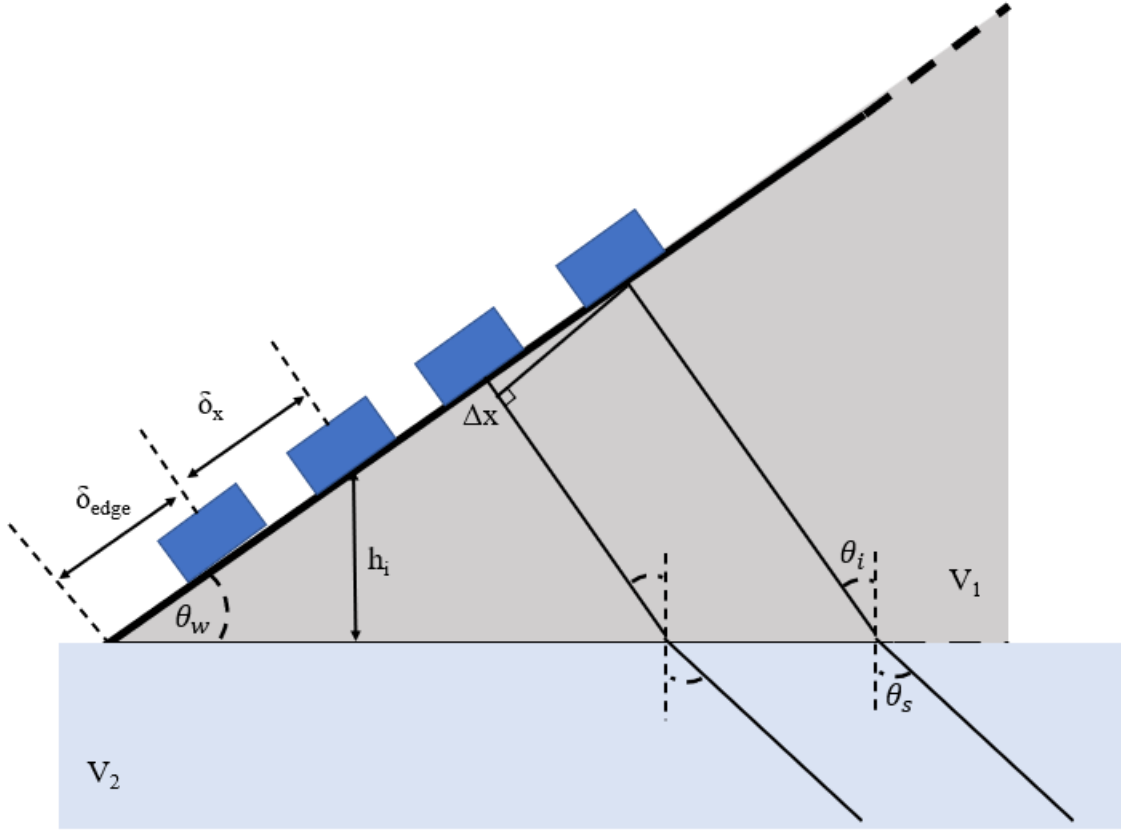


Figure 12: Internal wedge geometry definitions for timing delay of phased array on wedge

The internal angle  $\theta_i$  is found from Snell's law based on the desired propagation angle of the wave front,  $\theta_s$ .

$$\theta_i = \sin^{-1} \left( \frac{C_{L_1}}{C_{T_2}} \sin \theta_s \right) \quad (66)$$

where  $C_{L_1}$  is the longitudinal speed of sound in the wedge and  $C_{T_2}$  is the transverse speed of sound in test material. In the context of this work,  $\theta_s$  is determined by the required angle to meet nonlinear wave mixing conditions.

The necessary timing delay between consecutive firing elements can be found from the difference in propagation path between consecutive elements,  $\Delta x$ .

$$\Delta x = \delta_x \times \sin(\theta_i - \theta_{wedge}) \quad (67)$$

From this, the timing difference required can be found by dividing the travel difference by the longitudinal speed of sound in the material. This can be generalized for each element as:

$$t_i = \frac{(i - 1) \times \delta_x \times \sin(\theta_i - \theta_{wedge})}{C_{L,wedge}} \quad (68)$$

This timing is the needed delay for each subsequent element in order to steer a beam to the desired angle of the effective wave front. For a linear phased array with constant pitch between elements, the timing difference between elements will be constant between each element in the array. The time of element 0 can be nonzero and in this work, it is based on the differences in the propagation time required between wave fronts to reach the mixing point.

The total propagation time of a single ray in the wedge is also of importance. This can be found geometrically; first the vertical height of the emitting element is found as:

$$h_i = (\delta_{edge} + i \times \delta_x) \times \sin(\theta_{wedge}) \quad (69)$$

where  $\delta_{edge}$  is the distance from the first emitting element to the bottom of the wedge.

From this length, the time of flight from one element in the wedge is found as

$$T_i = \frac{h_i}{\cos \theta_i \times C_{L,wedge}} \quad (70)$$

This time is important to account for in order to ensure that the wave fronts from two phased arrays are arriving at the desired mixing point concurrently.

### 2.7.2 Beam Focusing

An often-used ability of phased arrays is beam focusing. By using nonconstant timing differences between elements, the generated wave front from a phased array does not create a planar wave front, but instead can converge onto a point for amplification of the wave. A general depiction of beam focusing from a phased array is shown in Figure 13. The promise of an increased acoustic output at the mixing point is potentially beneficial in this work. However, the wave field from beam focusing is not planar and the mixing conditions described in Section 2.6.1 would not hold.

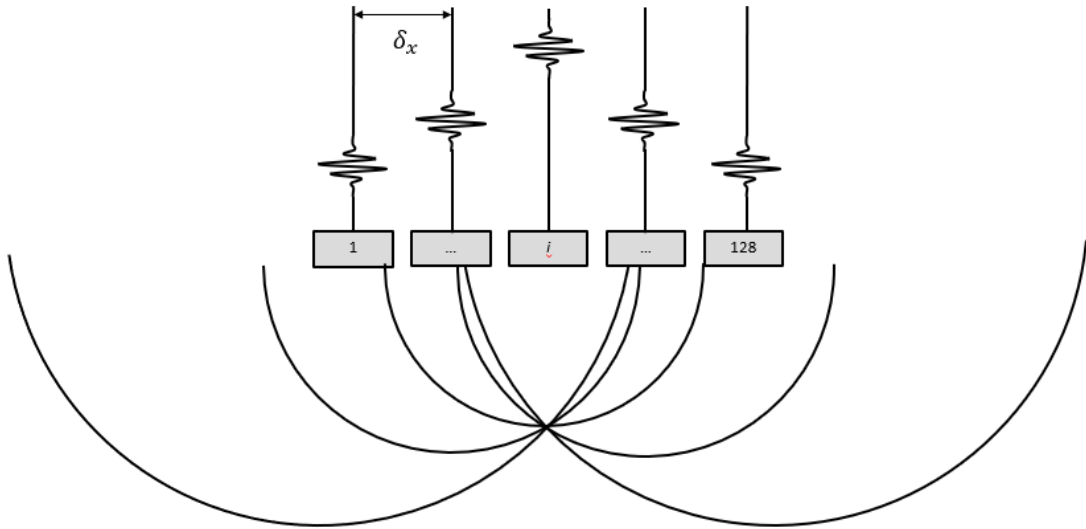


Figure 13: Depiction of beam focusing

## **2.8 Additively Manufactured Metals and Potential Defects**

### *2.8.1 Powder Bed Fusion*

The AM parts studied in this work are manufactured with laser powder bed fusion (L-PBF) methods. Powder bed fusion (PBF) is one of the seven additively manufacturing methods as defined by ASTM F2792 [60]. This manufacturing process is commonly used in industry and as such has been subject to a significant amount of research study. Process induced defects including porosity can affect print quality. These defects can lead to significant changes in mechanical performance.

In this process, a thin layer of powdered metal is spread across the print surface. The powdered metal is rapidly melted and then solidifies. The thermal energy source is subject to change depending on which sub-category of PBF is being used. Electron beam melting uses an electron beam to fuse the metal particles and was first commercialized in 2002 [2]. Selected Laser Sintering (SLS) and Selective Laser Melting (SLM) both use a laser to fuse the metal particles and are as such categorized as Laser Powder Bed Fusion techniques (L-PBF). The AM specimens studied in this work are manufactured with the SLM technique. In each method, following the solidification of the layer, the process is repeated in the subsequent layer with a new layer of powder being spread by the recoater. The orientation of this next layer as defined by the hatch angle ( $47^\circ$  in this work) and is one of the many processing parameters that can affect the print outcome [61]. A visualization of the manufacturing process can be seen in Figure 14.

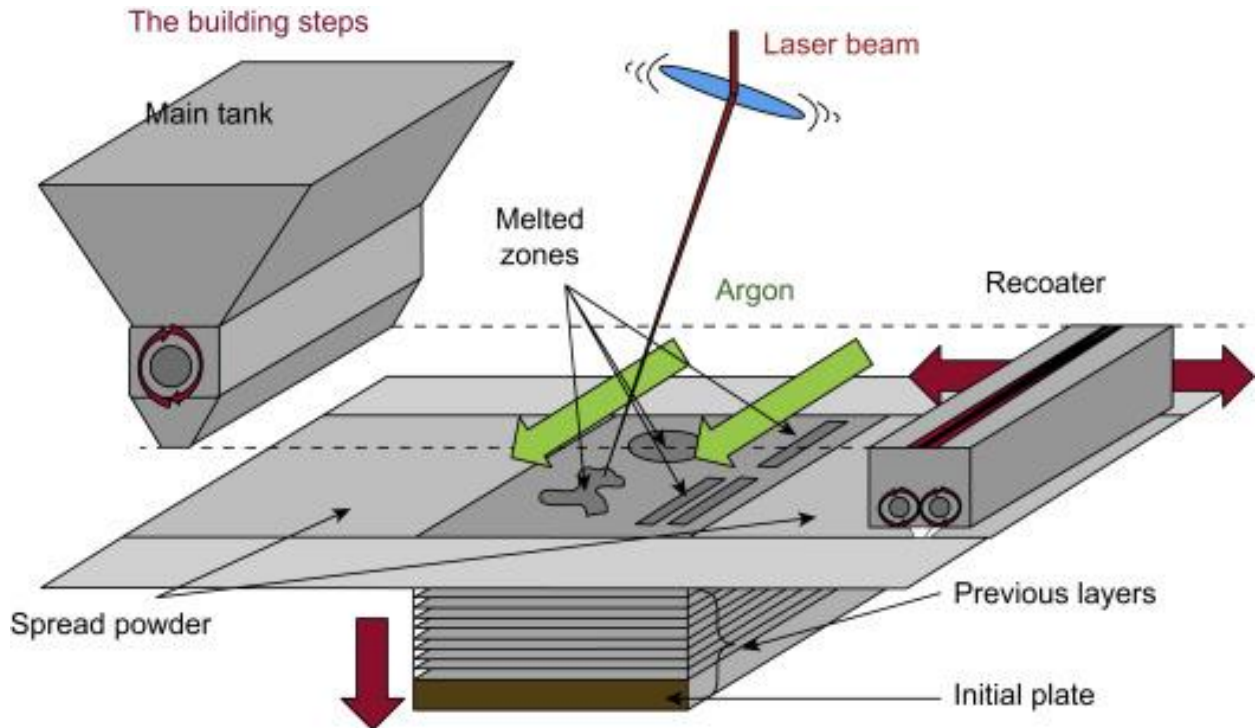


Figure 14: Schematic of laser powder bed fusion [62]

Printing parameters including laser power, layer height, scan speed, scan path, and powder characteristics including size and use cycle can affect material performance. In this work, the laser power and scan speed are of particular interest for their influence on the formation of porosity in AM materials. The interconnectedness between these two parameters is discussed in the next section. However, direct problems with the laser power can in and of itself lead to porosity problems. In Figure 14, the laser beam is shown to be directed by a mirror to the current melt zone. This mirror as aforementioned in the motivation section of this work (Section 1.1) can potentially be damaged with scratches or smudges causing insufficient laser power from reaching the melt pool [7]. Also shown in this image is the argon gas which fills the print chamber which is used to prevent oxidization of solidified layers. Poor ventilation of this inert gas and the potential for vaporized powder in the build chamber can attenuate the laser power.

### 2.8.2 Scanning Speed and Power Relationship

Along the large set of processing parameters which can affect material performance, scanning speed and laser power are two interconnected parameters which can significantly affect the quality of the metal powder fusion. These two parameters are key in determining the energy density at the point of melting the metal powder.

$$E = \frac{P_{laser}}{V_{scan} \times h \times t} \quad (71)$$

where  $E$  is the energy density per volume of material,  $P_{laser}$  is laser power,  $V_{scan}$  is scan speed,  $h$  is the hatch spacing, and  $t$  is the thickness of the layer. Unforeseen decreases in the laser power will cause a decrease in the energy density when the scanning parameters are not adjusted. For a set of printing parameters, there exists an operating window for which the best energy density is applied to the powdered metal. Printing outside of this operating window can lead to an increase in porosity.

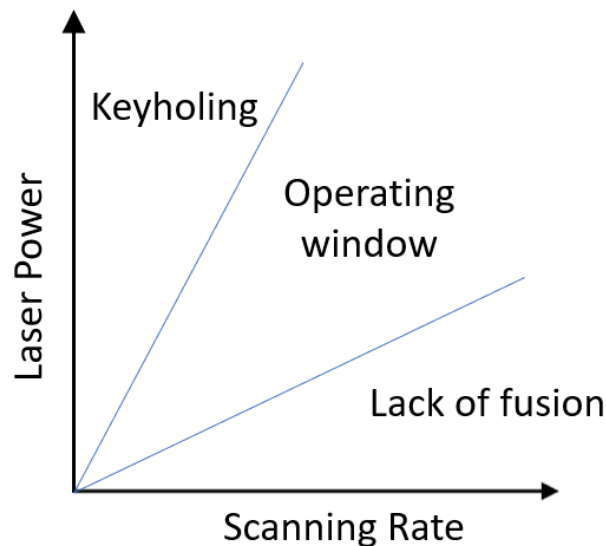


Figure 15: Scanning rate and laser power relationship

### 2.8.3 Porosity

Several potential microstructural defects can occur from variations in laser power during the printing process. Two common types of porosity caused by incorrect processing parameters are irregularly shaped pores caused by lack of fusion and spherical pores caused by keyholing [8]. Both of these processing related flaws are found to be a more dominate source of defects in comparison to gas porosity [8].

#### 2.8.3.1 Lack of Fusion Porosity

Lack of fusion porosity is caused by insufficient melting (too low of energy density) of a new powder layer [9]. This decrease in energy density leads to a smaller melt pool and incomplete melting. The void caused by this is an irregularly shaped pore that is partially filled with unmolten powder particles. Pores of this size are typically 10~20  $\mu\text{m}$  in terms of major axis [63]. A visualization of the formation of lack-of-fusion porosity is seen in Figure 16. As detailed in CHAPTER 3, Specimen 2 and the central layer of the stacked specimen are thought to contain significant amounts of lack-of-fusion porosity. An image showing the irregular shape of lack-of-fusion porosity can be seen in Figure 18(a).

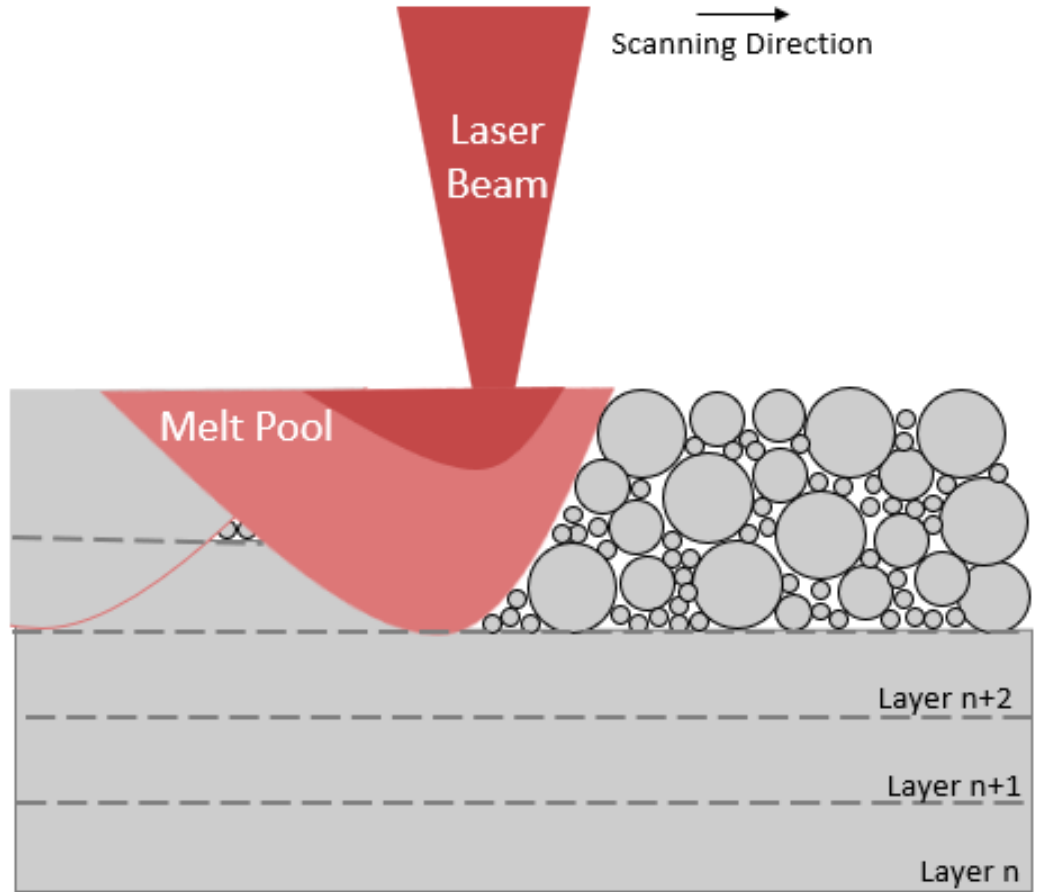


Figure 16: Visualization of lack-of-fusion porosity

### 2.8.3.2 Keyhole Porosity

The effects of too high laser power are similar to the effects of a reduced scanning speed. Large melt pool overlap results from an increase to the energy applied at the melt pool. Keyholing pores are caused by a sufficiently high laser causing evaporation of the metal and the formation of plasma [10]. Metal evaporation causes the development of a vapor cavity with increased laser absorption leading to a deeper depth penetration from the laser and eventual collapse of the cavity [10]. Keyhole pores are typically larger than lack-of-fusion porosity [63]. An image of keyhole porosity can be seen in Figure 18(b). As

detailed in CHAPTER 3, The top layer of the stacked AM specimen in this work is theorized to contain significant amounts of keyholing porosity [64].

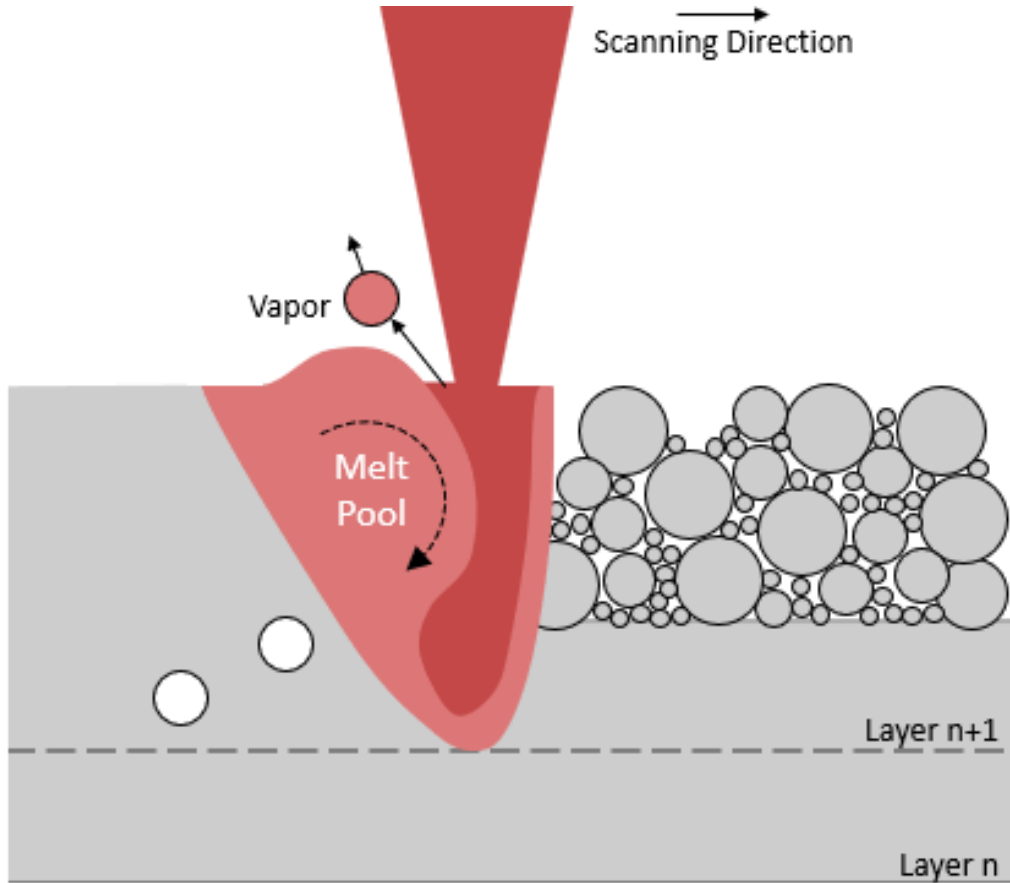
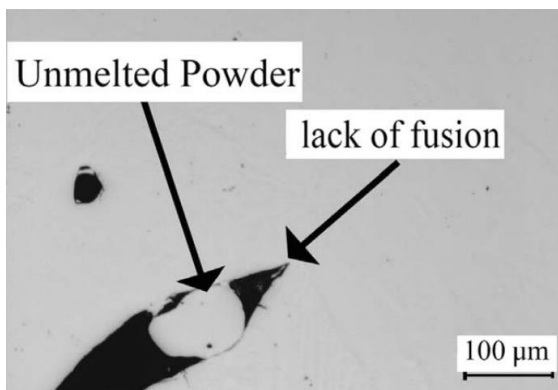
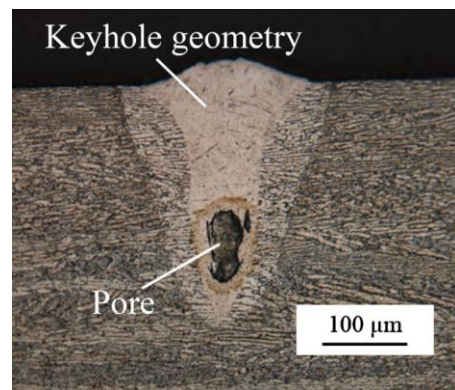


Figure 17: Visualization of keyholing porosity



(a)



(b)

Figure 18: Images of porosity in AM. (a) Lack-of-fusion porosity [65] (b) Keyhole porosity [7]

#### 2.8.4 *Dislocations*

Another potential microstructural defect of concern in this work is dislocations and dislocation density. High thermal gradients are generated between the inputted thermal energy required for printing and the remaining structure [5]. Heterogeneous thermal expansion caused by these thermal gradients can lead to high local stress and can generate distortions [66]. Dislocations are caused by the necessary resolution to distortions in the crystal lattice. Heterogeneous thermal expansion resulting from these thermal gradients can create high local stresses leading to the formation of plastic strains and distortions [6]. Similar to porosity, the dislocation density can have mechanical performance effects on an AM part [60]. No measure of dislocations in the AM parts of this work are made.

## **CHAPTER 3. MATERIALS**

### **3.1 Overview**

Multiple test specimens are used throughout this work. A large aluminum block was initially used as a test specimen for its large size and the setup flexibility it provides. Additively manufactured specimens are the focal point of this work. The application of the developed techniques to AM is the preeminent goal. A concrete block was used in a parallel project and shows the range at which this work can be applied. All three material groups are explained in detail in this section. The corresponding measurement setups for these specimens are listed in CHAPTER 4.

### **3.2 Aluminum Specimen**

The aluminum specimen used in this work provided a large metal testing block for the initial development and theoretical testing of this work. Wrought manufactured metal specimens are significantly cheaper than AM specimens therefore allowing for larger specimens. The placement of wedges, transducers, and phased arrays in various configurations is made easier with the flexibility provided by a larger specimen.

The dimensions of the specimen used in the preliminary stages of this work are shown in Figure 19. The specimen is a large 6061-T6511 aluminum block with no known imperfections. The relatively linear microstructure allows for easily predictable wave propagation, but since all commercial materials have some amount of microstructural defects, a measure of acoustic nonlinearity is still possible in this material. 6061-T6511 is a commonly used aluminum series with good corrosion resistance.

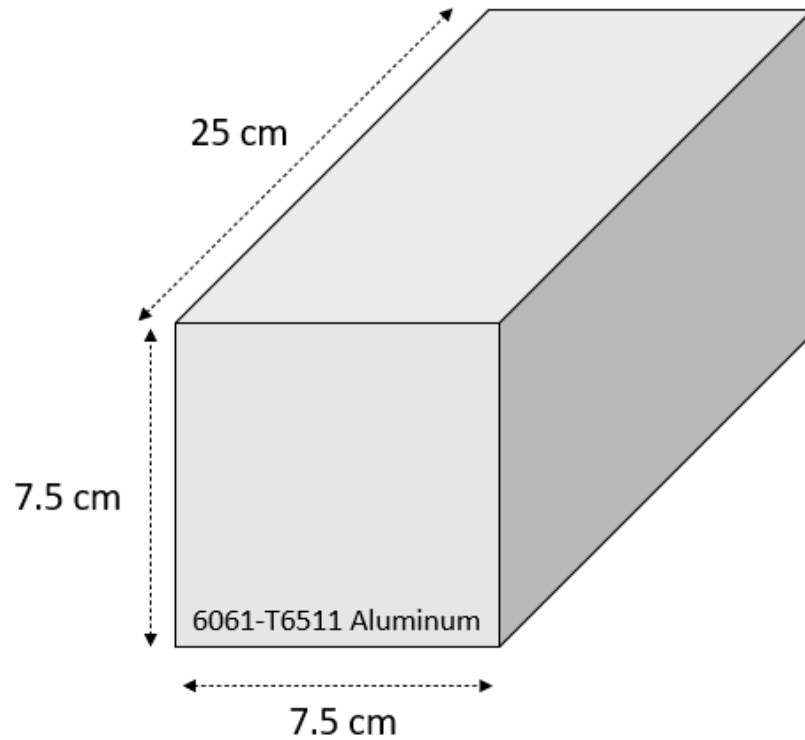


Figure 19: Aluminum specimen geometry

### 3.3 Powder Bed Fusion Specimens

Four AM specimens were made for this work. Three are 316L stainless steel parts printed during the same build and are discussed in the majority of the work. The fourth was printed using the same system parameters and is discussed in the Appendix. The three specimens were manufactured on an EOS M290 with laser powder-bed fusion [67]. Powder for all three parts is from Carpenter Technology's 15-45 $\mu$ m diameter spherical powder. Printing parameters used on the EOS M290 system are included in the Appendix.

### 3.3.1 Nominal and Underpowered AM Specimen

Two of the specimens are visually identical as seen below:

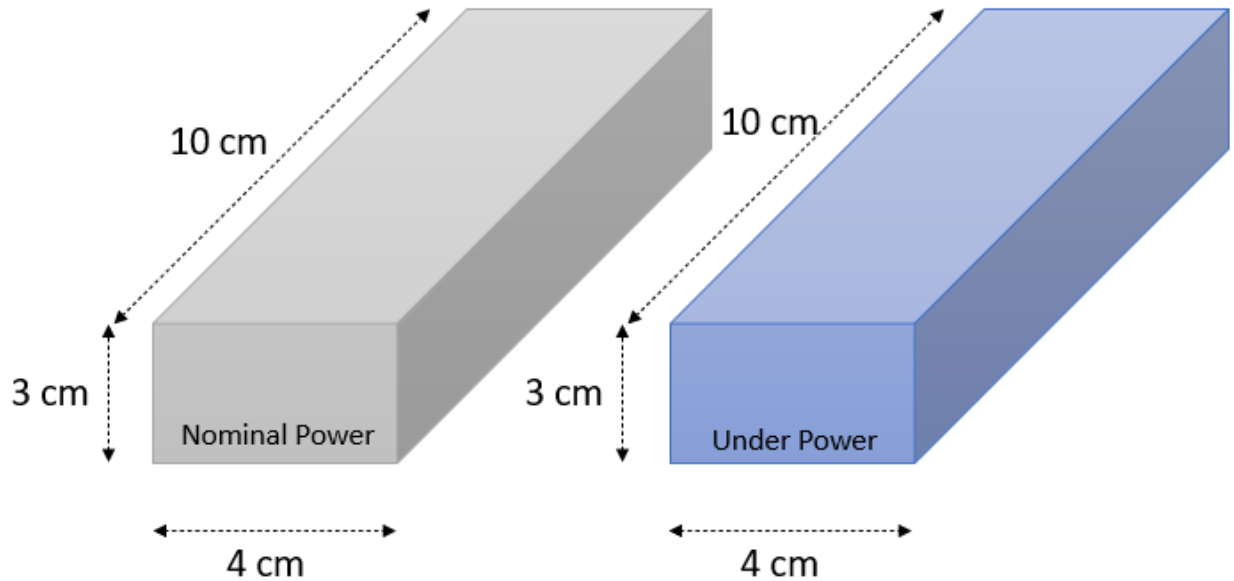


Figure 20: 316L PBF Specimens

Both are flat bars with identical visuals (the underpowered specimen is identified in blue for distinction in this work only). One is made with the standard power (214 W) for the EOS scanning speed. The other is purposefully underpowered (160 W) to cause an increase in lack-of-fusion porosity.

### 3.3.2 Acoustically Transparent Boundary

To accommodate the width needed for scanning with the setup with phased arrays, the two specimens are coupled together with a nearly acoustically transparent boundary as shown in Figure 21.

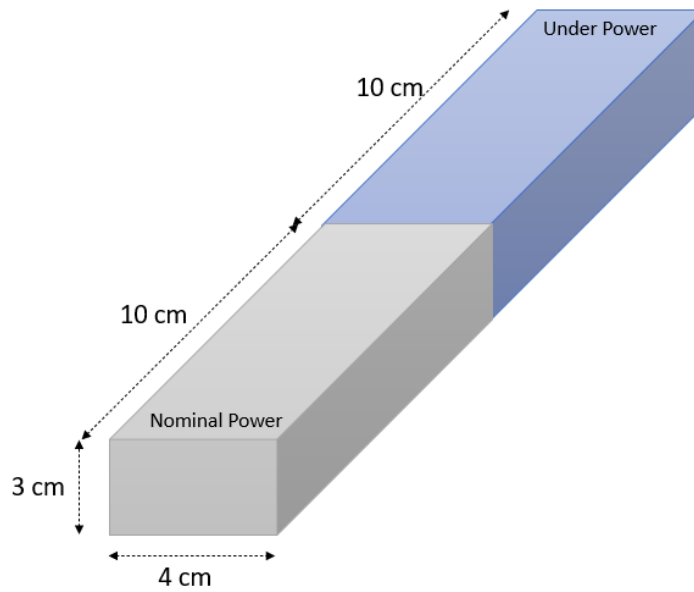


Figure 21: Combined AM specimen

The two specimens are clamped together as shown in Figure 22. In Figure 22, the combined AM specimen is labelled in yellow.

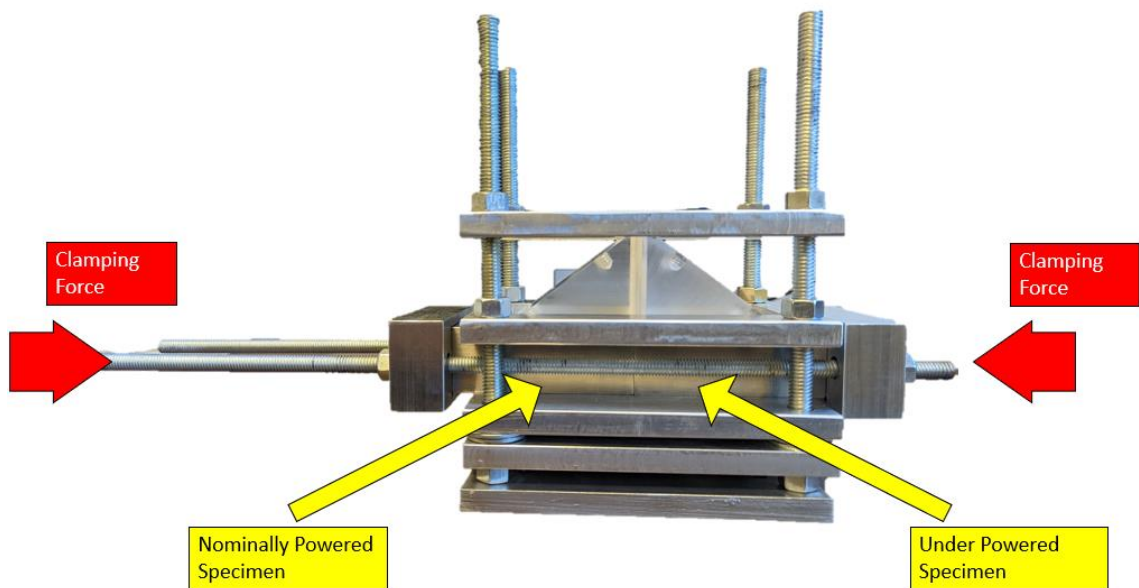


Figure 22: Combined AM specimen configuration

A clamping force is applied with threaded rod and two identical machined brackets (shown in Figure 23). These brackets help to distribute the clamping force evenly across the boundary.

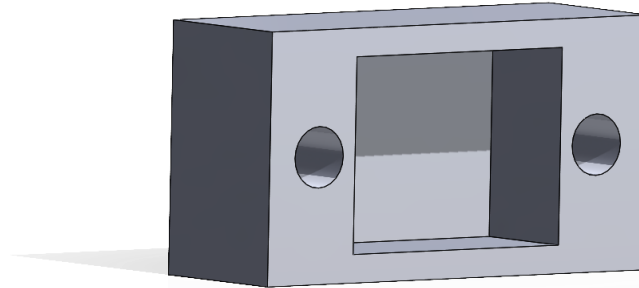


Figure 23: Combined AM specimen holder

The two touching ends of the combining specimens are machined square to have even contact between the two parts. Between both parts, a thick shear couplant is applied in a very thin layer.

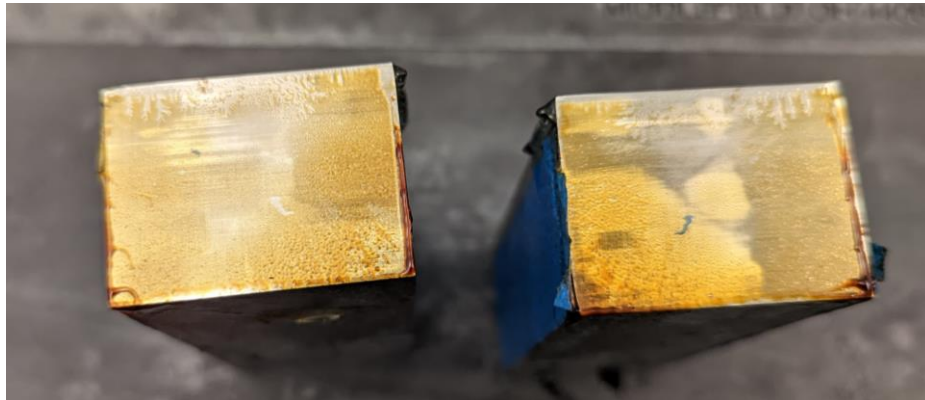


Figure 24: Shear couplant for combined AM specimen

A shear couplant is thick enough for the propagation of shear waves, allowing a shear wave to propagate from one specimen to another. While high amounts of care are taken to ensure the best coupling conditions, some acoustic loss does occur at this boundary as shown in future sections. These losses are easily accounted for by altering the amplitude

of the two emitting phased arrays to counteract the effects of acoustic loss. This boundary does not cause any noticeable acoustic distortion or refraction as shown in Section 4.4.4.1.

Because the acoustic loss can be counteracted and there is no noticeable distortion, this boundary is considered “acoustically transparent” for this work. This boundary is meant to overcome challenges associated with benchtop testing and is not indicative of scenarios seen in practical applications. The closest parallel to this scenario is a welded seam between two parts. The application of these techniques in this scenario is not explored in this work.

### 3.3.3 *AM Stack*

During the same print as the two specimens in Figure 20, a third specimen with purposefully varied layers was manufactured. The printing conditions of this specimen are identical to the previously aforementioned specimens. It contains three distinct regions: a nominally powered section (214 W) mirroring the nominal specimen in Figure 20, an underpowered section (160 W) mirroring the underpowered specimen in Figure 20, and an overpowered section (270 W) as shown in Figure 25.

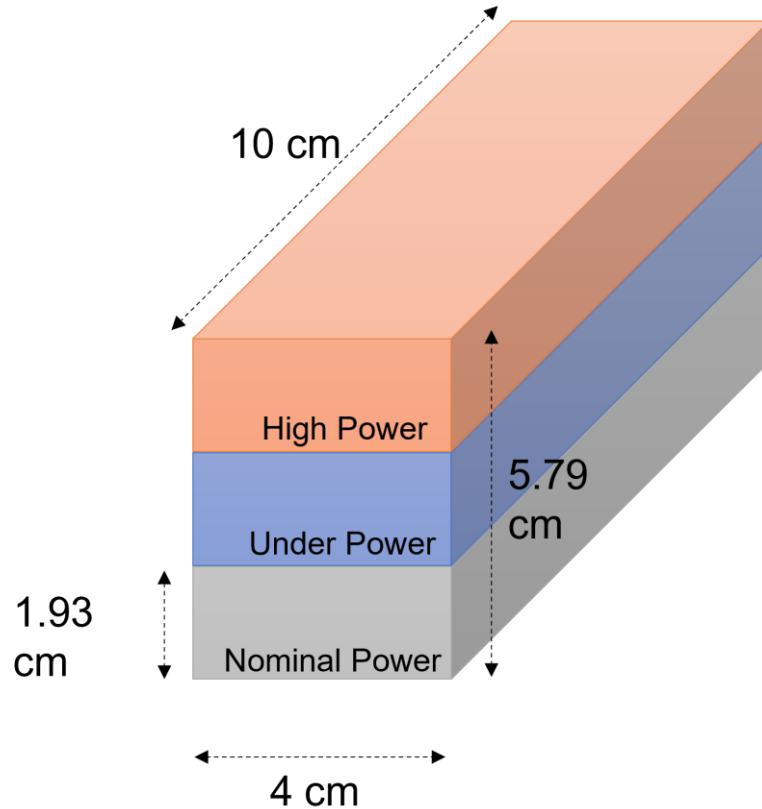


Figure 25: Additively manufactured stack specimen

The width and length of this specimen mirrors the other two additively manufactured specimens, but the height is larger since it is comprised of the three distinct layers. This part was manufactured before the final iteration of the testing setup was developed. Therefore, the geometric constraints associated with the phased arrays used in this work were not accounted for in the planning and manufacturing of this part. Each layer in this part could not be scanned with the developed phased array based system due to geometric constraints. However, this part can still provide a valuable insight into the phased array wave mixing technique. The boundary between each region is as manufactured and is more accurately representative than the coupled boundary discussed in Section 3.3.2.

### 3.3.4 Porosity Measure

X-ray computed tomography (x-ray CT) is a non-destructive testing technique that can be used to image microstructural features within a specimen including porosity [26]. A series of x-ray images are taken on a specimen as it is rotated 360° within the test chamber. These images are reconstructed into grayscale slices that can be combined into a 3D view of the specimen. For this work, a Zeiss Metrotom 800 X-ray was used to investigate the differences in porosity between two specimens. Each scan is done at 70 kV.

Representative 316L PBF specimens printed at the nominal voltage of 214 W and purposefully underpowered at 160 W were scanned. The specimens are 1.1 cm cubes printed concurrently with an additional AM specimen (See Appendix) in the same build chamber using the same build settings as the corresponding layer.

For the 1.1 cm specimens, a total of 1,690,729,056 voxels are obtained. The resolution of these scans is 18  $\mu\text{m}/\text{voxel}$ . Typical pore size associated with lack of fusion porosity in this material is 10~20  $\mu\text{m}$ . [63]. An interior volume is selected to remove porosity associated with the exterior skin of the specimens. The data can be segmented into 1,174 individual “slices” along the z axis in the direction of printing. Each slice is a grayscale image with granularity from 0 to 65,535.

#### 3.3.4.1 Image Processing

Significant image processing is required to quantify the porosity from the x-CT data. The image processing is performed such that there is a qualitative visual match to pore structures. A consequence of this method is that the result is dependent on the subjectivity in the thresholds used to determine porosity. To counteract challenges associated with the

large data size from the resultant scans, a porosity is measured for each layer of the scan and the specimen result is averaged through all analyzed layers. This approach does not consider the interconnectivity of pores through the cross section, nor does it allow for a determination of grain size analysis in the print direction, which is the same direction of the volume slicing. This approach has been successfully used in literature to characterize porosity in agreement with more robust methods [26].

The raw grayscale image is constructed by plotting the voxels isolated to a single z-axis layer. A zoomed in example of this is shown in Figure 26a. The grayscale image is considerably noisy, and the porosity defects are not overtly evident, however dark regions corresponding to porosity can be seen. A 2-D adaptive noise-removal filtering, Weiner filter, is applied as shown in Figure 26b. The Weiner filter is intended to remove additive noise while inverting blurring. To combat the loss associated from blurring, a 2-D order-statistic filtering is applied to help distinguish potential dark regions corresponding to porosity as shown in Figure 26c. This process is furthered with a Fast Local Laplacian filtering in Figure 26d. This filter helps with edge detection and increases contrast within the image. The final filtering is a binarization in Figure 26d based the built in MATLAB command `adaptthresh`. This binarization is based on local first order statistics which can counteract the effects of lighting gradients resultant from the x-CT.

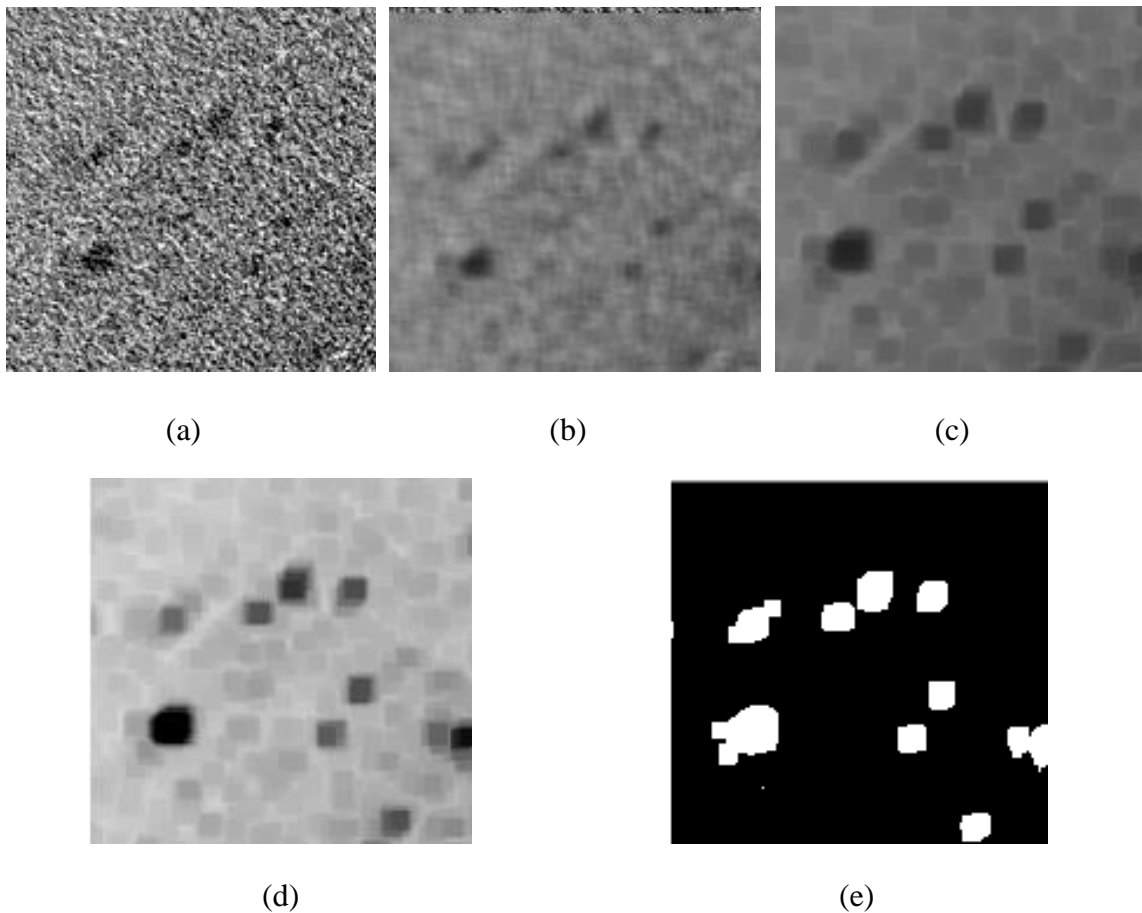


Figure 26: Image processing steps for porosity measurement of x-CT scan. (a) Raw grayscale image. (b) Weiner adaptive noise filter (c) 2D order statistic filter (d) Fast local Laplacian filtering of images (2) Binarization of grayscale to porosity count

With a binarized image, the process of counting the porosity is subject to a potential source of bias as a size threshold is placed. Light regions in Figure 26e that are below a certain area size are discarded and the remaining area of porosity for the slice is summed. This thresholding does not count for small pores that may be unassociated with lack-of-fusion porosity. It also does not account for small cross sections of a pore that intersect the plane of the slice. However, the total porosity is averaged through all analyzed slices. The porosity corresponding to this slice is calculated from the total area of the summed pores and the total area of the specimen at that slice.

The average porosity percentage of underpowered specimen (160 W) is 10.51% which is 36.4% higher than the nominal powered specimen (214 W) which has an average porosity percentage of 7.27%. This increase in porosity for the underpowered specimen is expected and matches trends seen in literature [26]. The intended goal of this porosity characterization is to ensure that the printing parameters used in the creation of the test specimens do correspond to their intended differences in porosity as predicted in the literature [8], [68].

### **3.4 Concrete Specimen**

A concrete based testing setup was developed in parallel to the wave mixing in additive metals. The details and results of this work can be found in *Kim et al.* [57]. A brief description of the main specimen is included here to give a perspective on the broad range of materials this technique can be applied to in future works.

#### *3.4.1 Dimensions*

A concrete prism was cast to be  $96.6 \times 30.5 \times 28.6 \text{ cm}^3$ . The composition of the concrete mixture is as described in Table 5. By mass, the water-to-binder ratio is 0.40 and the binder is 90% cement and 10% limestone. This binder was selected to reduce thermal deformation and allow for better bonding between the cast concrete and the embedded damage. This good bonding is a better simulation of real-life scenarios in which areas of damage are naturally formed in a concrete structure due to lifecycle use. The NDE techniques in this work are intended to examine the damage itself and not improper contact conditions. After removing the cast concrete from the plywood mold, the concrete block is cured at room temperature.

Table 5: Concrete Specimen Construction Details

Component	Amount (kg/m <sup>3</sup> )	Standard	Source
<b>Crushed quartz river sand</b>	700	ASTM C33	Lambert Sand and Gravel, Shorter, Alabama
<b>Crushed granitic gneiss coarse aggregate</b>	1061	ASTM C33 #67 gradation	Vulcan Materials Company Lithia Springs, Georgia
<b>Coarsely ground limestone powder</b>	46		BARACARB 50, Halliburton
<b>Portland cement</b>	409		Type I/II, LafargeHolcim

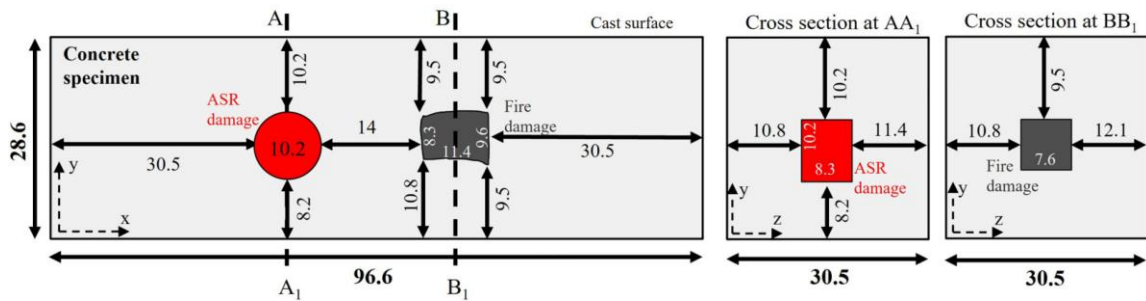


Figure 27: Schematic of a cast concrete specimen with embedded damage

### 3.4.2 Embedded Damage in Concrete Specimen

Two regions of internal damage are cast into the concrete specimen. In Figure 27, the red insert shows an alkali-silica reaction (ASR) damaged cylinder from I-676 in Atlanta. A harmful reaction occurs between siliceous aggregate minerals and alkaline pore solution in concrete. A moisture containing gel is produced which can lead to swelling and

eventually internal microcracking. The other region of damage is a fire damaged specimen of a precast concrete bridge girder from I-85 in Atlanta. As the fire occurs extraneously to the concrete specimen, the differential in thermal expansion between aggregate and paste can lead to cracking. Furthermore, the cement hydration products can begin to degrade, leading to further microcracking. Detailed quantification and characterization is included in the literature report on this project [57]. A visualization of how the damaged inserts were cast into the concrete specimen is seen in Figure 28.

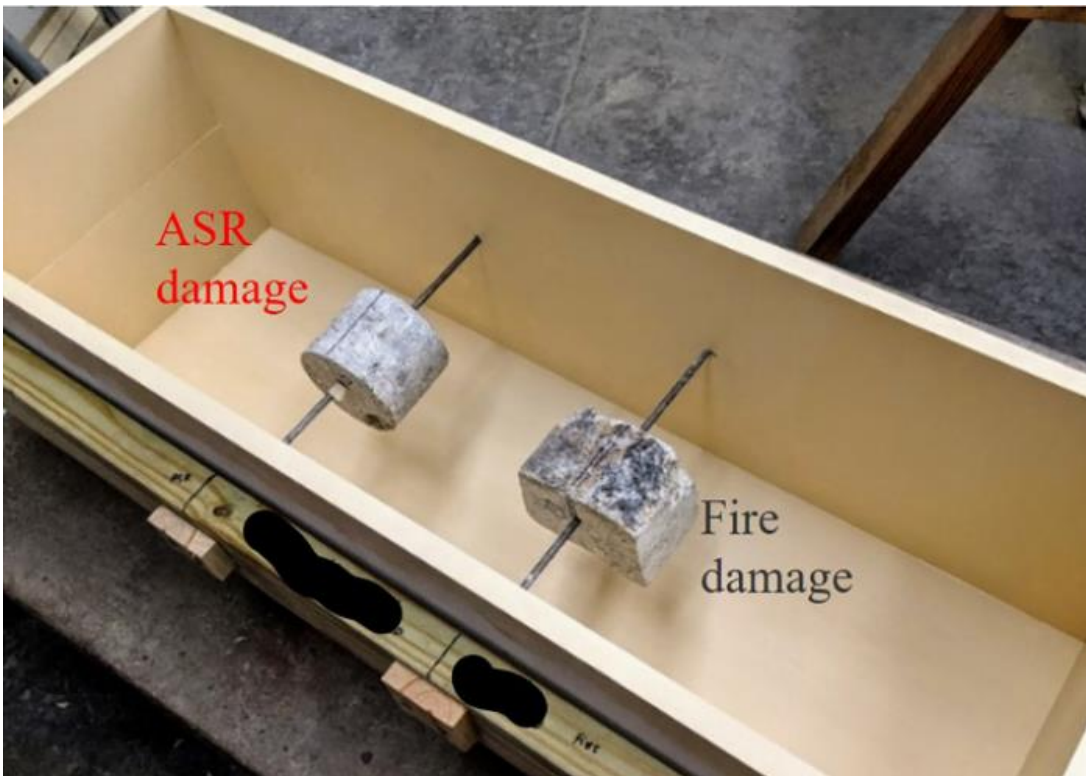


Figure 28: Inserted damage into concrete block

## **CHAPTER 4. EXPERIMENTAL PROCEDURE**

### **4.1 Overview**

The experimental procedures used in this work are detailed in the following section. First the linear ultrasonic setups measuring speed of sound and attenuation are covered. Then each of the nonlinear wave mixing setups using only single elements are explained. These setups share a general form, but the differences determined by the tested material are important distinctions to observe. For phased array based nonlinear wave mixing, the system details and theorized scanning capabilities are first explained. Then the setup configuration for each tested material is shown. The final setup is a comparative nonlinear bulk measurement setup.

### **4.2 Phase Unwrapping Velocity Measurement**

As shown in Section 0, the success of nonlinear wave mixing measurements is highly dependent on accurate wave velocities of the material. Common techniques for measurement of longitudinal and shear velocity are based on time of flight and time of first arrival. These techniques can be prone to error caused by phase shift and unknown system delays. In this work, a phase unwrapping velocity measurement is used [69]. The velocity of a wave can be found from the phase differences at various points of the wave. In practice, the comparison is made between the initial measure of an ultrasonic wave packet traveling through the medium of interest and the first reflection. To measure these two parts of the signal, the setup in Figure 29 is used.

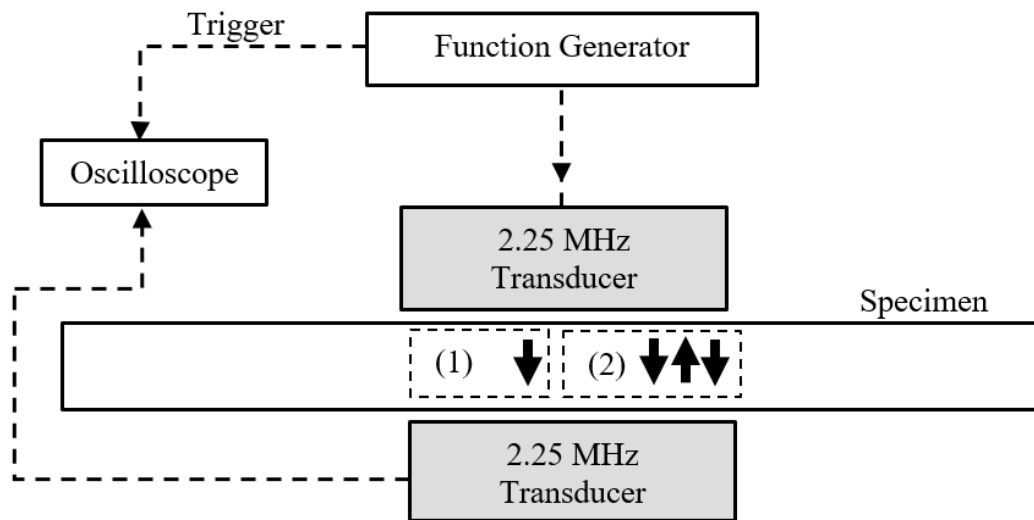


Figure 29: Setup for measuring first through-transmitted and first reflected signal. Dashed boxes labeled 1 & 2 in specimen show path taken from first and second wave packet.

An Agilent 33250A arbitrary function generator is used to generate an electric pulse to excite a 2.25 MHz centered Panametrics V106 longitudinal transducer with a radius of 0.5 inches. The input wave is a 20-cycle tone burst at 2.25 MHz. An identical receiving transducer is placed at the opposite end of the test specimen. Both transducers are coupled to the test specimen surface with a thin oil based couplant.

The first and secondary wave packets shown in Figure 30 are easily separated in the time domain given that the number of cycles is small enough for the propagation distance (i.e. twice the sample thickness). Once the two wave packets are separated, a Hann window is applied to each to remove the influence of transient components as shown in Figure 31. This transience is attributed to the ringing up and down of the transducer from the excitation of the acoustic wave. The frequency spectra of each packet are then analyzed with a discrete Fourier transform. Using the built in MATLAB unwrap command, the phase of each packet is unwrapped and plotted as a function of frequency as shown in Figure 32.

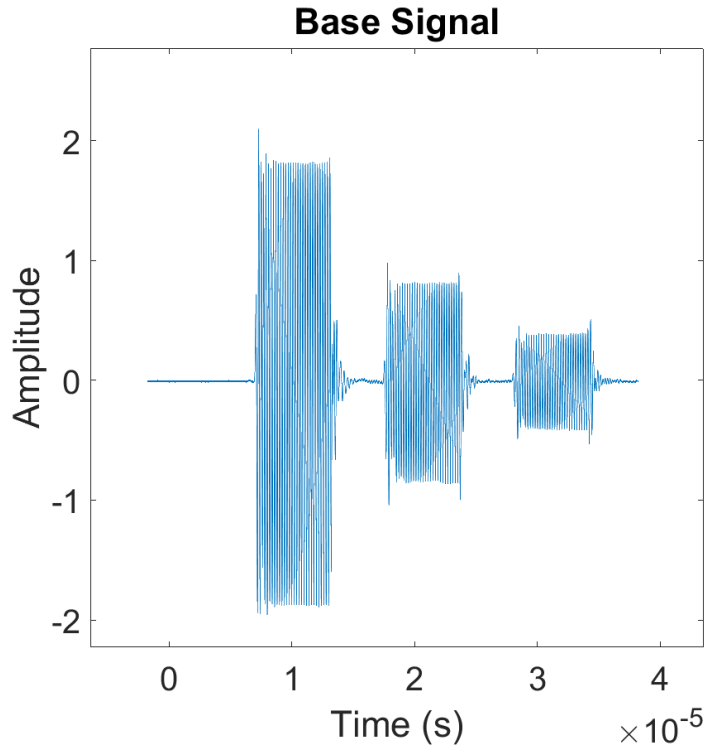


Figure 30: Measured signal for phase unwrapping velocity measurement

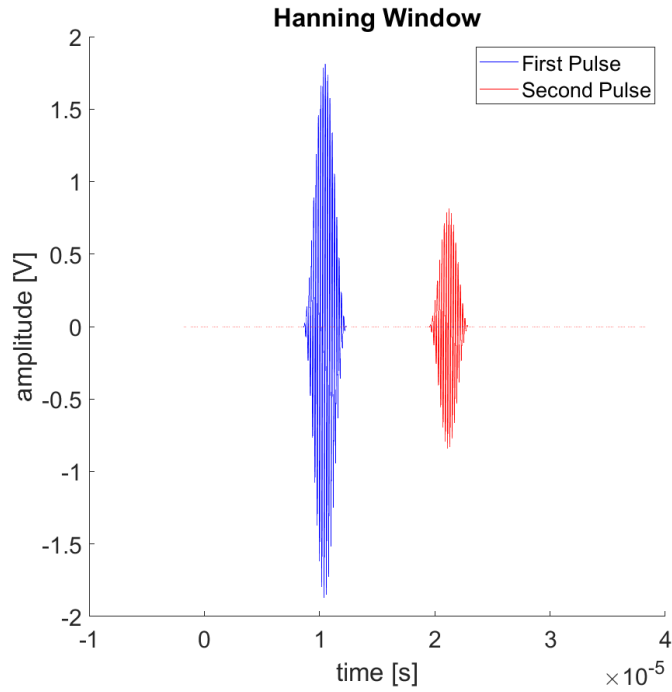


Figure 31: Hanning window applied for phase unwrapping velocity measurement

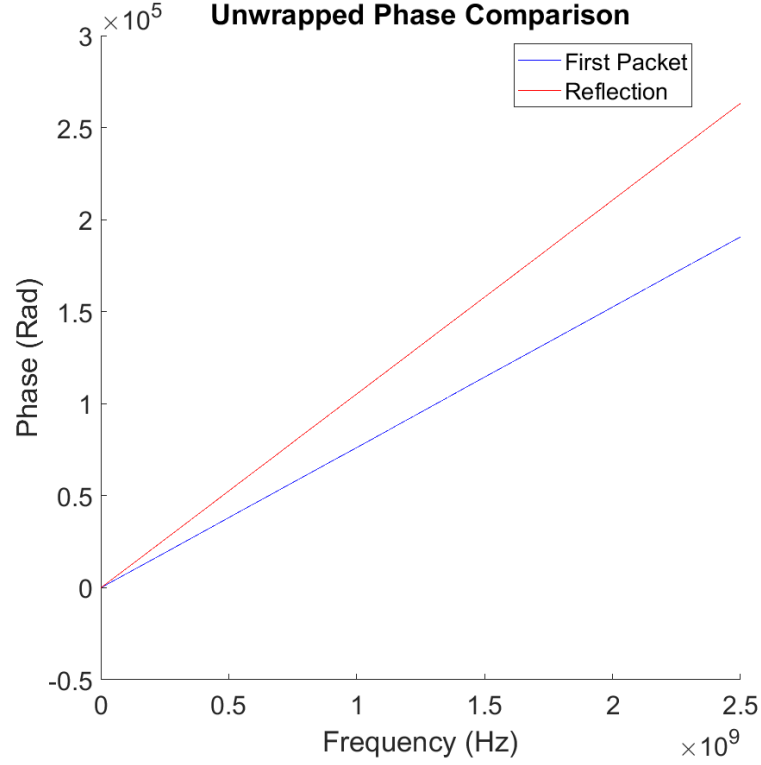


Figure 32: Unwrapped phase comparison as a function of frequency

The spectra of each packet are defined as:

$$S_1(f) = IT_T T_B D(z) e^{-\alpha z} e^{i[kz - \omega t + \Phi_o]}$$

(72)

$$S_2(f) = IT_T T_B R_T R_B D(3z) e^{-\alpha 3z} e^{i[3kz - \omega t + \Phi_o]}$$

where  $I$  is the spectrum of the input signal and  $T_T$ ,  $T_B$ ,  $R_T$ ,  $R_B$  are the transmission ( $T$ ) and reflection ( $R$ ) coefficients for the top ( $t$ ) and bottom ( $b$ ) surfaces.  $D(z)$  and  $D(3z)$  are the respective diffraction coefficients for the first and second wave packet.  $\Phi_o$  is the phase offset of the packet in relation to the input signal phase.

From the ratio of the spectra, a frequency dependent phase velocity,  $c$ , relationship can be acquired:

$$\arg \left( \left| \frac{S_1}{S_2} \right| \right) = |kz - \omega t + \Phi_o - (3kz - \omega t + \Phi_o)| = 2kz = \frac{4\pi fz}{c} \quad (73)$$

which can be solved for the phase velocity,  $c$ , as:

$$c = \frac{4\pi fz}{\arg \left( \left| \frac{S_1}{S_2} \right| \right)} \quad (74)$$

The total speed of sound measurement for each material is an averaged value from 5 independent measurements. The measurement is made for each material with both shear and longitudinal setups. For shear measurements, the Panametrics V106 transducers are replaced with Panametrics V153 shear transducers which are centered at 1 MHz and the oil based couplant is replaced with a thick shear couplant which allows for the propagation of shear waves.

### 4.3 Attenuation Measurement

Linear ultrasonics measurements are used as a comparative measure for the sensitivity of nonlinear ultrasonic techniques to microstructural features. Acoustic attenuation is an intrinsic material property which is influenced by material composition, crystal grain structure and inhomogeneities. It was initially developed by R.L. Smith at the National NDT Centre in the United Kingdom for the characterization of material grain size [70], [71]. Relative attenuation and not absolute attenuation are used in this thesis as a comparative measure to the sensitivity of the developed nonlinear mixing technique with phased arrays.

The relative acoustic attenuation can be found from the equation below. The derivation of this relation is found in the Appendix of this work.

$$\alpha(f) = \frac{1}{2z} \left[ \ln \left( \left| \frac{V_1}{V_2} \right| \right) - \ln \left( \left| \frac{D(s_1)}{D(s_2)} \right| \right) \right] \quad (75)$$

where  $z$  is the distance of propagation path through the material,  $V_1/V_2$  is the measured voltage ratio between the steady state portions of the first and second wave packets, and  $\frac{D(s_1)}{D(s_2)}$  is the ratio of the diffraction corrections for two propagation distances. With a consistent experimental setup, the largest variation in each specimen's attenuation comes from the material itself. Therefore, these values are used as a relative attenuation measurement to compare between specimens.

The attenuation for each specimen is measured using contact transducers in a through transmission setup as seen in Figure 33. This experimental setup has been previously used to study microstructure in additively manufactured metals [72]. Two identical broadband transducers (Panametrics V106), centered at 2.25 MHz, are clamped through the thickness of the tested material with an oil based couplant between each contact surface. One transducer is connected to a function generator and acts as the transmitting receiver. The other is connected to an oscilloscope as a receiver. The input signal is a 20-cycle tone burst and the measurement is taken in 1 MHz increments between 1-10 MHz.

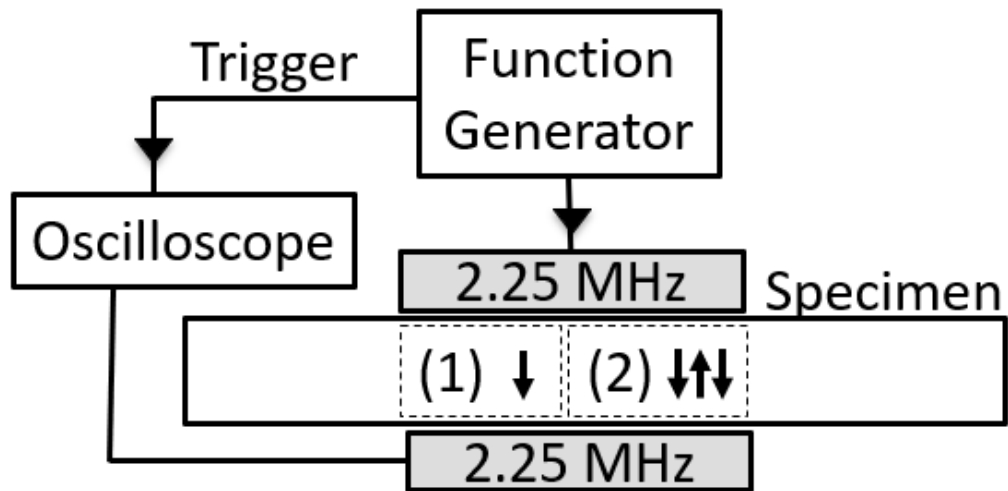


Figure 33: Through transmission attenuation measurement setup. Dashed boxes labeled 1 & 2 in specimen show path taken from first and second wave packet.

Two wave packets are examined for each measurement; the first signal (labeled 1 in Figure 34) travels through the thickness of the specimen once, while the second (labeled 2 in Figure 34) travels through the sample three times. The relative attenuation for the frequency measured is found by comparison of these two first wave packets.

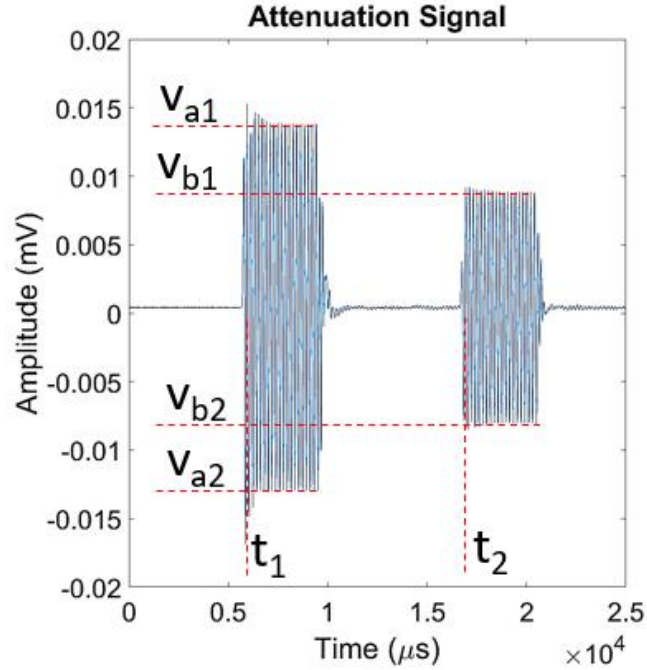


Figure 34: Time Domain Signal for Relative Attenuation Measurement

#### 4.4 Nonlinear Wave Mixing with Single Element Transducers

The preliminary stages of this work include the setup and development of a single element noncollinear wave mixing setup based on previous works found in the literature [33]. An auxiliary immersion setup was created to further understand the required geometry necessary for correct mixing conditions to be met [34]. The single element mixing setup was then adapted for each of the three material classes (aluminum, AM stainless steel, and concrete). A shear-shear mixing condition, the first entry in Table 1, was selected based on the previously mentioned rationale that is repeated here in brief for clarity.

The mixed wave is a longitudinal wave propagating in the direction of the sum of the two initial waves ( $\mathbf{k}_r = \mathbf{k}_1 + \mathbf{k}_2$ ). The longitudinal wave is easier to measure at the angle of intersection with the material surface. This forward propagation is easier to measure as

it prevents potential geometric conflicts between the emitting transducers and the necessary location of the receiver.

The experimental setup in each of the three materials is similar. The variations come from the required mixing conditions, the best frequency for the material, and the wedges needed to launch shear waves at the correct angle in the material.

#### *4.4.1 Single Element Nonlinear Wave Mixing in Aluminum Block*

The large aluminum block has a relatively uniform microstructure and is used for exploration of wave mixing conditions in metal. No known damage has been imparted to the aluminum block and the microstructure of the aluminum is thought to have less microscale damage in comparison to stainless steel. Nevertheless, quadratic nonlinear behavior is still exhibited by the material and the generation of a scattered wave is still possible if resonance conditions are met. A schematic of the experimental setup is shown in Figure 35.

The measured speed of sound in the aluminum block is  $c_L = 6300.9 \frac{m}{s}$  and  $c_T = 3127.4 \frac{m}{s}$  as presented in Table 6. Using Equation 56, the angle required to meet resonance conditions is found to be  $121.4^\circ$ . A Rexolite® wedge is cut based on Snell's law to  $41.2^\circ$  in order to convert the longitudinal output of the emitting transducers to shear waves propagating at  $60.7^\circ$ . The mixing area is located between the two emitting points since the same propagation angle for the incident waves is mirrored.

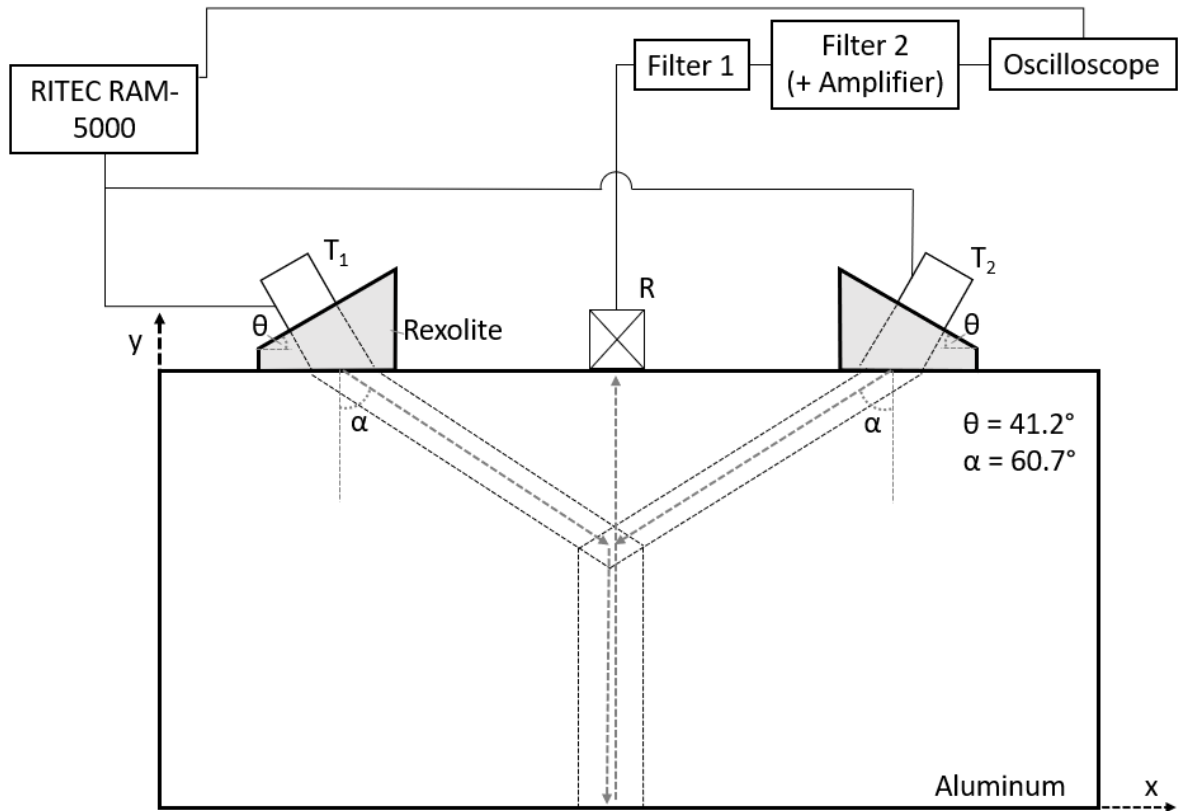


Figure 35: Single element mixing setup in aluminum

The RITEC RAM-5000 is a computer controlled modular ultrasonic system. It is used to output two 5 MHz 20 cycle tone burst signals to a pair of Valpy Fisher CF0504LN (centered at 5 MHz) emitting transducers. The transducers are coupled to two identical acrylic wedges. The wedges are then clamped to the top surface of the aluminum block. A receiving transducer (Valpy Fisher CF1005LN centered at 10 MHz) is clamped on the top surface at the exact midpoint between the two wedges. Each contact surface is coupled with an oil based couplant. As Table 3, the mixed wave propagates forward away from the emitting wedges. It then reflects off the bottom surface of the block before reaching the receiving transducer on the top surface.

The received signal is passed through a series of amplifiers and inline bandpass filters before it is recorded on an oscilloscope. The filters are the Mini-Circuits BBP-10.7+

Lumped LC Band Pass Filter with a  $50\ \Omega$  elliptic response between 9.5 to 11.5 MHz. A 10 MHz bandpass filter is used to filter unwanted signal that could have been generated by the experimental setup or second harmonics of unexpected input into the signal. The filter response is seen below in Figure 36.

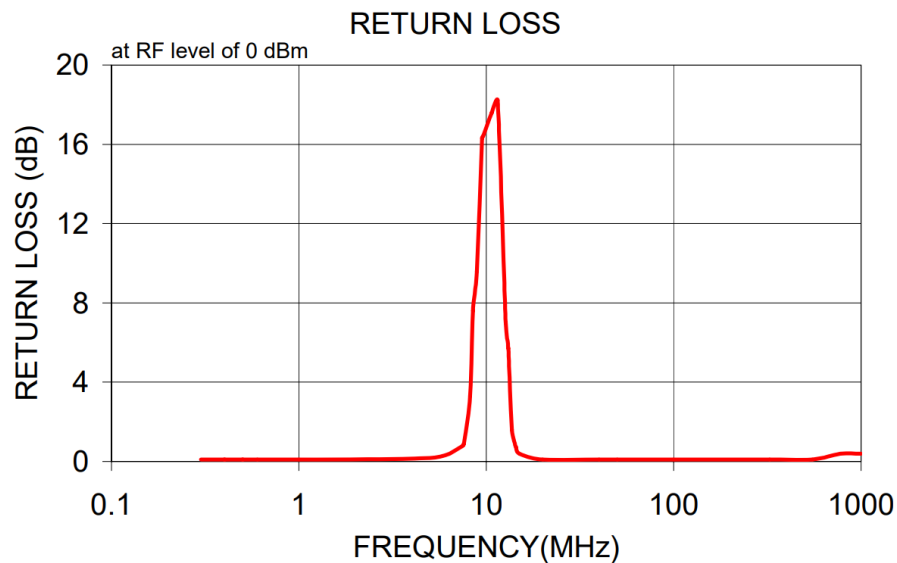


Figure 36: Inline bandpass filter response [73]

Following each bandpass filter, an amplifier is used to increase the signal amplitude. First a Panametrics Model 5072 PR Ultrasonic Pulser/Receiver is set to a gain of 20 dB followed by an Olympus Panametrics-NDT Ultrasonic PreAmp with a predetermined gain of 40 dB. This signal is then recorded with an oscilloscope and averaged 256 times to increase signal-to-noise ratio.

The mixing point can be found from ray tracing the emitting waves. Because of symmetry in the input waves, the mixing point is centered below the two wedges. The depth of the mixing point is determined geometrically by the separation of the two acrylic wedges. The only way to move the mixing point is to translate the setup or change the wedge separation distance. Translation of the wedges across the block surface would

translate the mixing point within a plane of constant depth in the block. The mixing point can be raised by bringing the two wedges together or lowered by increasing separation. Since this block is homogeneous, the measured nonlinear value is not expected to change significantly. However, movement of the mixing point can be used to help validate that the received signal is from the nonlinear wave mixing of the two input waves.

#### 4.4.1.1 Proof of Mixing

Verification that the received wave is resultant from nonlinear wave mixing can be done by comparing the wave field when both emitting transducers are outputting simultaneously and independently. The setup shown in Figure 35 is used. A measurement is made with only one emitting transducer emitting. A second independent measurement is subsequently made with only the other transducer emitting. The sum of the two independent measurements is compared to a measurement made with both transducers emitting simultaneously. If nonlinear wave mixing is occurring, the interaction of the two initial waves will produce a unique outcome, the scattered wave. This unique interaction will occur at a time and location that can be predicted to further verify the measurement. This verification has been previously used to determine the level of system nonlinearity unassociated with nonlinear wave mixing [33]. Verification similar to this procedure is used for each nonlinear wave mixing setup.

#### 4.4.1.2 Laser Vibrometer Setup for the Visualization of Wave Mixing

The need for the four-way polarity flipping technique in AM specimens is theorized to be caused by the high level of non-mixed nonlinearity that is temporal and geometrically difficult to separate from the mixed wave. A large source of this nonlinearity is thought to

come from second harmonic generation of longitudinal waves that are not converted into shear waves in the AM specimens. Through the use of a 3D laser vibrometer, the propagation of waves in the wedge and material can be visualized and the effects of these unwanted second harmonics is seen.

As part of a collaboration with Los Alamos National Laboratory, the experimental setup of wave mixing in the aluminum block was visualized with laser vibrometry. A PolyTec 3D Laser Vibrometer (PSV-500-3D) is synced with the emission of the input ultrasonic waves following Figure 35. A highly reflective coating is added to the wedges and aluminum block to aid in the tracking of wave motion. The transducers are placed as close as possible to the front edge of the aluminum block to increase movement visualization. Particle motion in all three dimensions is recorded for a variety of mixing tests to understand the mechanisms affecting the testing setup.

#### *4.4.2 Single Element Nonlinear Wave Mixing in Concrete*

Due to the highly heterogeneous nature of concrete, low frequency NDE measures are better suited to this material. Lower frequency waves are less scattered from the heterogeneities within concrete. In this setup, two 50 kHz centered Ultrasonics GRD50-D50 transducers are used for generation of input longitudinal waves. The transducers are screwed and coupled to a set of Teflon wedges cut to an angle of 27.5°. Unlike the metal examples, Teflon is used for the mode conversion wedges due to its low longitudinal speed ( $c_L = 1450 \text{ m/s}$ ). As with previous setups, the wedges cause a mode conversion from the initial longitudinal waves into shear waves in the concrete. The mixed wave is received at the top of the specimen with an Ultrasonics GRD50-D100 that is centered at 100 kHz. Both the emitting and receiving transducers have a diameter of 5 cm. The placement of emitting and

receiving transducers on the same side is important for realistic applications of ultrasonic NDE to concrete structures. Many concrete structures are inaccessible from both sides and single sided measurements are important.

The function generator used is an Agilent Model 33250A and the power amplifier is an ENI 240L. The input signal is a 40 kHz tone burst with four cycles. This shorter length is necessary when working with low frequencies to avoid overlap with the mixed and reflected signals. The reflected signal at 80 kHz is filtered through two Butterworth filters (Krohn-Hite Model 3202 and Krohn-Hite Model 3988) both set with cutoff frequencies at 70 and 90 kHz. A gain of 6 dB and 20 dB is added after the filtering to make up for loss. To further increase signal-to-noise ratio the received signal is averaged 256 times.

To scan the concrete block for the ASR and fire damage, the Teflon wedge and emitting transducers are translated along the surface. To increase the depth of the scanning volume, the distance between transducers is increased. The spatial resolution of this setup is estimated to be between 6.5-8.3 cm.

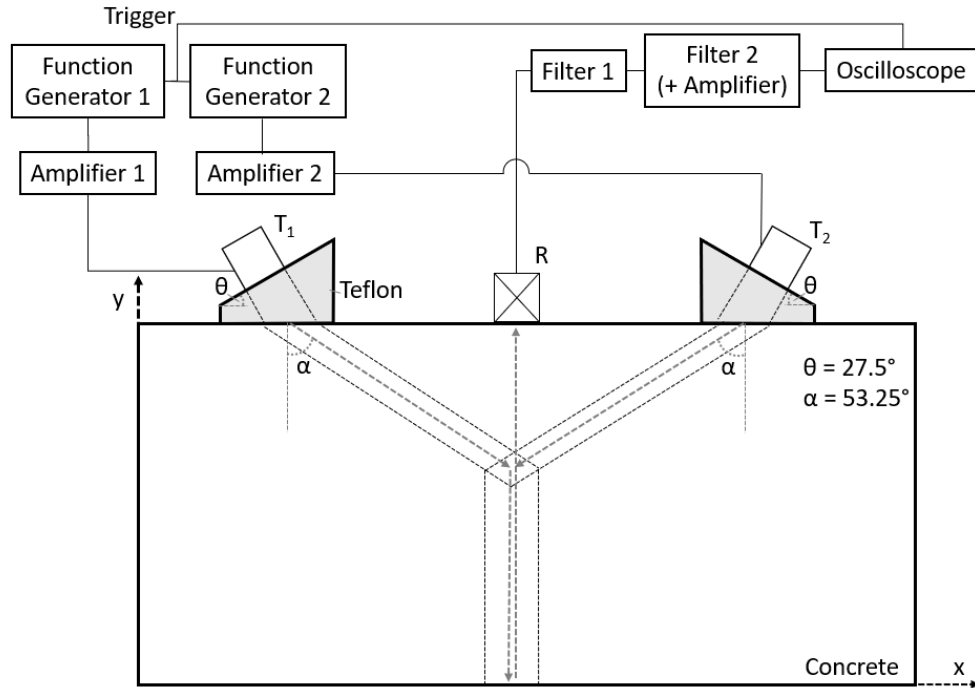


Figure 37: Experimental setup for single element wave mixing in concrete

#### 4.4.3 Single Element Nonlinear Wave Mixing in Homogenous AM Material

Testing of the AM materials is conducted in a similar fashion to the aluminum block. Because the speed of sound ratios in the AM specimens are different from aluminum, a different mixing angle of  $115.4^\circ$  is required. Similarly, to achieve this input angle new Rexolite® wedges are cut to  $40.5^\circ$ . The angle definitions are shown in Figure 38.

Because of the limited size of the AM specimens, the receiving transducer is placed on the opposing side of the transmission. This geometric constraint is also experienced in experimental setups for the AM specimens using phased arrays. Unlike the aluminum and concrete structures, the small size of AM specimens does not dictate the need for single sided measurement in many use cases. The same transducers, amplifiers, and filters from

the aluminum setup (Section 4.4.1) are used for the AM specimens. The mixing setup shown in Figure 39 is used for both the nominal and underpowered AM parts.

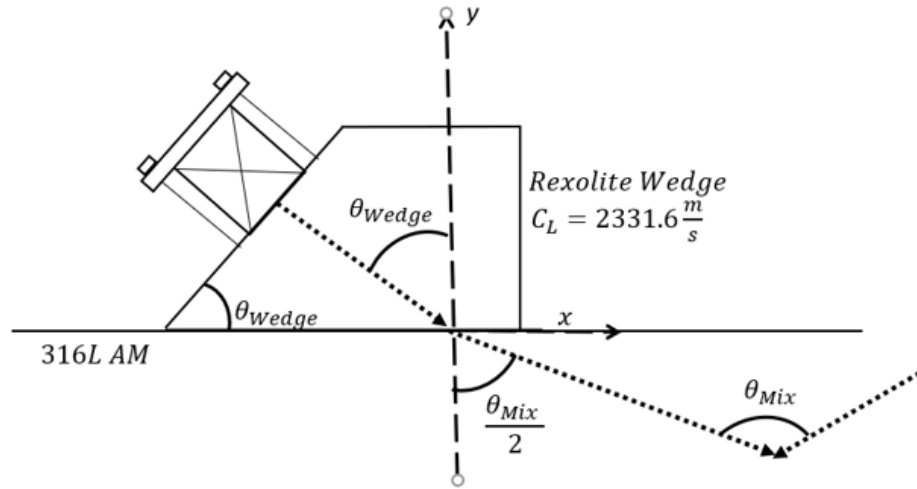


Figure 38: Geometric definitions for wedge angle calculation for single element mixing

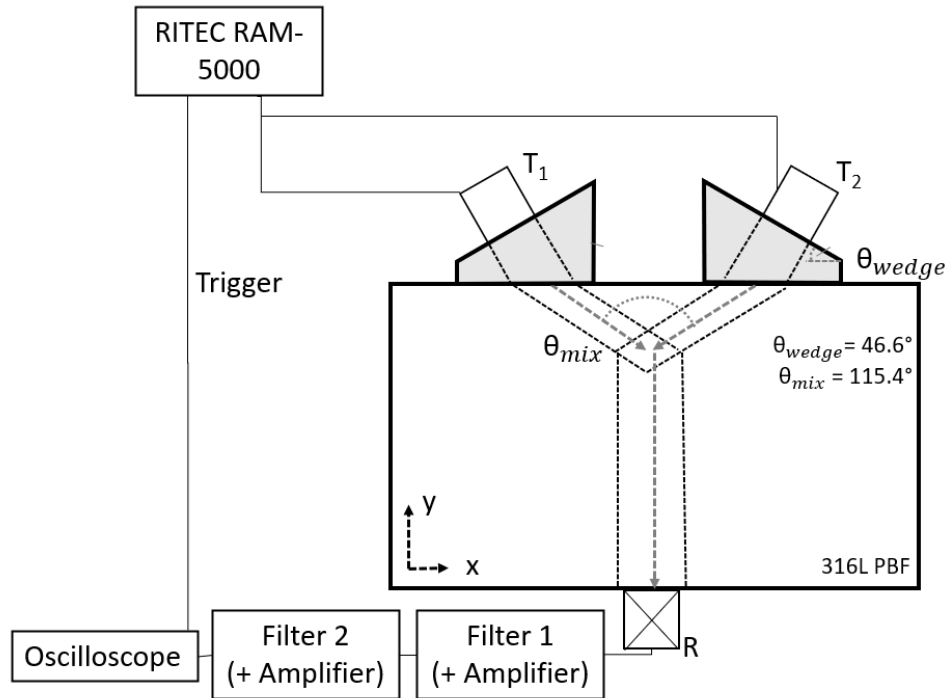


Figure 39: Homogeneous AM single element mixing schematic

#### 4.4.3.1 Single Element Diffraction Correction

The effects of attenuation on the incident and scattered wave are accounted for in this section. Wave mixing in highly attenuative materials including the concrete specimen must account for the effects of diffraction. In high frequency applications including the AM specimens and the aluminum block, the effects of attenuation on the mixed wave are reduced. However, the effects of diffraction are considered for completeness.

The proportionality used for the relative measure of acoustic nonlinearity,  $\beta$ , from Equation 33 is restated below:

$$\beta_{rel} \propto \frac{A_3}{A_1 A_2}$$

where  $A_1$ ,  $A_2$ , are the amplitudes of the input waves and  $A_3$  is the amplitude of the resultant mixed wave. The amplitudes of the waves in Equation 33 should be the amplitude of the corresponding wave at the point of mixing. A diffraction correction is added to Equation 33 to account for the effects of propagation distance on the input and mixed waves as well as the single element diameter modeled by a circular piston source. The input waves  $A_1$ ,  $A_2$  are diffracted from the input at the transducer by the following relation:

$$\begin{aligned} A_{1m} &= A_1 e^{-\alpha_1 d_1} D(\omega_1; d_1) \\ A_{2m} &= A_2 e^{-\alpha_2 d_2} D(\omega_2; d_2) \end{aligned} \tag{76}$$

where  $A_{1m}$  and  $A_{2m}$  are the amplitude of the input waves  $A_1$  and  $A_2$  at mixing,  $\alpha_1$  and  $\alpha_2$  are the frequency dependent attenuations at frequencies  $\omega_1$  and  $\omega_2$ ,  $d_1$  and  $d_2$  are the propagation distances from the emitting location to the mixing point, and  $D$  is the

diffraction correction for a circular piston source [74]. The diffraction correction is found from:

$$D(\omega_i; d_i) = \sqrt{\left(\cos\left(\frac{2\pi}{s}\right) - J_0\left(\frac{2\pi}{s}\right)\right)^2 + \left(\sin\left(\frac{2\pi}{s}\right) - J_1\left(\frac{2\pi}{s}\right)\right)^2} \quad (77)$$

where  $J_0$  and  $J_1$  are the zeroth and first order Bessel functions of the first kind.  $s$  is the single composite variable defined as:

$$s = \frac{2\pi d}{ka^2} \quad (78)$$

where  $d$  is the propagation distance and  $a$  is the radius of the piston approximation.

A similar correction to  $A_1$ ,  $A_2$  must also be applied to the amplitude of the scattered wave  $A_3$ . Recall from Equation 59, that the amplitude of the third wave is dependent on the amplitude of the two incident waves. In the case of nonlinear wave mixing within a solid,  $A_3$  cannot be measured at the point of mixing. The amplitude of the mixed wave at the receiver,  $A_3'$ , is diffracted from the point of mixing to the receiver location. This can be accounted for by the following:

$$A_3' = A_3 e^{-\alpha_3 d_3} D(\omega_3; d_3) \quad (79)$$

The diffraction corrected wave amplitudes in Equation 76 and Equation 79 are inserted into the proportionality of  $\beta$ , from Equation 33. The amplitudes of the input waves are common in both the denominator and numerator as shown in Equation 59 and are therefore removed

from the calculation of  $\beta$ . The resultant relative  $\beta$  calculated for single element diffraction in this work is computed as:

$$\beta_{rel} = \frac{A'_3 e^{\alpha_1 d_1} e^{\alpha_2 d_2} e^{\alpha_3 d_3}}{D^2(f_1; d_1) D(f_3; d_3)} \quad (80)$$

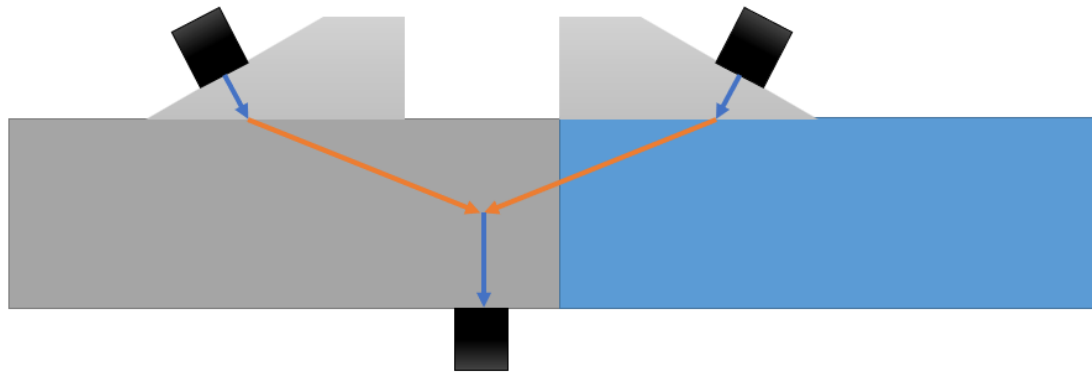
In the case of single element mixing in a homogeneous material,  $d_1$  and  $d_2$  are equal due to symmetry and  $\alpha_1 = \alpha_2$ .

#### 4.4.4 *Single Element Nonlinear Wave Mixing in Heterogeneous AM Material*

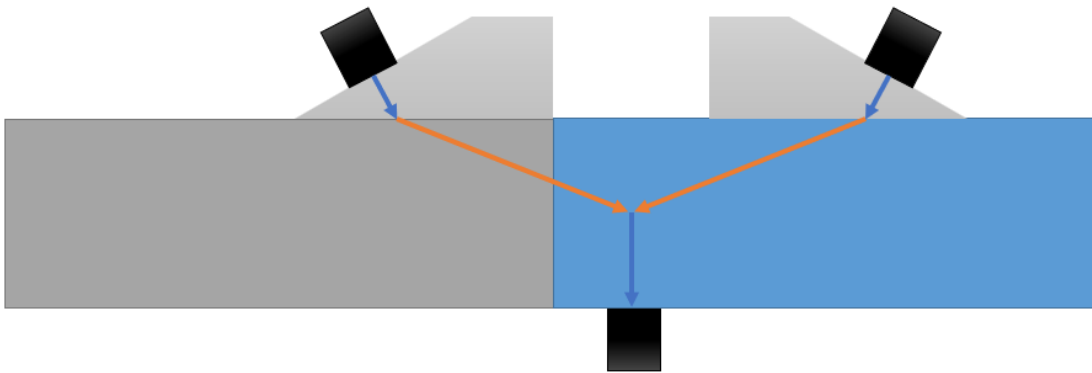
The testing setup used on the individual AM specimens is then used on the heterogeneous AM specimen. This experiment is done to determine the effect of the layer boundary on the mixing setup.

##### 4.4.4.1 Across Acoustically Transparent Boundary

The combined specimen as described in Section 3.3.2 is tested by placing the emitting transducers and wedges on opposite sides of the acoustically transparent boundary. If the polarization of a shear wave is parallel to the plane of a solid-solid interface (grain boundary) as in this experimental setup, no longitudinal waves are generated [75]. By translating the setup across the boundary, the two sides can be “scanned” to determine the sensitivity of the setup to the location of the mixing point. In the two cases shown in Figure 40, the mixing point is in a different side. The input waves travel the majority of their path through materials with differing microstructural compositions.



(a)



(b)

Figure 40: (a) Single element mixing in nominal AM specimen (b) Single element mixing in underpowered AM specimen

The experimental equipment used on this heterogeneous combined material is identical to the homogeneous material in Figure 39. There is no need to account for refraction at the interface as discussed alongside the results of this measurement in Section 5.4.4.1. Diffraction correction in this heterogeneous material follows Equation 80, where once again  $d_1$  and  $d_2$  are equal due to symmetry.  $\alpha_1$ , and  $\alpha_2$  are selected based on which side the incident wave travels most.  $\alpha_3$  is selected based on which side the mixing occurs.

## 4.5 Mixing Phased Array

Following the establishment of a functional mixing setup with single element transducers, the focus of the work shifted towards the development of a nonlinear wave mixing technique using phased arrays for the transmission of the input waves into the setup.

### 4.5.1 Pulse Based Transducers

The first implementation attempt used The Phased Array Company (TPAC) Explorer system. This compact system is primarily intended for in-field inspections [76]. Like many commercial systems, the Explorer is intended for linear ultrasonics, primarily using time-of-flight technology for imaging purpose. As such and to save significantly on cost and size, the system emits a pulse as seen in Figure 41. This system is based on the generation of a fixed negative square pulse for each individual element. This generation is easy as it does not require an individual high-frequency amplifier for each element. The max pulse width for this system is  $1 \mu\text{s}$ , but the optimal width of the pulse is defined as  $\frac{1}{2 \times f_{probe}} = \frac{1}{2 \times 5 \times 10^6 \frac{1}{s}} = 0.1 \mu\text{s}$ . The maximum delay between pulsing elements is  $32.9 \mu\text{s}$  which provides an additional limit to steering angle particularly when including the required delays for the incident waves to simultaneously reach the mixing point.

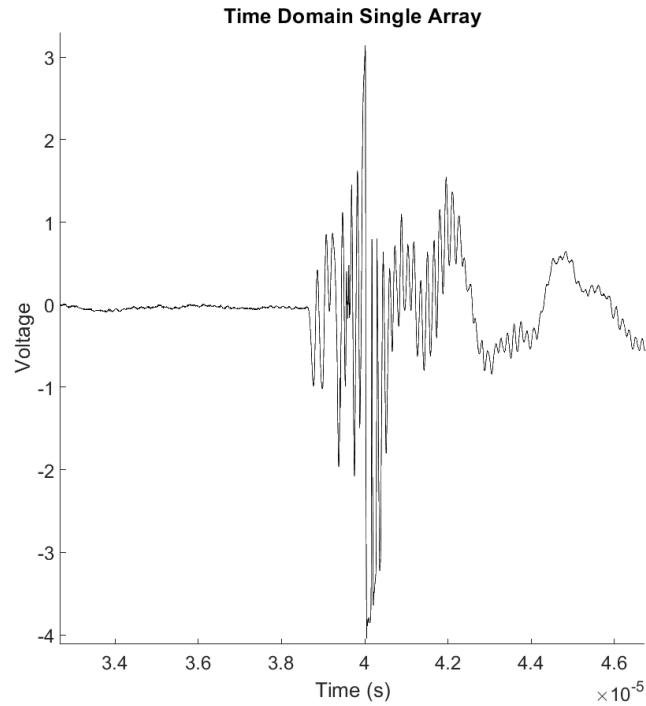


Figure 41: Example output of pulse-based phased array system

The pulse-based propagation of this system is difficult to adapt for use in a nonlinear mixing setup. The pulse is centered around 5 MHz but contains significant off-frequency components. The quantification of  $\beta$  is difficult if the input into the system is of nonuniform frequency. Furthermore, this system does not provide control over the initial polarity of the input wave. This eliminates the possibility of implementing the four-way polarity flipping technique, which was experimentally determined to be essential for nonlinear wave mixing in the studied metals due to the low nonlinearity in comparison to the concrete specimen. The results obtained from the measurements conducted with the Explorer phased array system are inconclusive and do not show significant evidence of mixing.

#### 4.5.2 *Verasonics System*

The Verasonics Vantage 256 is a research focused ultrasonic system which gives significant amounts of user control for each of the 256 channels. This system's capabilities are significantly improved from most industry phased arrays systems as it is based on Pulse Width Modulation with tristate signals to reproduce analog waveforms. For the application of wave mixing, this provides two key benefits. The first is arbitrary waveform generation capabilities, which are used in this setup for the generation of 20 cycle harmonic tone burst input signals. In comparison to short pulse-based systems, the mixing of tone bursts is easier to quantify as the mixing condition is determined in part by the frequency ratio of the two input waves. Furthermore, the larger spatial lengths caused by the increased number of cycles provides more opportunity for the input signals to intersect without the same potential for significant noise contributions from a continuous signal. The second key benefit is the control over initial polarity or 180-degree phase shift of the input waves. This capability allows for the implementation of the four-way polarity flipping technique with phased arrays.

Two Philips ATL L7-4 Linear Probes are used for the generation of longitudinal waves into acrylic wedges. These phased array transducers are second-hand medical phased arrays primarily designed for vascular imaging and diagnostics. Each L7-4 consists of 128 elements with an element width of 7 mm, pitch of 0.298 mm, and total element length of 36.2 mm defined by Figure 42. The center frequency of the transducer is nominally 5 MHz with a useable range from 4 MHz to 7 MHz. This range allows for the potential wave mixing with dissimilar frequencies. Each phased array probe used in this

research was tested to ensure proper firing of each element and that the amplitude of the outputted wave was equivalent.

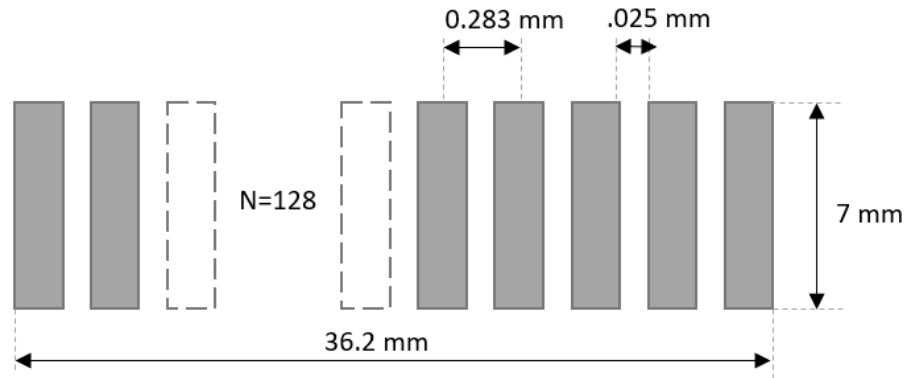


Figure 42: Phillips ATL L7-4 element dimensions

Each phased array is bolted to an acrylic wedge with Sonotech Ultrigel II as couplant. The acrylic wedges are cut differently for the aluminum and AM stainless steel specimens as described in the following sections. The Phillips L7-4 phased arrays are significantly larger than the single element transducers and the phased arrays used with The Phased Array Company Explorer system. To fit the entire L7-4 active aperture, the wedge must be 9 cm (Figure 45) long to allow for the propagation of the entire wave front into the material. A schematic and wiring diagram for the wave mixing setup using the Verasonics system is shown in Figure 43.

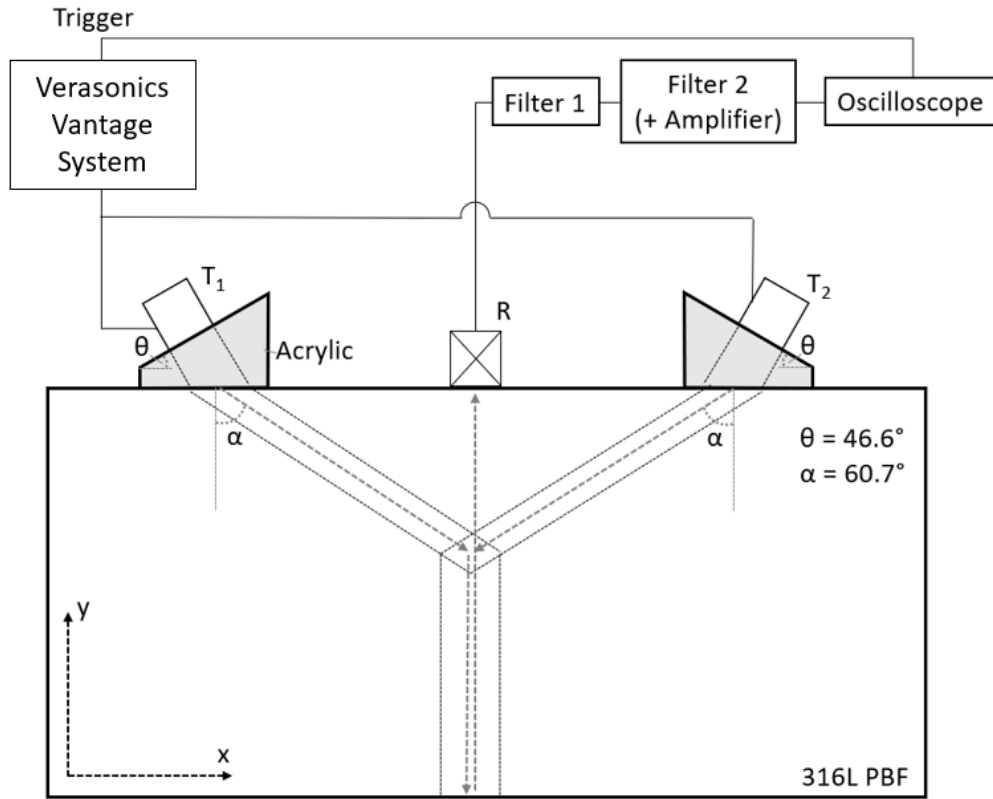


Figure 43: Wiring diagram for nonlinear wave mixing setup using Verasonics Vantage System

#### 4.5.3 Scanning Arc

Equation 56 defines the necessary angle,  $\theta_{mix}$ , between two intersecting shear waves in order to produce a third resonant wave. An arc defined by a constant angle can be made from isogonics; isogonics are lines of equal angle between two points. They can be geometrically defined with an isosceles triangle  $ABC$  with base  $\overline{AC}$  and  $\angle ABC$  equal to the required angle. An arc without constant radius can then be drawn for each location of  $B$  such that the angle  $\angle ABC$  is constant. If the angle  $\angle ABC$  is equal to the required mixing angle for resonance condition, this arc will include the potential scanning points for a given set of incident wave modes and frequency ratio within a given material. In the case of two incident shear waves propagating from a single side of the test specimen, point  $A$  is first

taken at (0,0),  $C$  is defined by the wedge separation,  $d$ , as  $(d,0)$ , and point  $B$  is defined as any point  $(x,y)$  along the arc such that  $\angle ABC = \theta_{mix}$ . From this geometry, the angle is found to be:

$$\tan \theta_{mix} = \frac{-yd}{x(x-d) + y^2} \quad (81)$$

The resultant quadratic equation from Equation 81 is then solved for all  $y$  such that the scanning arc is located in the testing material.

$$y = \frac{1}{2} * (-\sqrt{d^2 \cot^2(\theta_{mix}) + 4x(d-x)} - d \cot(\theta_{mix})) \quad (82)$$

This arc defines all possible mixing locations for the selected resonance condition (incident waves, frequency ratio ( $a$ ), acoustic velocity ratio ( $c$ )). Note that the mixing angle  $\theta_{mix}$  is a function of the parameters  $a$  and  $c$ .

An arc of constant  $121.4^\circ$  for  $a = 1$  between the two emitting positions is shown in Figure 44 for mixing in the aluminum block. Similar arcs are computed for each test material and can account for variations in the position of the emitting wedges. Changing the separation distance between the emitting wedges,  $d$ , will change the shape of the scanning arc. This should be considered in the development of future measurement setup to ensure that the potential regions of interest are covered by the scanning arc.

The two emitting positions marked on the top surface of the aluminum block are a simplified location of the ray traced expected centerline for the wave front from the L7-4 steered towards Scanning Point 2. The scanning points are arbitrarily selected along the arc and are within the emitting angle limits possible for the phased array and wedge. The

expected propagation direction of the mixed wave can be found from the vector sum of the two incident wave vectors. The intersection of the propagation direction and the bottom surface of the aluminum block is found and used for the necessary receiver location. The component of the scattered wave orthogonal to the surface is large enough to be measured by a contact transducer on this surface.

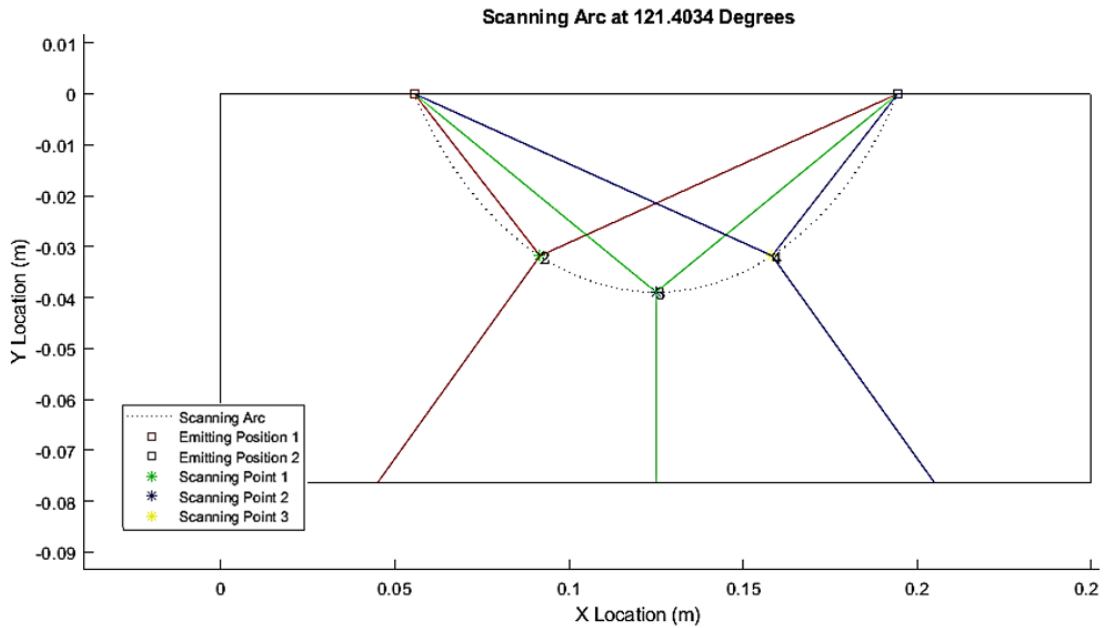


Figure 44: Scanning arc and points for Al L7-4 mixing setup

#### 4.5.4 Mode Conversion Wedge for Phased Array

A few notes on the design of the mode conversion wedge used for the Phillips L7-4 phased arrays are discussed here. Some of the design features are shared in common with mode conversion wedges used in other experimental setups. The design features are inspired by the results of laser vibrometer inspection of the nonlinear wave mixing setup as discussed in Section 5.4.2.1. As shown in Figure 45, an overhang at the top of the wedge is designed to trap non-transmitted components of the wave that are reflected back into the wedge. The leading vertical face of the wedge is not cut to  $90^\circ$  with the bottom surface.

Based on ray tracing analysis, this subtle angle helps direct reflected waves into the overhang and prevents the re-entrance of reflected waves into the test specimen. Square ridges are cut along the top and vertical surface of the wedge. These are the two wedge surfaces perpendicular to the propagation path that are not required to be flat for proper coupling. The ridges are designed to diffuse the reflected wave and remove any strong path for reflected waves to enter the specimen in large amplitude.

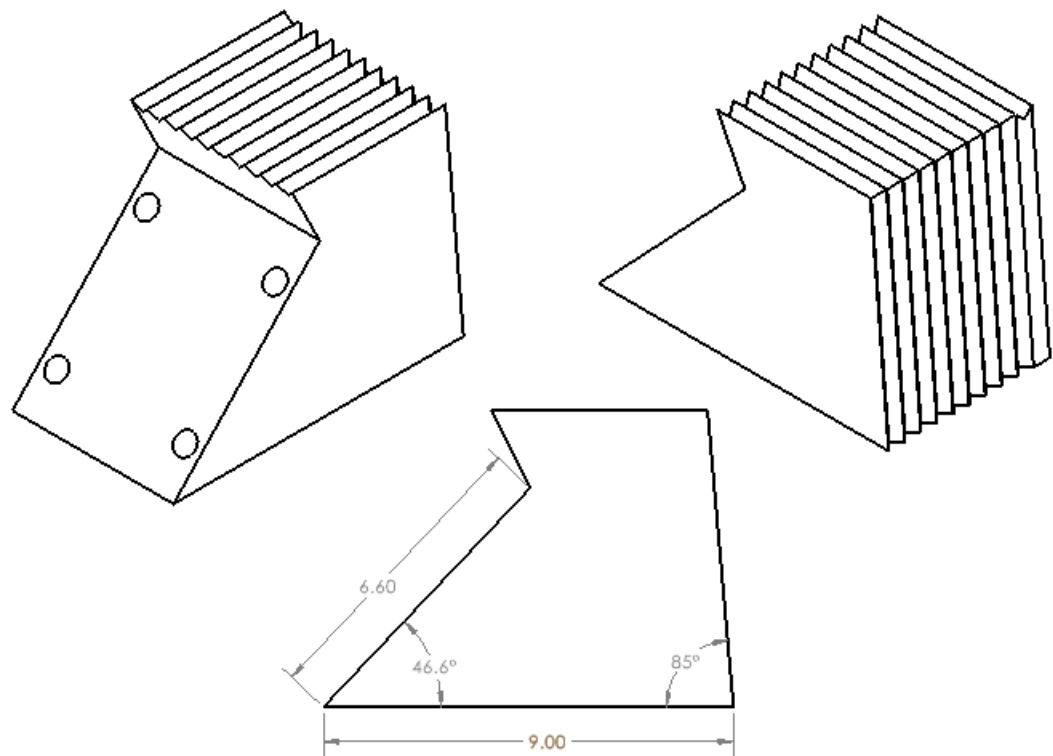


Figure 45: Wedge for Phillips L7-4 phased array mixing in aluminum. Distances are marked in cm.

The length of the wedge used for the nonlinear wave mixing setup in the aluminum block is 9 cm. This is the minimum length necessary for the complete propagation of a plane wave generated from the entire active aperture of the Phillips L7-4 (3.6 cm) with a wedge angle of  $46.6^\circ$ . The total length of the PBF AM Specimens is 10 cm. To accommodate the large size of the phased array relative to the AM specimen, only half of

the elements are used in the nonlinear mixing setup in the AM. By using only the lower half of the active area, the wedge length can be significantly shortened as shown in Figure 46. The effects of the reduced active area are discussed in Section 4.5.7.1. As a consequence of the shortened length, the overhang used in other conversion wedge designs cannot be implemented in the shortened wedge used for the L7-4 scanning in the given AM specimens.

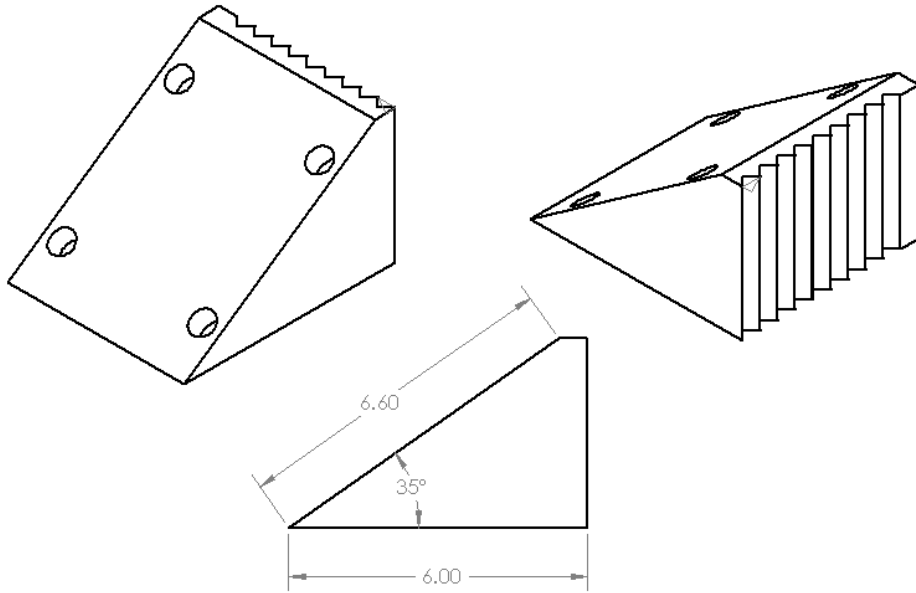


Figure 46: Wedge for Phillips L7-4 phased arrays mixing in AM specimen. Distances are marked in cm.

#### 4.5.5 Nonlinear Phased Array Scanning in Aluminum Block

The size advantage provided by the aluminum block is most helpful in establishing the phased array setup. From Table 1, a mixing angle of  $121.4^\circ$  is needed for the mixing of two same frequency shear waves in aluminum. Each wedge is cut to  $46.6^\circ$ ; this angle is cut just below the critical angle ( $49^\circ$ ) for mode conversion. It allows for the increase in angle required to generate shear waves which propagate at the necessary angle for mixing. Dimensions and features of the wedge can be seen in Figure 45.

The phased array mixing setup is similar to the phased array setup in AM metals shown in Figure 43. The same receiving transducers, filters, and amplifiers are used for all phased array nonlinear wave mixing setups. The scanning arc for the phased array setup in aluminum is shown in Figure 44. Three mixing points are selected along the scanning arc: one in the middle of the arc and two points which are symmetrically far from the center. These points are selected so that the mixed wave must be measured at a significantly far location from one another, thereby aiding in the assessment of whether nonlinear mixing has occurred. A picture of the measurement is included for visual aid in Figure 47.

The necessary timing for each phased array element to steer the incident waves to point 1 (left of center) is shown in Figure 48. The timing delay for each array is a linear relationship as no beam focusing is used. A uniform timing delay is added to the left phased array as the propagation path is shorter than from the right phased array. The propagation for each element is calculated from Equation 70 and the propagation distance in the material. This uniform delay is added to ensure that the two incident waves are meeting at the mixing volume simultaneously. Small error in this estimate is potentially permissible depending on the length of the incident wave (number of cycles). Longer incident waves provide more opportunities for interaction between the incident waves, but a long incident wave may also contribute to destructive interference with the mixed wave.

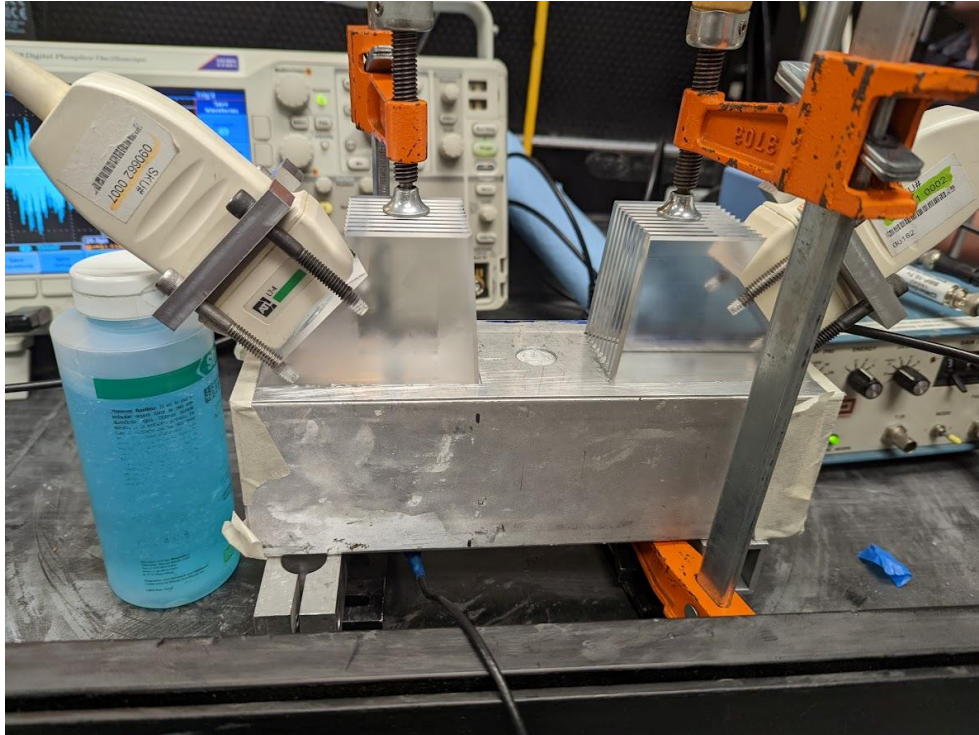


Figure 47: Experimental setup for the scanning of the aluminum block with phased arrays

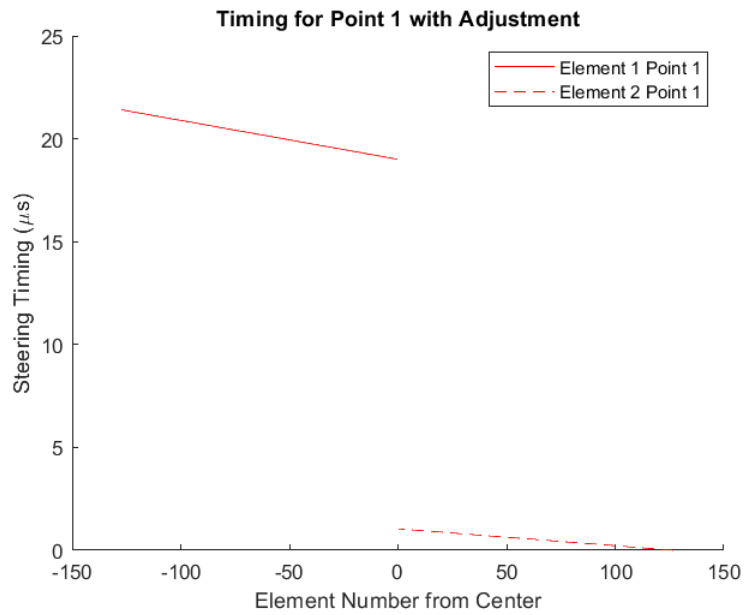


Figure 48: Phased Array element timing needed for mixing at Point 1 in aluminum block

#### 4.5.5.1 Proof of Scanning Verification

Due to the homogenous nature of the test aluminum block, verification of scanning in this specimen depends on the spatial and temporal measurement of the mixed signal and not variations in the amplitude of the mixed wave. A similar routine used for the single element scanning (Section 4.4.1.1) can be used, which is based on the uniqueness of the measurement made when both emitting transducers are made to fire simultaneously. Additionally, because of the scanning capabilities provided by the phased array, the location and timing which the mixed wave intersects with the bottom surface can be moved. Tracking the mixed wave at various locations gives further indication to the success of wave mixing.

Measurements were made with three identical receiving transducers located on the bottom of the aluminum block as shown in Figure 49. Measurements are made with all three receiving transducers for three different measurement sets, corresponding to the three colors (orange, grey, and blue) in the visual aid. Measurements from the three receiver points are compared for scanning when each of the three mixing points is targeted. Exact locations for the mixing point and necessary receiving points are calculated as in Figure 50. The propagation direction of the mixed wave is predicted by the summation of the incident wave vectors. The expected results are compared to the measurements from the three receivers.

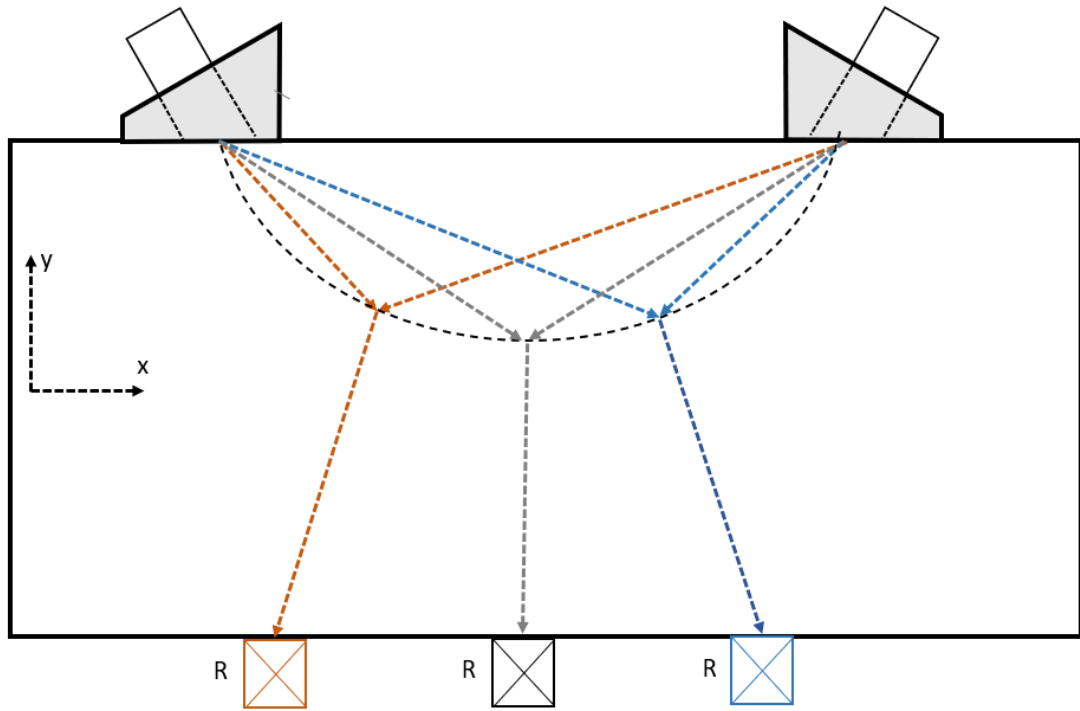


Figure 49: Scanning verification routine based on location of receiving mixed wave

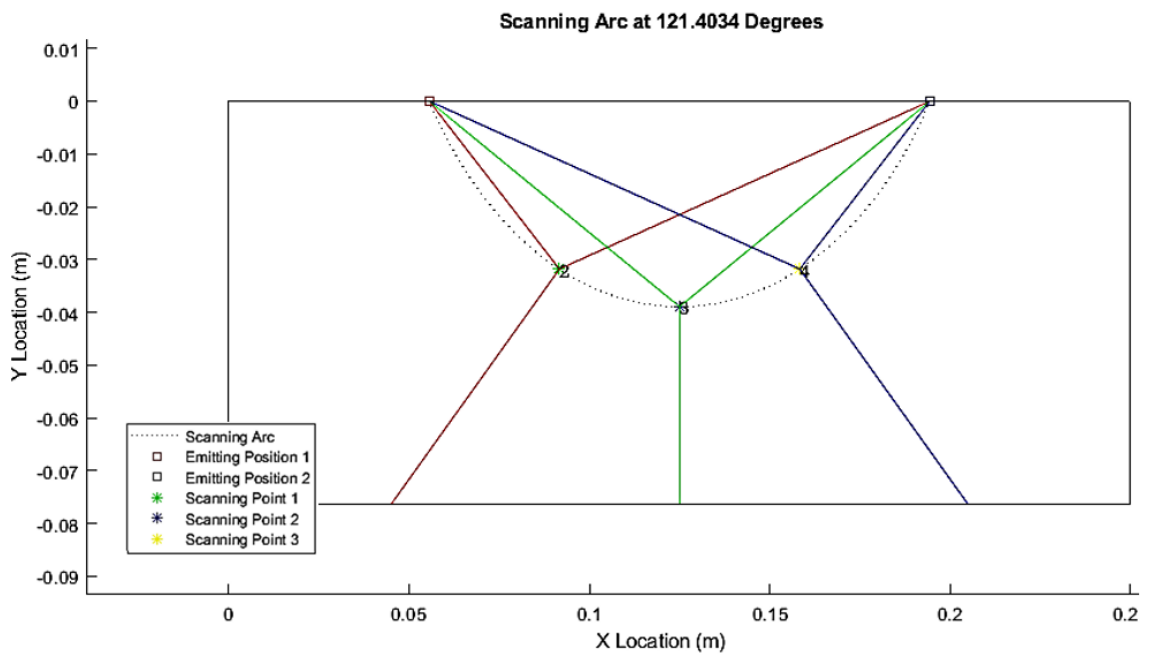


Figure 50: Scanning arc in aluminum block with phased arrays with exact locations

#### 4.5.6 *Nonlinear Phased Array Scanning in Homogenous AM Materials*

Alteration of the experimental setup was required for adaption of the scanning setup using the Phillips L7-4 transducers to the smaller size of the AM materials. Two of the mode conversion wedges for the phased arrays (Figure 45) cannot fit on a single surface of the AM specimens. As a solution, only 64 elements or half of each L7-4 phased array is used. By reducing the number of active elements used, the mode conversion wedges can be significantly shortened as shown in Figure 46 allowing for both phased arrays to fit on the test specimens. An active area of only 64 elements was found to still be a sufficient number of elements for the range of beam steering used in the nonlinear mixing setup.

Note the angle of the mode conversion wedge used for the phased array measurements in AM ( $35^\circ$ ) is smaller than the single element in AM ( $40.5^\circ$ ). The angle difference is not explained by the change in wedge construction material. The conversion wedges made for the L7-4 phased arrays are made of acrylic with a faster sound velocity than the single element wedges made of Rexolite®. Based on the resonance condition mixing angle and Snell's law for the acrylic, a wedge angle of  $48^\circ$  would be needed. Instead, a smaller angle is used to give more flexibility in beam steering. The necessary angle of propagation of the shear wave can be met by steering the acoustic wave within the wedge.

Figure 51 shows a scanning arc for using L7-4 phased arrays on nominally powered AM specimens. Distinct scanning arcs must be generated for the two studied AM specimens due to the small change in longitudinal and transverse sound velocities. Additionally, the small change in material wave speed significantly influences the timing delays required for effective beam steering with the phased array.

An assessment of the validity of the experimental setup (scanning arc and array element timing) can be performed by gradually moving the scanning location along the arc. The gradual steps along the scanning arc are shown in Figure 51 including the required shift in the receiver located at the bottom of the specimen to center the receiver to the mixed wave. This technique is effective since mixing at the center point of the arc (50% of arc length) provides a plane of symmetry for the setup. Element timing requirements for both phased arrays scanning at the center is identical, which offsets some of the effect of potential error. The influence of error increases as the measurement point is taken further away from 50% of the scanning arc.

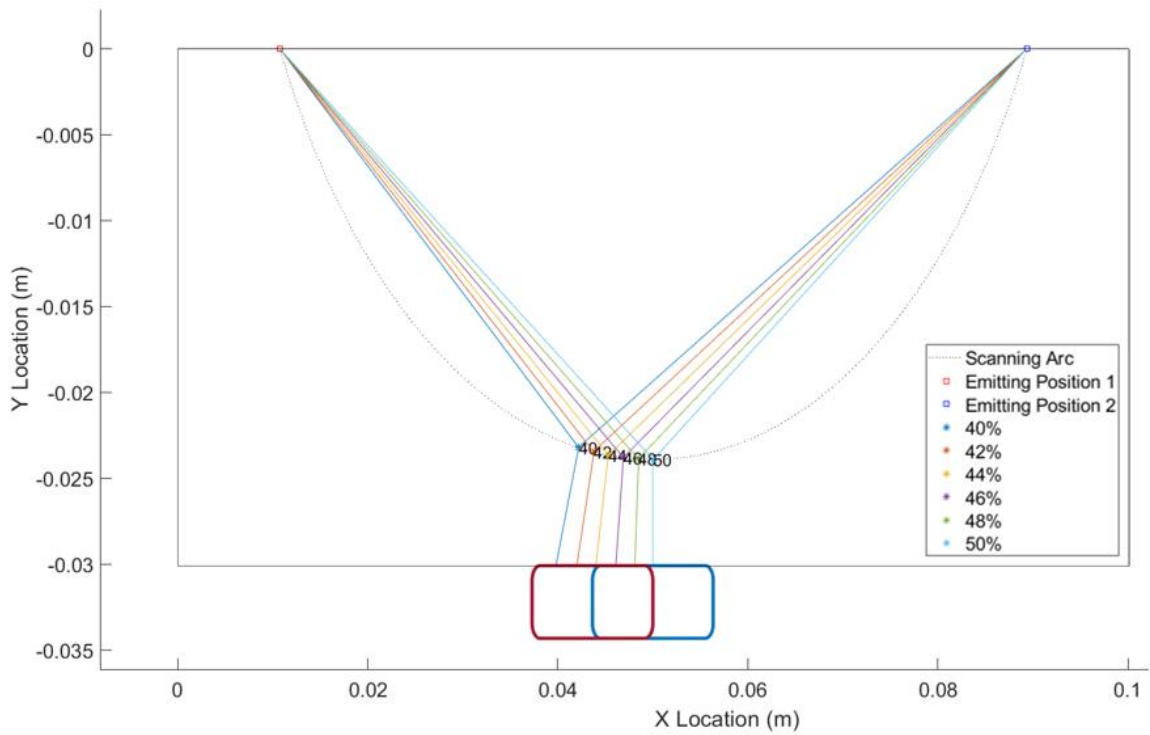


Figure 51: Scanning arc of homogenous AM specimen with phased array

#### 4.5.7 *Nonlinear Phased Array Scanning in Heterogeneous AM Material*

Following the verification of a correct phased array based nonlinear mixing setup in each of the AM specimens, the phased array testing setup was then used on the heterogeneous AM specimens. First an experimental setup for scanning across the acoustically transparent boundary is developed. Then a phased array-based measurement of the three layered stacked AM specimen is explained.

##### 4.5.7.1 Across Acoustically Transparent Boundary

Two Phillips L7-4 phased array probes are bolted to the shortened wedge shown in Figure 46. Pressure is uniformly applied from four bolts for each probe to ensure an even distribution of force coupling the probe to the wedge. The wedges are then pressed to the top of the combined AM specimen using an aluminum plate in which pressure is evenly distributed across the top of the wedges. This plate is seen at the top of Figure 52 which shows a layout of the metal rig used to hold all components of the measurement in line. The wedges are aligned such that the divide between the two wedges is in line with the acoustically transparent boundary. A slot cut into the plate supporting the AM specimen below is made to center the receiving transducers along the length of the AM specimen. This slot allows for multiple receivers to be coupled to the combined AM specimen so that multiple mixing points can be measured without changing coupling conditions. Sonotech Ultragel II gel is used between all interfaces for coupling. A picture of the experimental setup with the probes and specimen in place is shown in Figure 53.

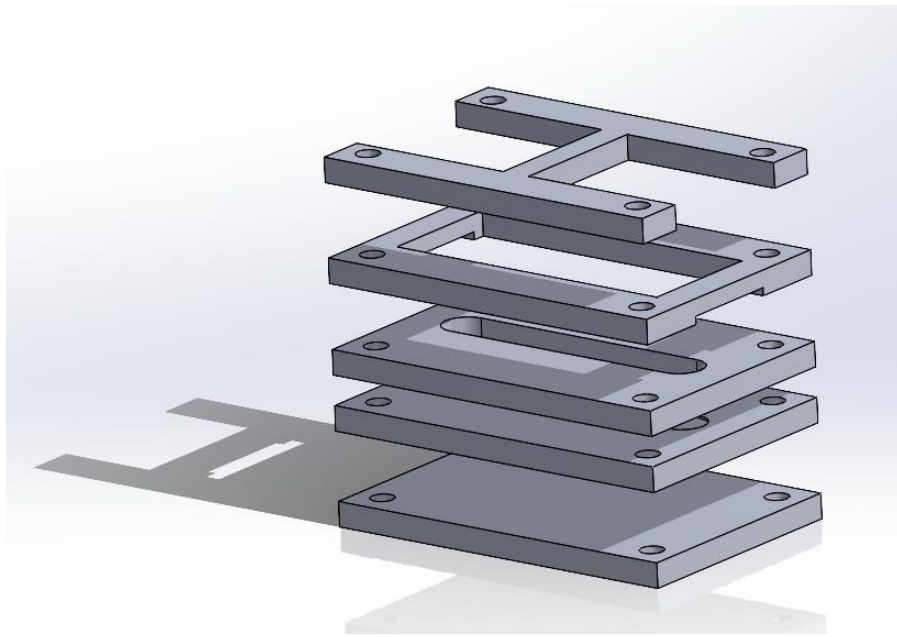


Figure 52: Stacked plates used to align phased array nonlinear mixing setup

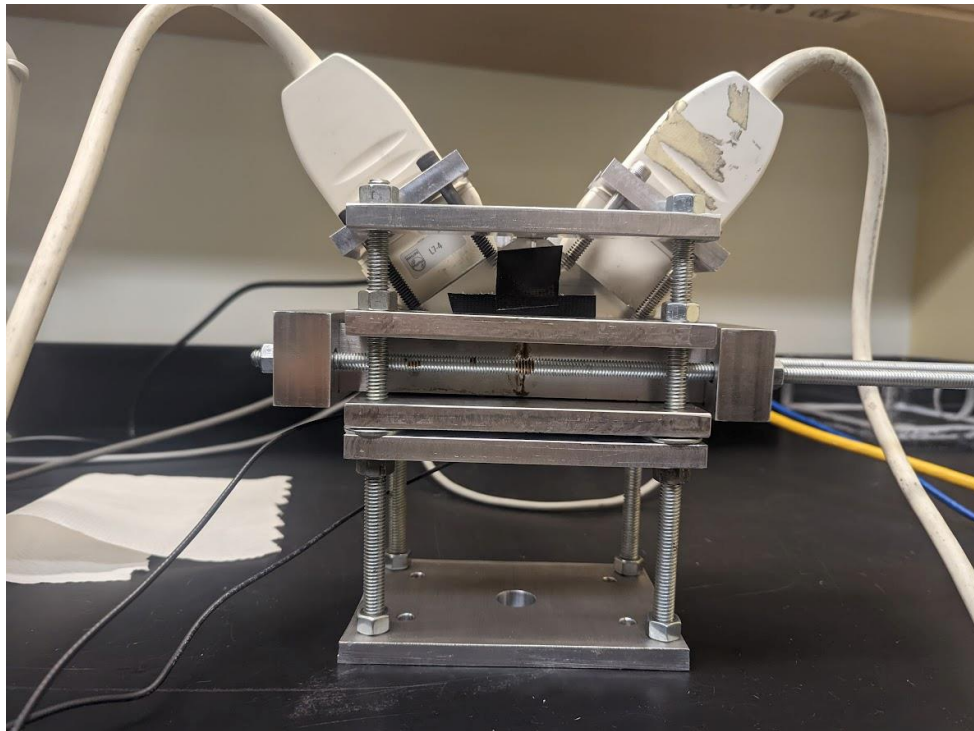


Figure 53: Experimental setup of phased array mixing in combined AM specimen

A scanning arc is calculated for the combined AM specimen for the mixing of two equal frequency incident shear waves. The arc is shown in Figure 54. The arc is not symmetric across the acoustically transparent boundary. A zoomed in section close to the boundary is shown in the insert. The subtle differences in wave speed between the two sides is accounted for in the generation of the arc in both halves. The scanning arc left of the acoustically transparent boundary in the nominally powered AM specimen is defined for a mixing angle of  $117.4^\circ$ . The scanning arc right of the acoustically transparent boundary in the underpowered AM specimen is defined for a mixing angle of  $116.8^\circ$ .

Four points are defined along the scanning arc. These points are located at various lengths along the arc starting from the left emitting receiver: Scanning Point 1 = 45%, Scanning Point 2 = 48%, Scanning Point 3 = 52%, Scanning Point 4 = 55%. Mixing points 1 and 2 are located within the nominally powered AM and mixing points 3 and 4 are in the underpowered side. By scanning along this arc, the sensitivity of the phased array-based setup to microstructural difference can be assessed.

The shortened wedges used in this setup allow for the two emitting points (marked at the top of the specimen in Figure 54) to be closer. The smaller wedge separation defines the scanning arc to have a shallower depth which is necessary to conform to the geometric restrictions of this material. The locations of the two receiving transducers are drawn with blue and red squares that are centered at the calculated center of the mixed waves intersection with the bottom of the specimen.

The timing delay for both phased arrays is based on the speed of sound of the side to which the wedge is coupled. The steering angle used in the calculation of the timing delay accounts for the discontinuity in the scanning arc.

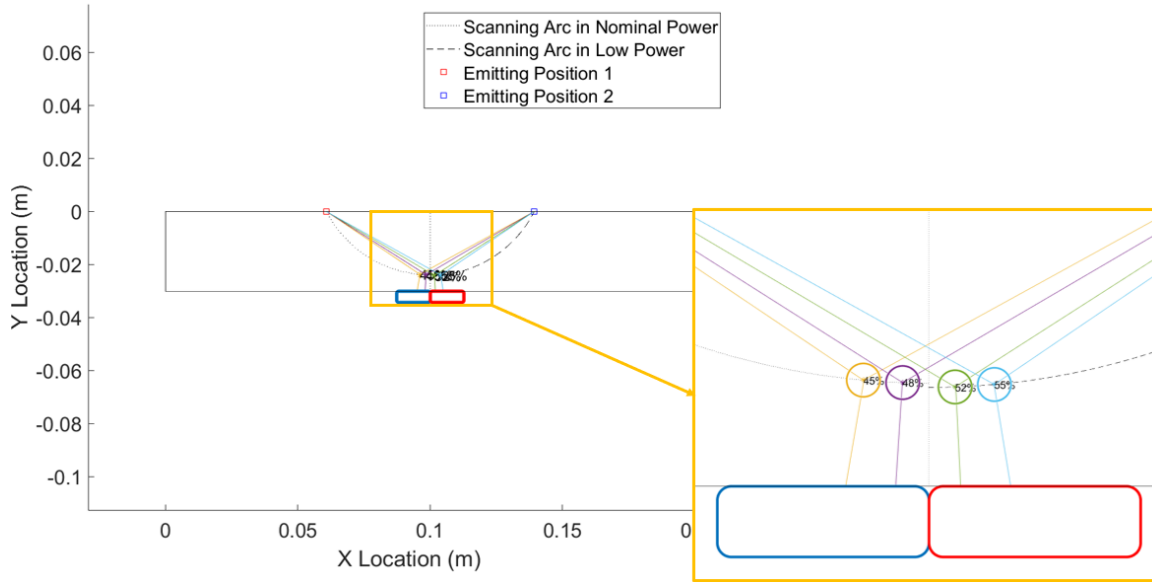


Figure 54: Scanning arc for combined AM specimen with insert near boundary

#### 4.5.7.2 Volume of Mixing

The measured  $\beta'$  of a material resulting from nonlinear mixing with phased arrays is compared between the two sides of the combined specimen. To compare this result from a scanned measurement with phased arrays, changes to the volume of the mixing zone must be accounted. Recall from Equation 59 that the amplitude of scattered wave is dependent on the mixing volume. The volume of the mixing area is determined by the overlapping volume of the two incident waves. In Figure 54, the scanning points are shown with a circle whose radius is approximately proportional to the scanning volume. For each of the mixing points defined, the mixing volume is wholly contained within one half of the combined specimen. Therefore, the resulting resonant wave is influenced by solely one AM material.

The scanning volume or mixing resolution can be found from the intersection area of the two mixing shear wave packets that are defined by the geometry below. The length of the wave packet is defined by number of cycles ( $n$ ) of the input tone burst and the wavelength ( $\lambda$ ) of the fundamental frequency [17], [45]. The width of the packet is defined

by the active area of the phased array,  $A$ , the steering angle required for the current mixing point,  $\theta_s$ , and the wedge angle  $\theta_{wedge}$ . The volume of mixing is estimated by the overlapping interaction area of these two wave packets at the mixing point as shown in red in Figure 56. The volume of interaction changes as a function of time as the two wave packets pass through each other. A numerical computation for this area must be used as no closed form solution exists for the area of an arbitrary polygon changing over time [17]. The depth into the page is assumed to be constant and used for calculation of a mixing volume from the overlap of the two packets. A sphere with equivalent volume is defined as the mixing resolution sphere. An approximate volume of  $0.098 \text{ cm}^3$  is estimated for the experimental setup defined in this section when the mixing point is located at the center of the two wedges. This is the volume for which the microstructure is evaluated at a mixing point to result in a given value of  $\beta$ .

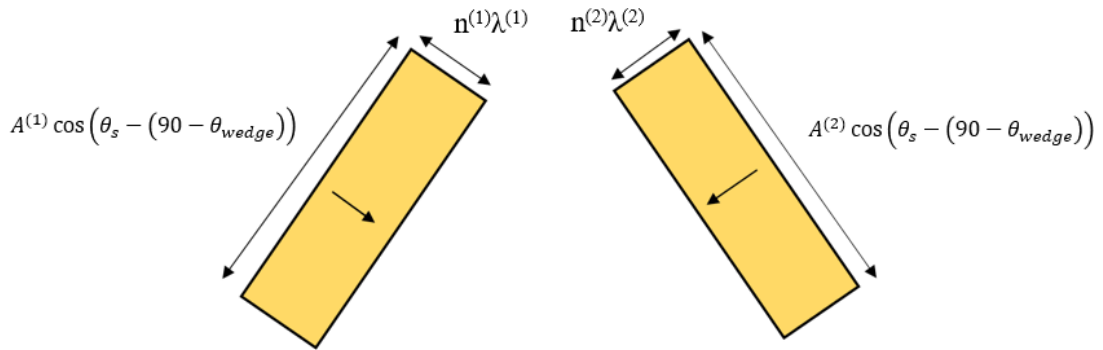


Figure 55: Mixing packet size definition

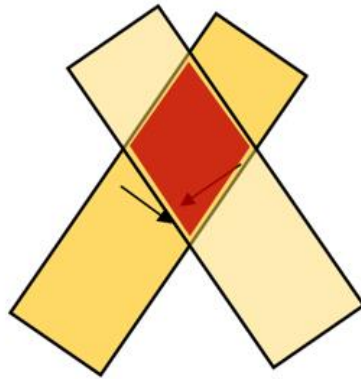


Figure 56: Mixing area defined by overlapping incident waves.

#### 4.5.7.3 In Stack AM Specimen

The AM specimen shown in Figure 25 which is comprised of three distinct layers is then measured with the phased array based nonlinear wave mixing technique. A scanning arc generated with the emitting points as far away from one another as geometrically possible is shown in Figure 57. At this max separation, the scanning arc does cross into the middle layer of the stacked specimen. However, mixing points along this arc in the top layer would propagate at an oblique angle towards the vertical edges of the specimen. Detection of the scattered wave when mixing occurs in the top layer is not made in this work.

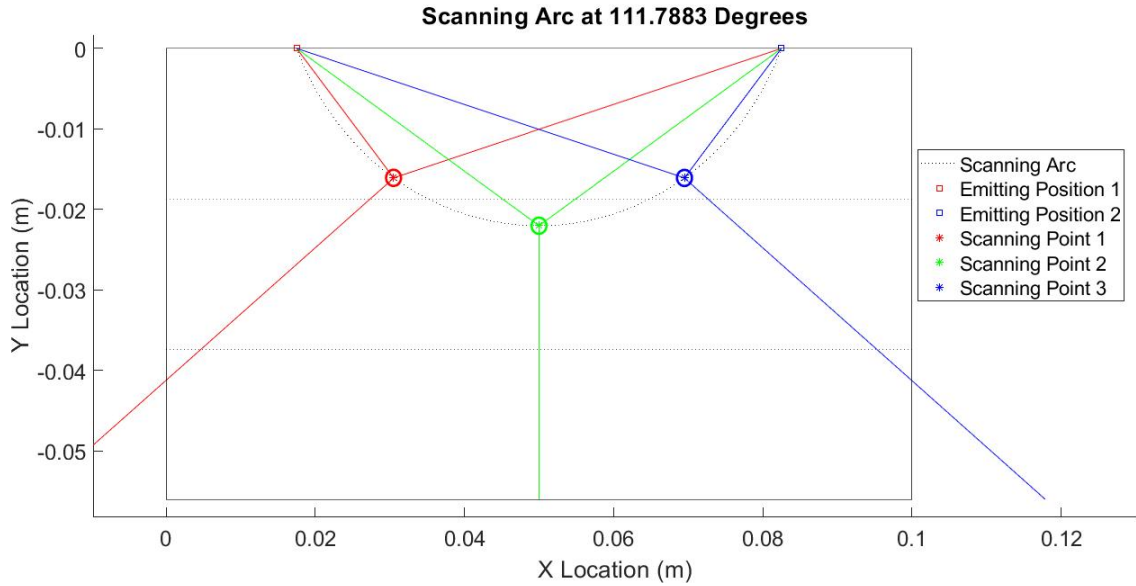


Figure 57: Scanning arc for stacked AM specimen

#### 4.6 Bulk Material Nonlinearity

The following experimental setup is used to measure an acoustic nonlinearity parameter in a longitudinal setup. This measurement technique has been previously used for the characterization of microstructure in stainless steels [11], [12]. The measurement technique is based upon the principles of second harmonic generation (SHG) [19]. The acoustic nonlinearity parameter recorded from this measurement set is not equal to the  $\beta$  measured from nonlinear mixing. To distinguish between the two values, the measured nonlinearity from this bulk second harmonic generation technique is denoted as  $\beta_{SHG}$ . The third order elastic constants that influence  $\beta$  and  $\beta_{SHG}$  are not completely shared. This setup gives a value of  $\beta_{SHG}$  that is averaged over the entire thickness of the specimen unlike the localized nonlinearity provided from nonlinear wave mixing. The measurement is done to complement the set of results from nonlinear wave mixing and to verify the trends seen from mixing.

A setup shown in Figure 58 is used to propagate a longitudinal wave through the thickness of a tested specimen. A 20-cycle sinusoidal tone burst centered at 2.25 MHz is generated and amplified by a RITEC RAM-5000 gated amplifier. The signal is transmitted through the test specimen with a Panametrics V106 (centered at 2.25 MHz) contact transducer. The received signal is recorded with a Valpy Fisher CF050404LN which is centered at twice the fundamental frequency at 5 MHz. The received signal is averaged 258 times for an increase in signal to noise ratio. The measurement is then repeated with an increased input amplitude. Each measurement iteration is preceded by a one level increase of excitation from the RITEC system. A total of 19 recordings are made for each measurement.

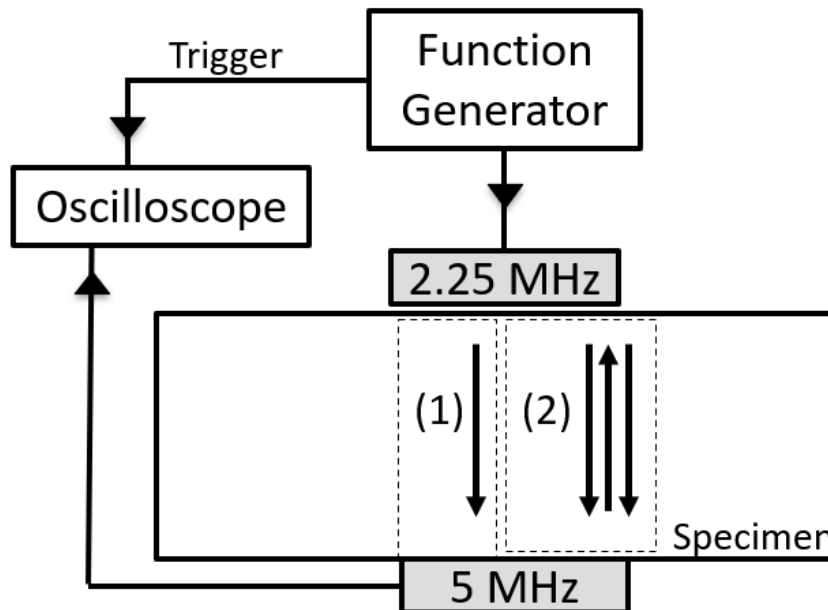


Figure 58: Through NLU measurement schematic

A stable region of the time domain signal is selected for each recording to avoid transient effects. The amplitude of the first  $A_1$  and second harmonic  $A_2$  within this region is measured and shown in Figure 59.  $A_2$  is plotted as a function of  $A_1^2$  in Figure 60. A linear fit is applied to this relation. The slope of this line is proportional to  $\beta_{SHG}$ .

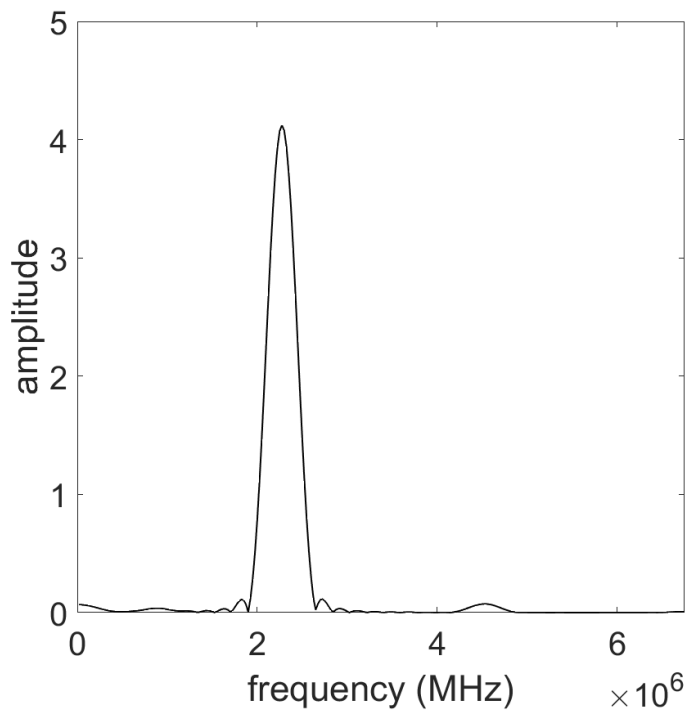


Figure 59: Fundamental and second harmonic of through NLU measurement

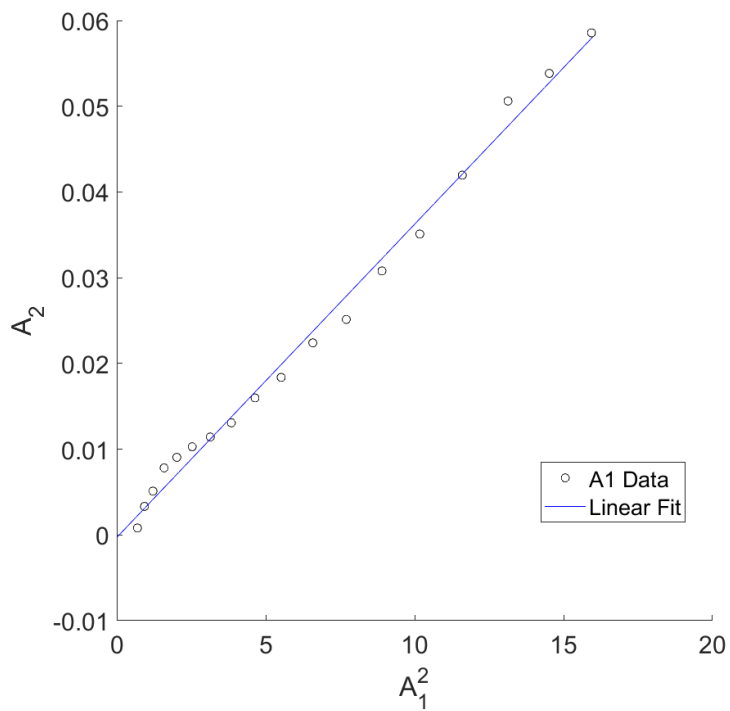


Figure 60:  $A_2$  vs  $A_1^2$ . Slope is  $\beta_{SHG}$

## **CHAPTER 5. RESULTS AND DISCUSSION**

### **5.1 Overview**

Experimental results from each measurement set are presented in this section. A discussion of the key points from each result is also given. First, the linear ultrasonic measurement results, velocity and attenuation, are shared. The velocity measurements are important to the development of the nonlinear mixing measurements and the sensitivity of the mixing setup to speed of sound is discussed. The sensitivity of these linear ultrasonic measurements to microstructural changes is compared to the nonlinear techniques. The result of each NLU setup is then presented.

### **5.2 Phase Unwrapping Velocity Results**

Averaged from approximately 20 measurement sets, the longitudinal and shear speeds of sounds were found for the test materials as shown in Table 6. Accuracy in these speed of sound measurements is of high importance to the success of the nonlinear wave mixing with phased arrays. The sensitivity of nonlinear mixing setups and especially the setup developed in this work using phased arrays is discussed in Section 0.

Table 6: Speed of Sound Results for Materials used in Mixing Setups

	<b>Longitudinal Speed of Sound <math>\left(\frac{m}{s}\right)</math></b>	<b>Shear Speed of Sound <math>\left(\frac{m}{s}\right)</math></b>
<b>Aluminum Block</b>	6390.9	3127.4
<b>Nominal 316L PBF (214W)</b>	5729.8	3217.4
<b>Underpowered 316L PBF (160W)</b>	5745.7	3071.3
<b>Rexolite® 1422</b>	2362.2	Unused
<b>Acrylic Sheet used for Wedges</b>	2707.9	Unused

Accurate measurements for the acrylic material used for the mode conversion wedges were of high importance to ensure the timing and steering of the phased array setup. The Clear Scratch- and UV-Resistant Cast Acrylic Sheet from McMaster-Carr® [77] was found to have a longitudinal speed of sound of 2707.9 m/s. Shear speed of sound is not needed in this material for this setup as the phased array transducers inputting the ultrasonic signal are longitudinal in nature. The mode conversion from a longitudinal to shear wave occurs at the boundary of the acrylic wedge and the tested material. Similarly, Rexolite® 1422 was used in the manufacturing of the wedges used in the single element mixing setups for its low speed of sound [78]. The longitudinal speed of sound reported by the manufacturer was found to be accurate [79].

### 5.2.1 Theoretical Effects of Porosity on Speed of Sound

One observation which can be made from Table 6 is in the comparison of the 316L PBF sound velocities. The nominally powered 316L PBF (214 W) was measured to have a lower longitudinal speed of sound than the underpowered 316L PBF (160 W). This comparison and the error of the longitudinal measurements can be seen in Figure 61. Note the percent change in longitudinal wave speed is 0.23%. Conversely, the nominally powered specimen was measured to have a higher shear wave velocity than the underpowered specimen as seen in Figure 62. The increase in transverse wave speed is much higher with a 4.6% difference.

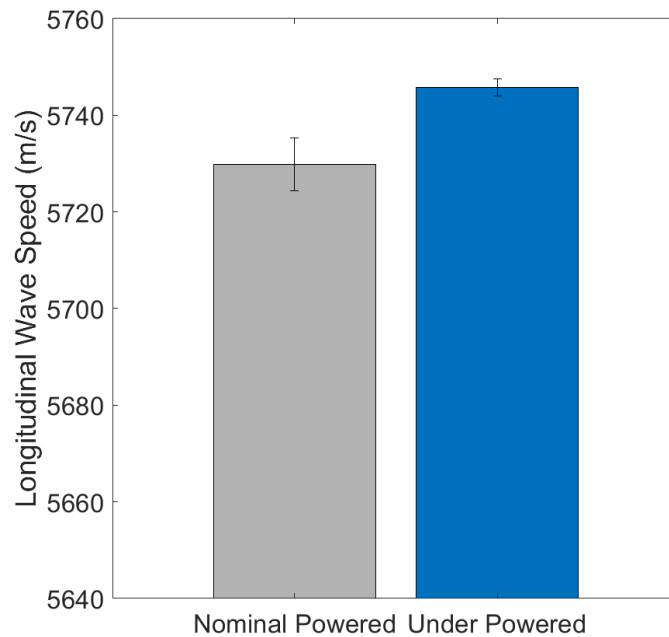


Figure 61: Comparison of longitudinal wave speed between nominal and underpowered 316L PBF specimens

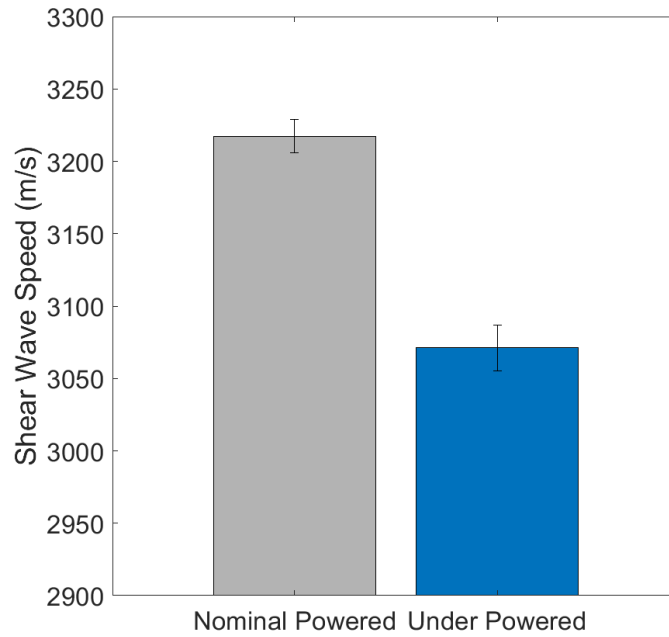


Figure 62: Comparison of transverse wave speed between nominal and underpowered 316L PBF specimens

Numerous microstructural features can effect wave velocity including texture and porosity [80]. In the formulation for both wave speeds, an increase in porosity (decrease in density) is expected to increase the wave speed. The difference in change seen in transverse and longitudinal wave speeds may be explained by the irregular shape of the lack-of-fusion porosity.

$$C_L = \sqrt{\frac{E(1 - \nu)}{\rho(1 + \nu)(1 - 2\nu)}} \quad (83)$$

$$C_T = \sqrt{\frac{G}{\rho}}$$

### 5.2.2 *Sensitivity of Mixing Setup to Variation in Speed of Sound*

Highly accurate measures of both longitudinal and shear speed of sound in the test material is important for the development of a phased arrays based nonlinear wave mixing setup. Small errors to both speeds of sound but particularly the material shear speed are compounded throughout the development process. As seen in Equation 56, the theoretical nonlinear mixing angle is dependent on the ratio of longitudinal to shear speed in a material. The sensitivity of the mixing angle to shear speed is seen in Figure 63. This sensitivity is a significant challenge to nonlinear mixing setups regardless of transducer type or scanning capabilities. In immersion setups using single element transducers, small adjustments to the angle of propagation can be easily made to account for any errors.

Sensitivity challenges are compounded when using phased arrays as the scanning path and array timing are additionally sensitive to the wave velocity. The scanning arc is defined by the mixing angle and the location of measurement, defined by the propagation path of the mixed wave, is dependent upon the shape of the scanning arc.

The timing delay between phased array elements needed for beam steering capabilities is also dependent on the wave velocities. In Equation 68, the internal angle of the wedge-phase array setup is determined by Snell's Law and the theoretical mixing angle. Figure 64 shows a representation of the sensitivity of timing between elements as a function of percent change in shear wave velocity for the 316L PBF mixing setup. 1-2% error in the shear speed of a material could mean that the beam is steered in a significantly wrong direction and that the two incident waves in the nonlinear mixing setup will not intersect at the required angle. Small error in wave speed can lead to failure of a nonlinear wave mixing measurement with phased arrays as shown in Figure 88 in Section 5.5.3.1.

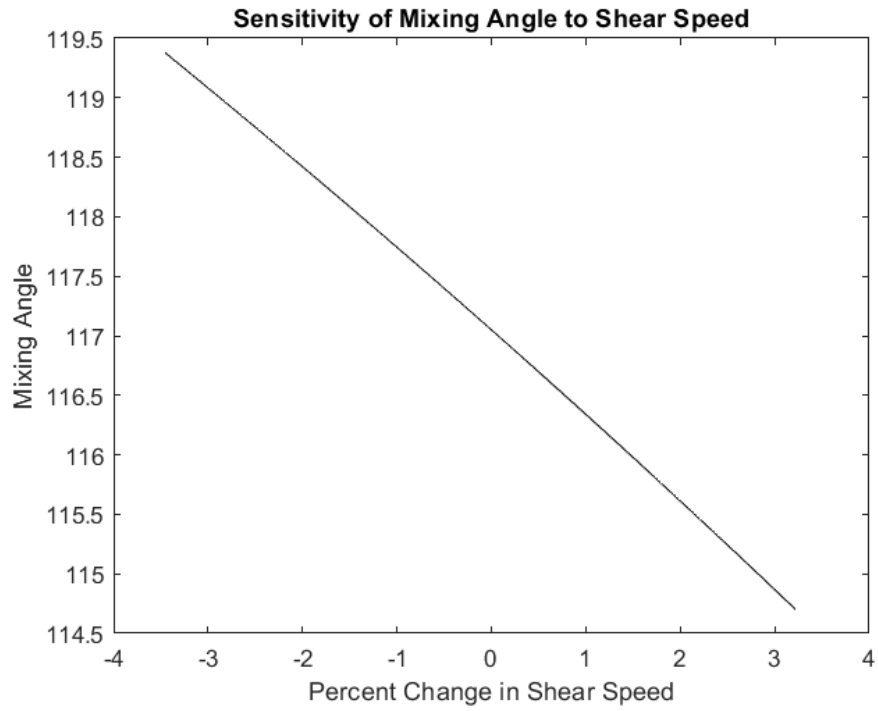


Figure 63: Sensitivity of mixing angle to change in shear speed

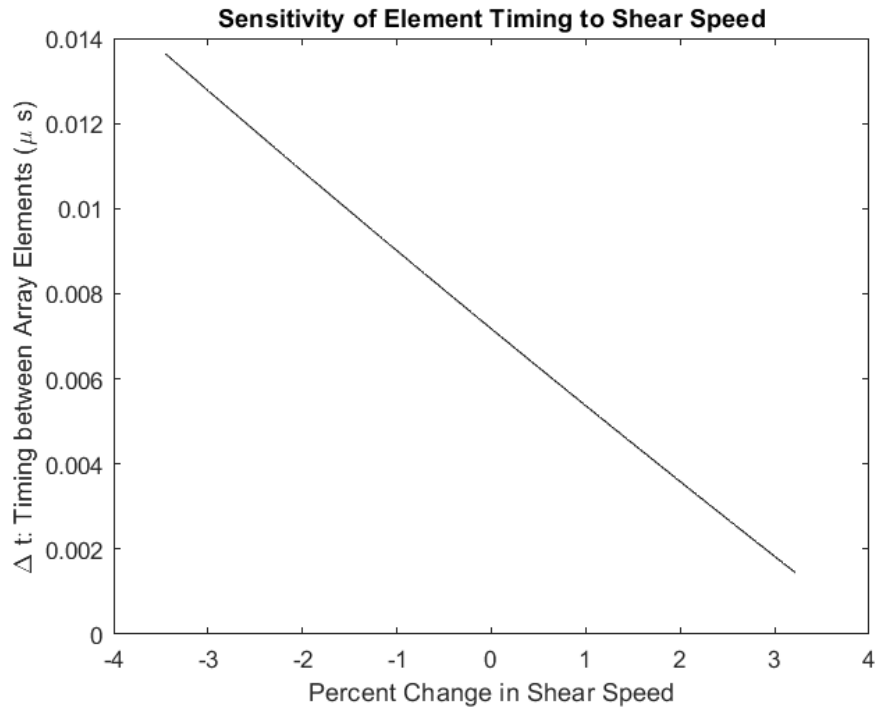


Figure 64: Sensitivity of timing between elements to change in shear speed

### 5.3 Attenuation Measurement

Relative attenuation values in the nominal and underpowered AM specimens are compared in Figure 65. The nominal specimen is measured to have a relative attenuation of  $139 \frac{np}{m}$  and the underpowered specimen at  $202 \frac{np}{m}$ . The percent difference between these two measures is 37%. The underpowered specimen was theorized to have higher attenuation due to the increase in lack-of-fusion porosity. Microstructural pores can cause scattering of an acoustic wave.

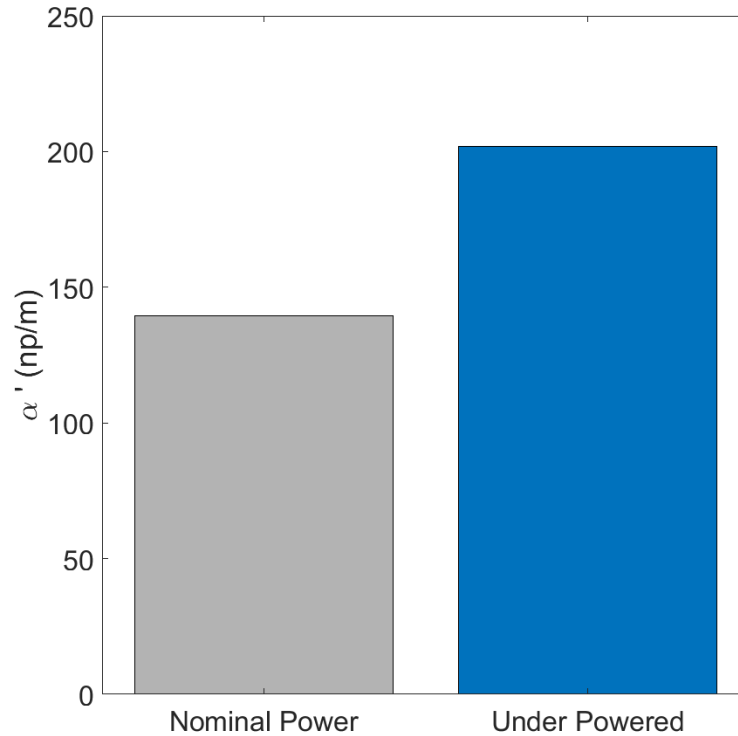


Figure 65: Comparison of relative attenuation between nominal and underpowered AM

## 5.4 Mixing Single Element

The results of nonlinear mixing with single element transducers are discussed in this section. First the results for nonlinear mixing in the homogenous AM material is shared to show the effectiveness and necessity of the four-way polarity flipping technique in metals. Then the results from the aluminum block are shared along with the laser vibrometer results in this specimen. A discussion is presented on the experimental improvements made from the vibrometer results. Then the results from the concrete specimen are shared including the mapping ability of acoustic nonlinearity that is possible with nonlinear wave mixing. The final result is of the heterogeneous AM material where measurement across the acoustically transparent boundary is shown.

### 5.4.1 Single Element Mixing Results in Homogenous AM Material

The received signal of the positive-positive polarity combination for single element nonlinear wave mixing in the nominally powered AM specimen is shown in Figure 66. This is the measured signal following the inline amplification, bandpass filtering (centered at 10 MHz), and averaging. Recall that the mixed wave for this setup is calculated to have a frequency of 10 MHz ( $\omega_r = \omega_1 + \omega_2$ ). The two vertical dashed lines are the expected time of arrival for the mixed wave (left line) and the 1<sup>st</sup> reflection of the mixed wave (right line). The expected time of arrival of the mixed wave is calculated by:

$$t_{expected} = \frac{d_{wedge}}{c_{l,rexolite}} + \frac{d_{shear\ in\ solid}}{c_{s,AM1}} + \frac{d_{mixed\ wave}}{c_{l,AM1}} \quad (84)$$

where  $d_{wedge}$  is the measured distance of the transmitted wave in the wedge.  $d_{shear\ in\ solid}$  and  $d_{mixed\ wave}$  are found by trigonometric determination of the mixing point based on the propagation angle and the separation distance between the wedges. No indication of a large amplitude at 10 MHz is shown at the expected time of arrival of the mixed wave in Figure 66.

The measured result from each of the four polarity combinations is shown Figure 67. The result from each polarity combination shows a similar form with no significant amplitude at the expected time of arrival. In Figure 68, the time domain result following the implementation of the four-way polarity flipping is plotted. Recall that the four-way polarity flipping routine is intended to suppress nonlinearities (resulting in second harmonics at 10 MHz) that are unassociated with mixing. The result in Figure 68 is therefore the result of nonlinear mixing. A significant peak in amplitude is found at approximately 22  $\mu$ s which coincides with the expected time of arrival for the mixed wave.

The same result following four-way polarity flipping for the single element nonlinear mixing setup in the underpowered AM is shown in Figure 69. Again, the result shows a significant amplitude at the expected mixing time indicating the strong presence of a scattered wave resultant from nonlinear mixing.

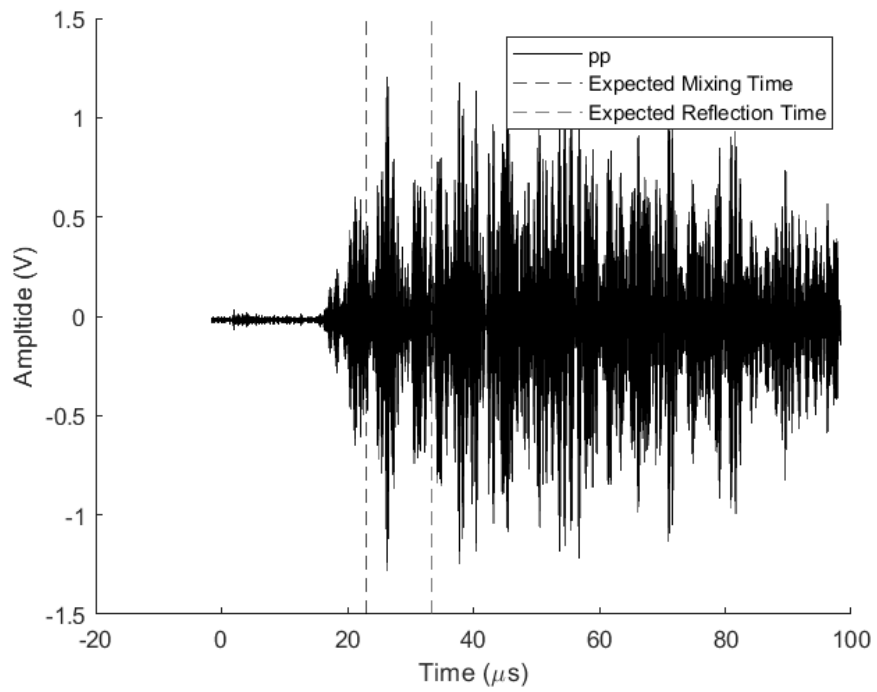


Figure 66: Positive-positive result with single element in nominally powered AM

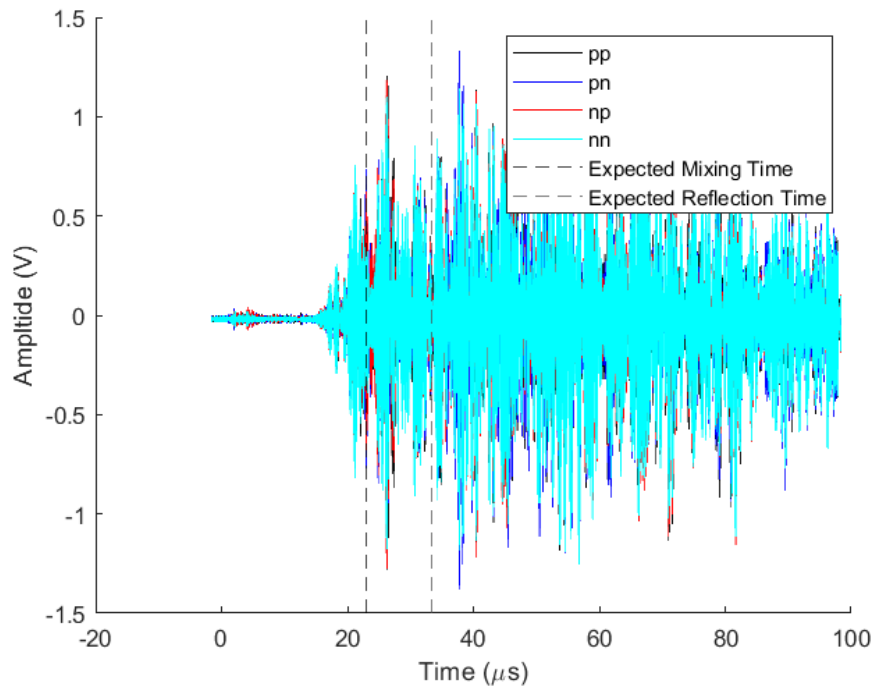


Figure 67: All polarity combinations for single element mixing in nominally powered AM

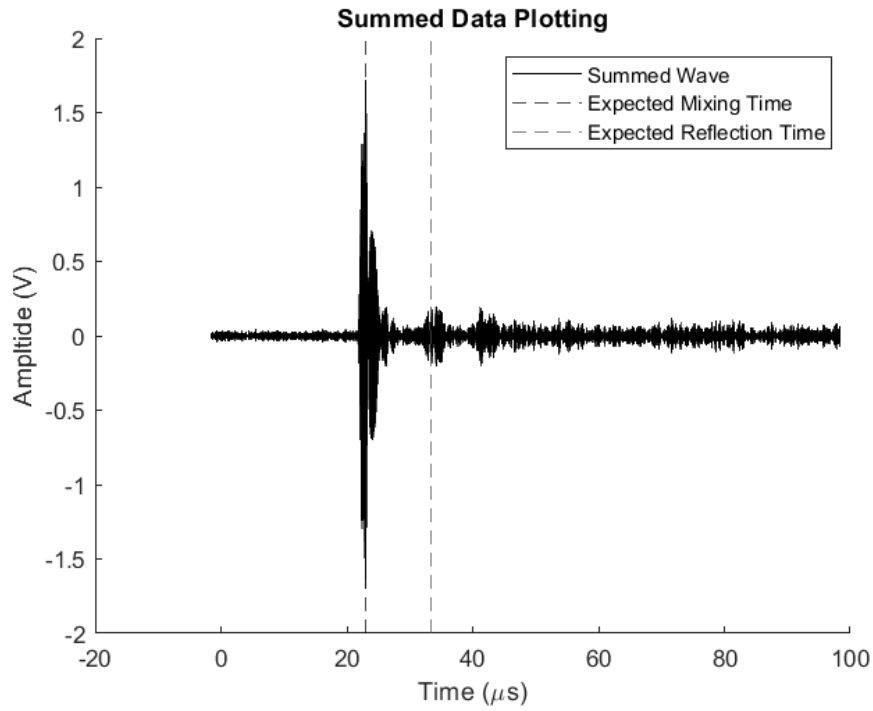


Figure 68: Nominally powered AM: mixed wave following four-way polarity flipping for single element mixing

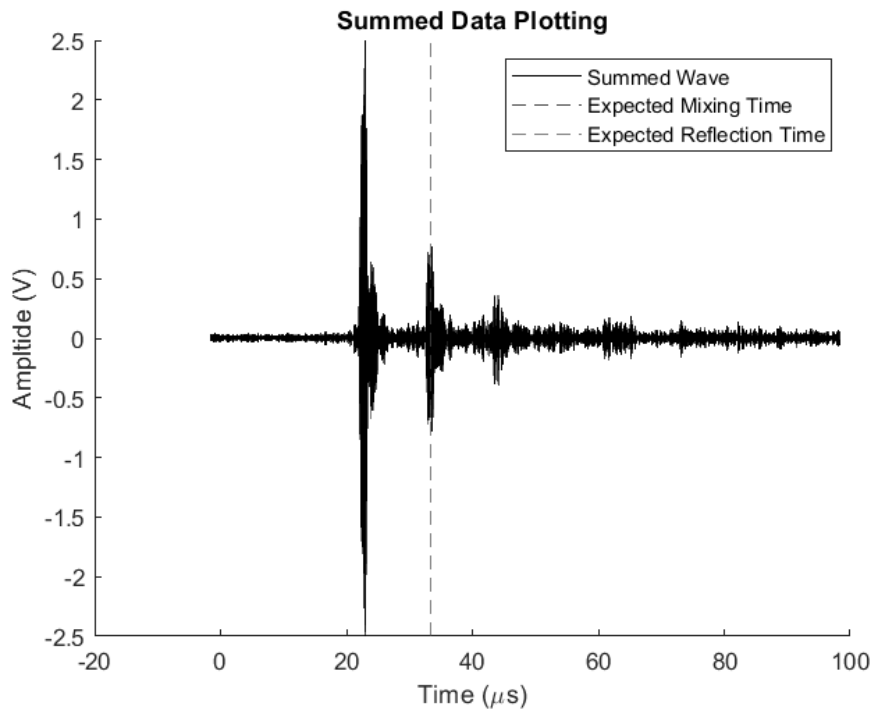


Figure 69: Underpowered AM: mixed wave following four-way polarity flipping for single element mixing

Without correction for diffraction, the amplitude of the mixed wave in the underpowered AM specimen is higher than that in the nominally powered specimen. A comparison of the quantification of  $\beta$  with diffraction correction is shown in Figure 70. As theorized, the acoustic nonlinearity in the underpowered specimen with increased lack-of-fusion porosity is higher ( $\beta' = 16.54$ ) than the nominal specimen ( $\beta' = 7.89$ ). The percent difference between these two measures is 71% which is substantially higher than the percent differences of the linear acoustic measures of velocity and attenuation. This follows the expected result that nonlinear wave mixing is more sensitive to microstructural changes than linear measures which are not sensitive to microstructural characteristics smaller than the linear wavelength. A comparison of the sensitivity between the two materials of the linear ultrasonic measures and  $\beta$  from nonlinear wave mixing is shown in Figure 71.

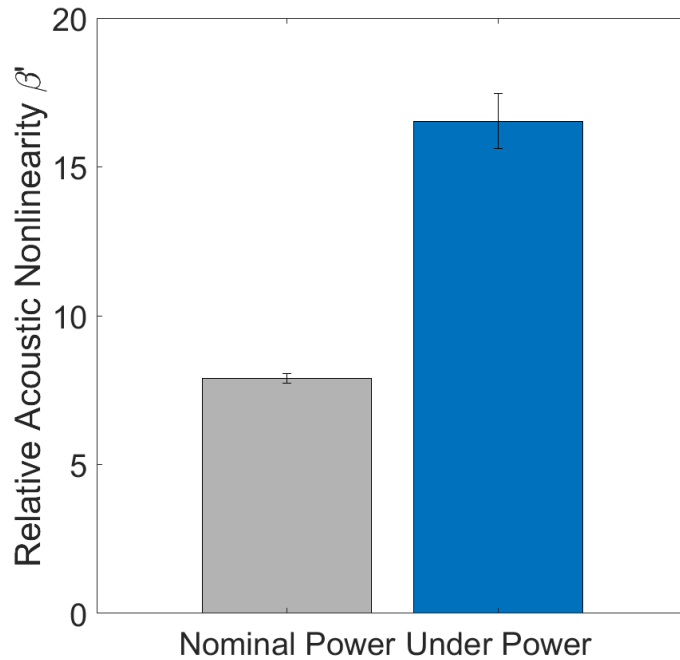


Figure 70: Comparison of relative acoustic nonlinearity measured on AM specimens with single element nonlinear wave mixing setup

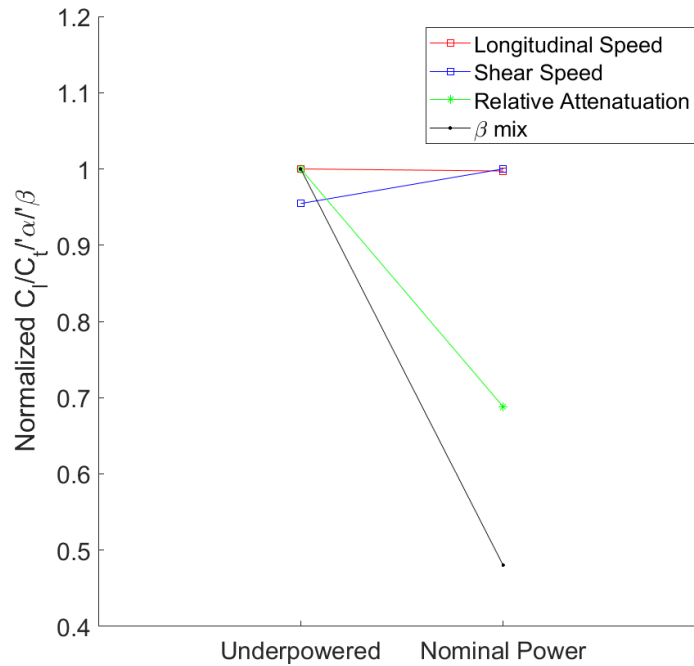


Figure 71: Comparison of sensitivity of ultrasonic measures between material states with different porosity

#### 5.4.2 Single Element Mixing Results in Aluminum Block

Effective nonlinear mixing is shown from the single element mixing setup in the aluminum block. The result following four-way polarity flipping is shown in Figure 72. Again, a large peak in measured amplitude is shown at the expected time of arrival of the mixed wave. As the aluminum block is a generally homogenous specimen, no comparison of  $\beta$  can be made to provide valuable information.

As discussed in Section 4.4.1.1, a proof for the presence of mixing can also be performed by comparing the measured signal when both emitting transducers are turned on simultaneously to the summed response of the signal when both transducers are turned on independently. A set of these results is shown in Figure 73 where the red and blue time domain signals are resultant from the two emitting transducers turned on independently.

The measurement for the case in which both transducers are emitting simultaneously is identical to the positive-positive polarity case used for the four-way polarity flipping measurement.

This proof may be extraneous in cases like Figure 72 where a strong peak is shown at the expected time of arrival of the mixed wave following four-way polarity flipping. However, in cases where the 10 MHz signal is noisy, this routine can give valuable insight into the success of nonlinear wave mixing. Comparisons like Figure 73 are made for all nonlinear mixing setups discussed in this thesis, but as they are intermediate results they are not included.

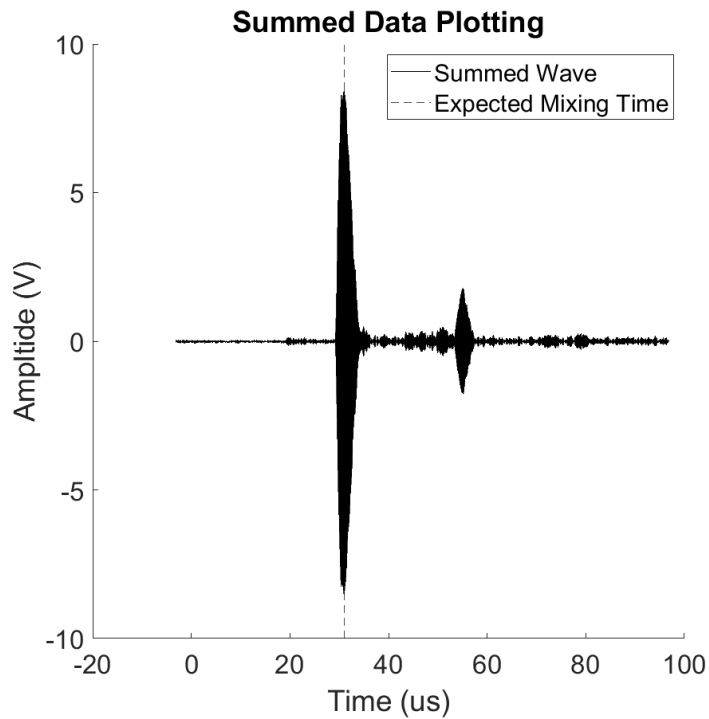


Figure 72: Mixed wave following four-way polarity flipping for single element mixing in aluminum block

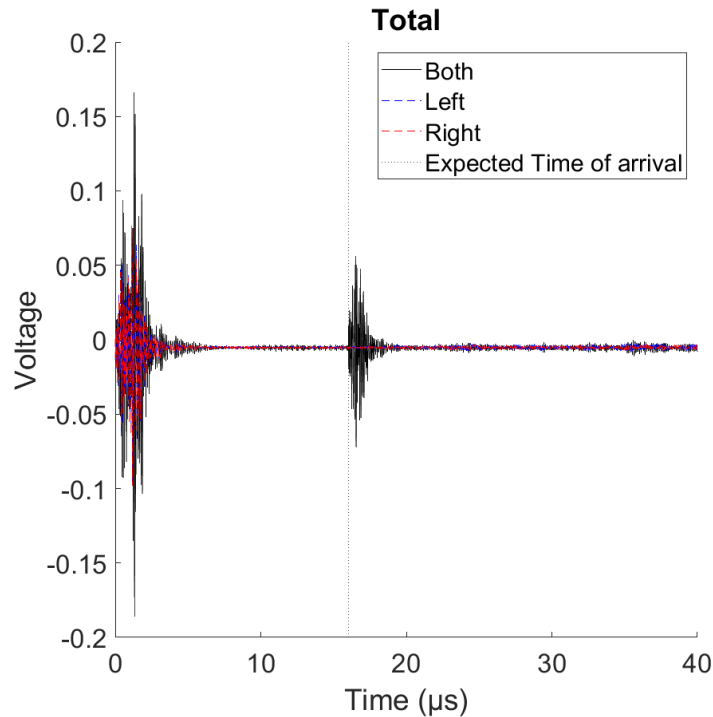


Figure 73: Excitation of emitting transducers independently and simultaneously

#### 5.4.2.1 Laser Vibrometer Results

An important set of results from the single element based nonlinear wave mixing setup in the aluminum block is from the corresponding laser vibrometer results. Progression of the wave through the mode conversion wedges and into the specimen was visualized in all three directions. Wave motion is better visualized with video but can still be shown in the single frame shown in Figure 74. In this visualization, pixel color corresponds to the summed amplitude of particle motion in all three directions, with lighter color indicating an increase in particle motion. The peak of the wave can be tracked through the setup. The propagation of the mixed wave is not easily visible as it is overlapped by the motion of unconverted longitudinal waves and shear waves from reflections within the wedge.

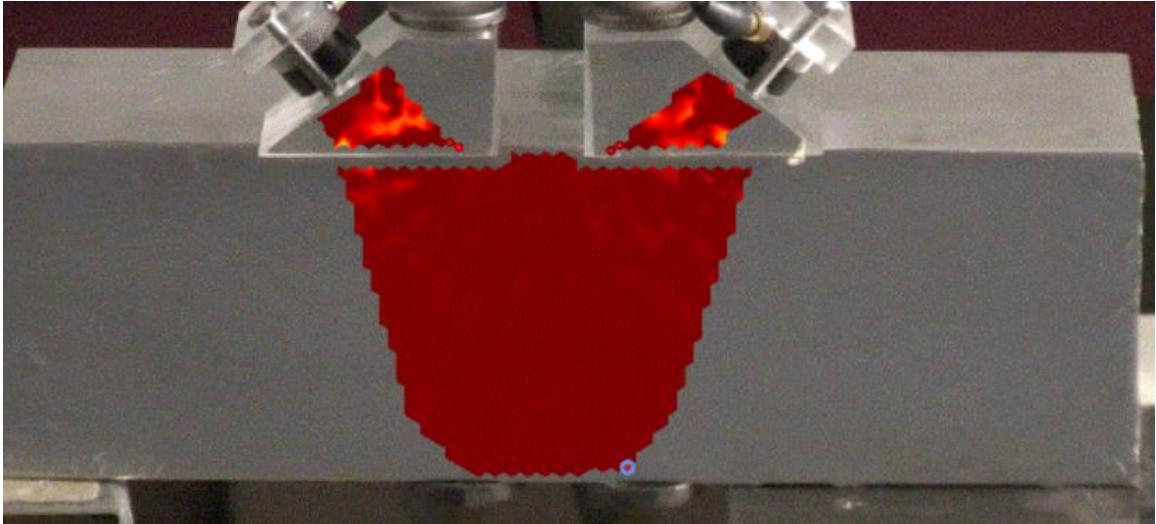


Figure 74: Single frame of wave propagation for single element nonlinear wave mixing in aluminum block

As previously discussed in Section 4.5.4, the results from the laser vibrometer inspired redevelopment of many of the mode conversion wedges used for nonlinear wave mixing in this work. Reverberations within the unimproved wedges are seen within the wedge in Figure 75. Reflections within the wedge enter the specimen after the intended incident wave. The time domain of the highlighted voxel in Figure 75 is shown in Figure 76, showing the introduction of reflections after the majority of the incident wave passes towards the mixing point.

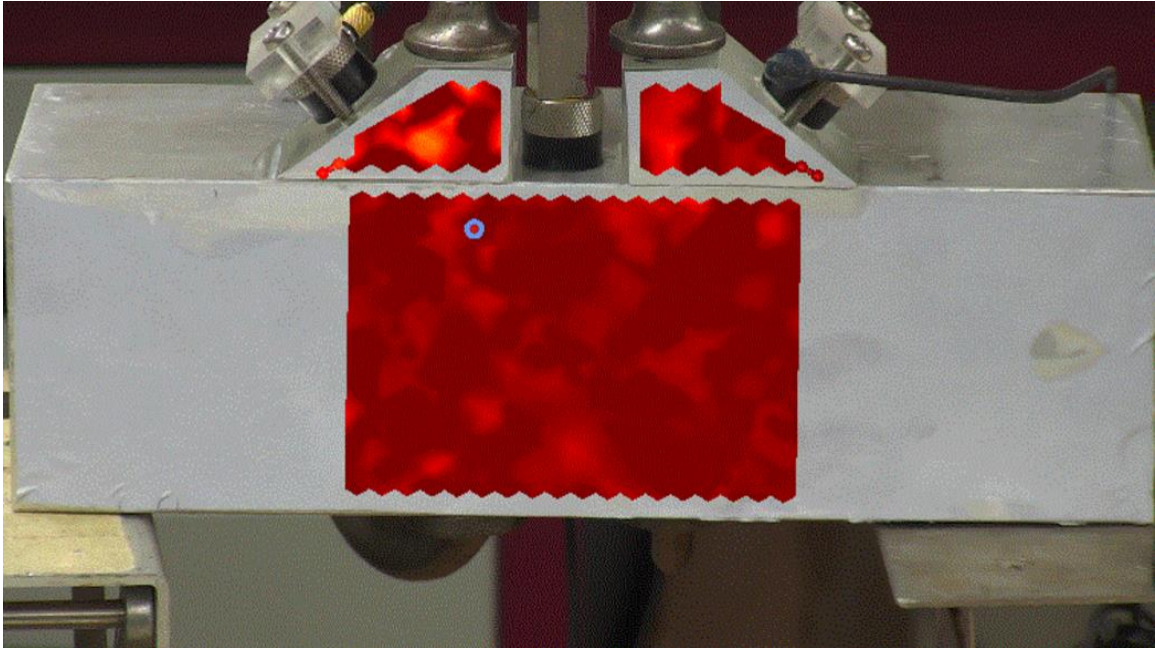


Figure 75: Laser vibrometer single frame showing reverberations in the mode conversion wedge

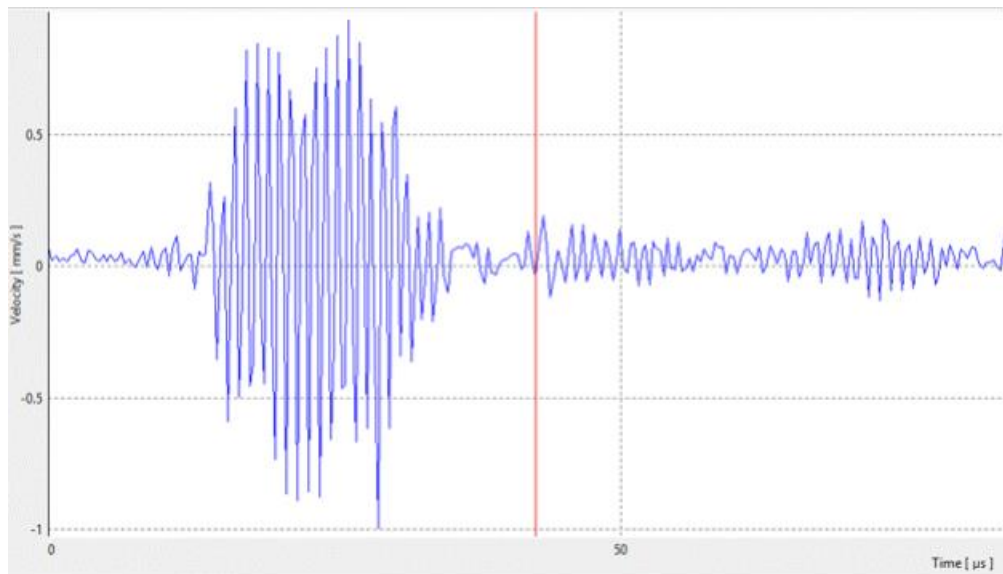


Figure 76: Corresponding particle motion of highlighted voxel in Figure 75 showing the existence of reverberations from the wedge entering the specimen.

### 5.4.3 *Single Element Mixing Results in Concrete*

The results of single element mixing in the concrete specimen are covered in detail in [57]. Three images are overlaid over the concrete specimen in Figure 77. Each image is the result of 25 measurements made at the cross section of the concrete specimen corresponding from left to right to ASR damage, no damage, and fire damage. The scan for the two damage areas is centered on the known location of damage inserted into the cast concrete specimen. In both cases of damage, significant increase in the acoustic nonlinearity parameter is found corresponding to the location of damage. Sensitivity of the acoustic nonlinearity parameter is shown in Figure 78.  $\beta$  increases significantly for nonlinear mixing when the mixing volume contains ASR and fire damage.

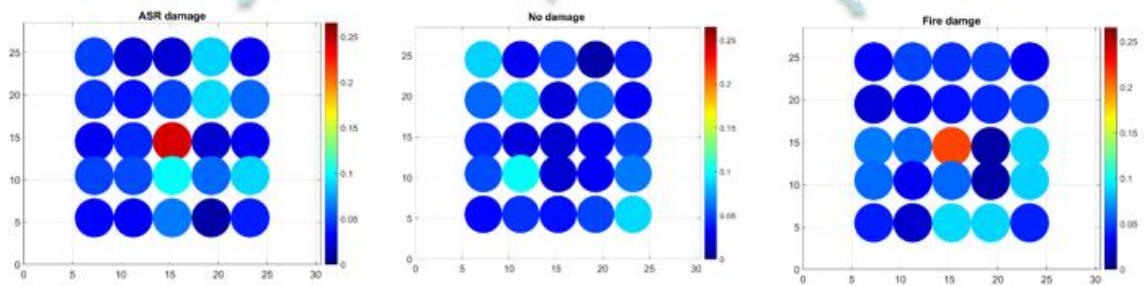
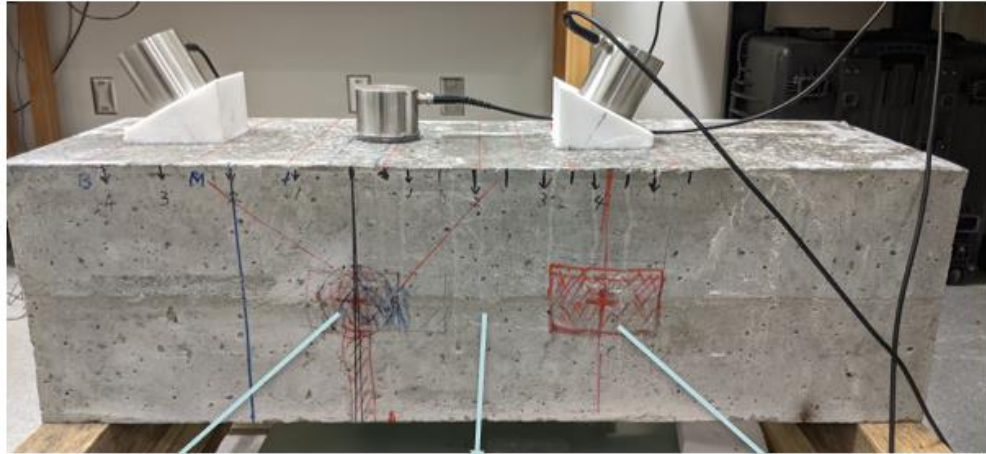


Figure 77: Acoustic nonlinearity scanned in cross sections corresponding to regions with ASR damage, no damage, and fire damage

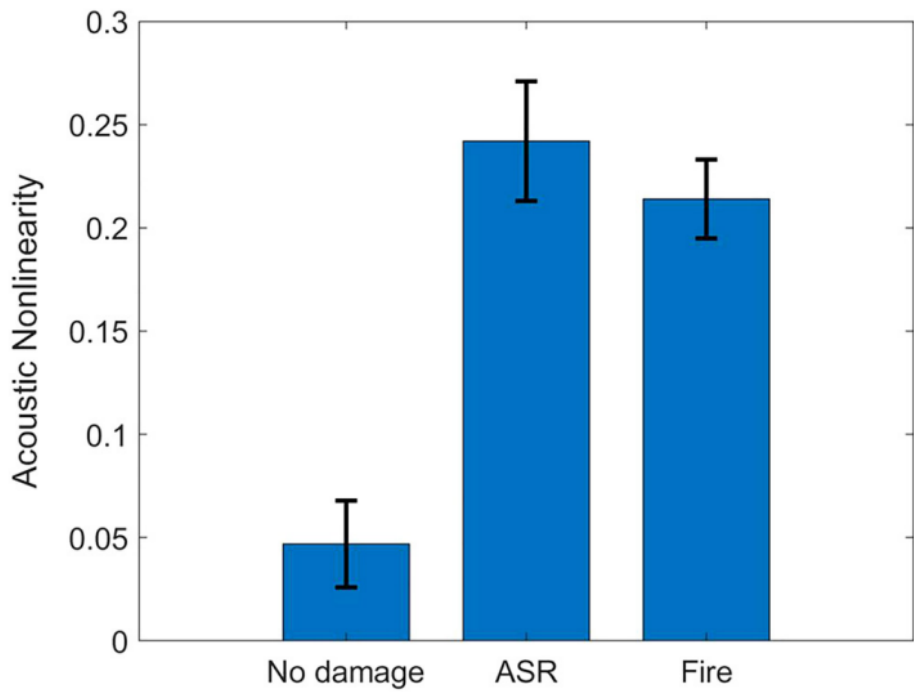


Figure 78: Comparison of acoustic nonlinearity at points within the concrete specimen containing no damage, ASR, and fire damage

#### 5.4.4 *Single Element Mixing Results in Heterogeneous AM Material*

##### 5.4.4.1 Across Acoustically Transparent Boundary

The results of the measurements across the acoustically transparent boundary as described in Section 4.4.4.1 are discussed in this section. The time domain signal following four-way polarity flipping when the mixing point is located in the nominally powered AM specimen is shown in Figure 79. This measurement matches the schematic drawn in Figure 40a. The matching result corresponding to Figure 40b where the mixing point is located in the underpowered AM specimen is shown in Figure 80.

Comparison of  $\beta$  between the measurement on both sides of the boundary is presented in Figure 81. The same trend presented in the homogenous AM specimens are shown here:  $\beta' = 15.6$  when mixing occurs in the underpowered section compared to  $\beta' = 7.81$  in the nominally powered section. The measured  $\beta'$  in each section is within the error of the results from homogeneous mixed specimen where  $\beta' = 16.54$  in the underpowered specimen and  $\beta' = 7.89$  in the nominal. This follows the expected outcome as  $\beta'$  is dependent on the material contained within the mixing volume and not influenced by the path of the incident waves. The characterization done with the nonlinear wave mixing technique is local to the mixing volume.

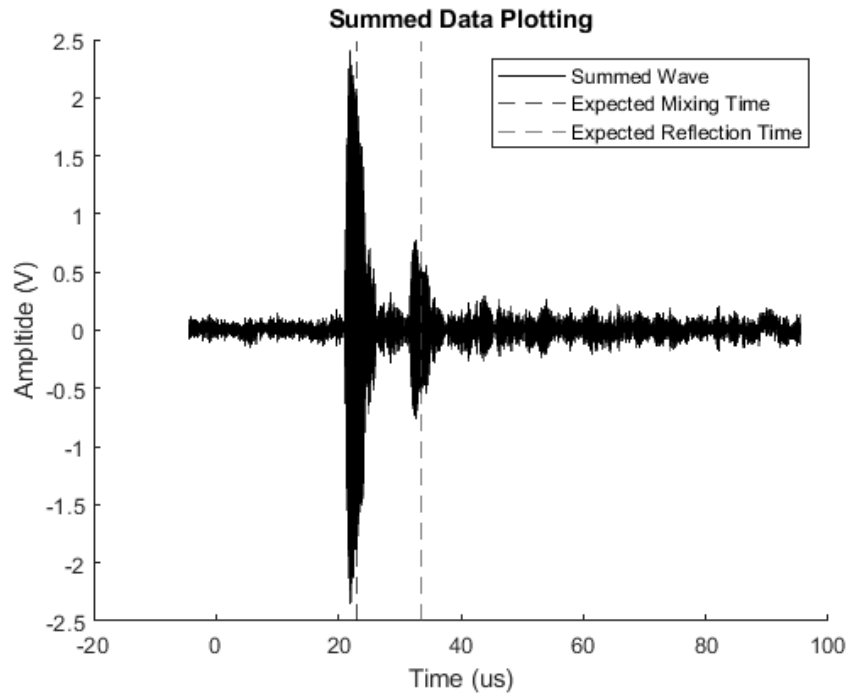


Figure 79: Single element mixing polarity flipping wave result across boundary in nominal specimen

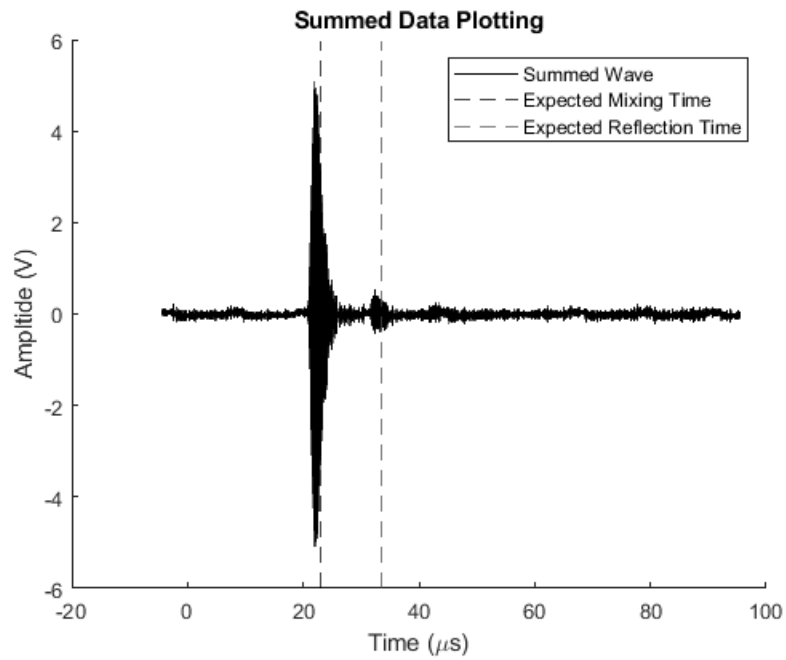


Figure 80: Single element mixing polarity flipping wave result across boundary in underpowered specimen

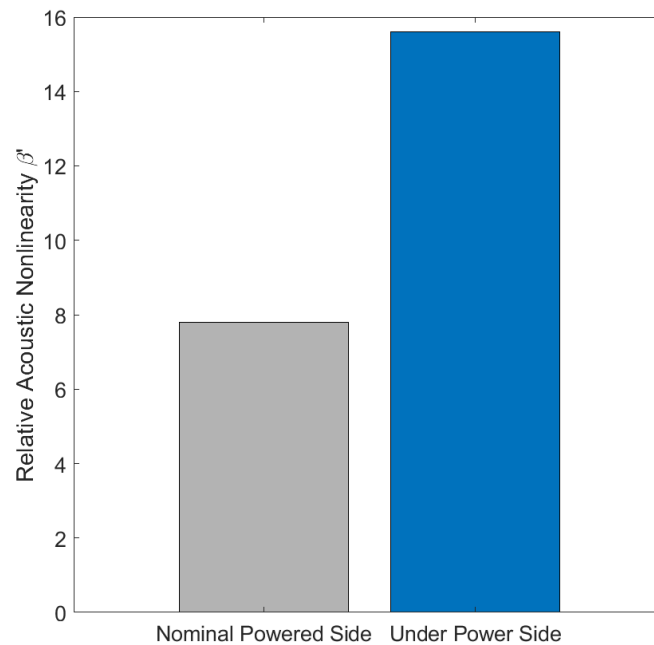


Figure 81: Comparison of  $\beta$  for single element nonlinear mixing in heterogenous AM

## 5.5 Mixing Phased Array

The results of each experimental setup using phased arrays are discussed in this section.

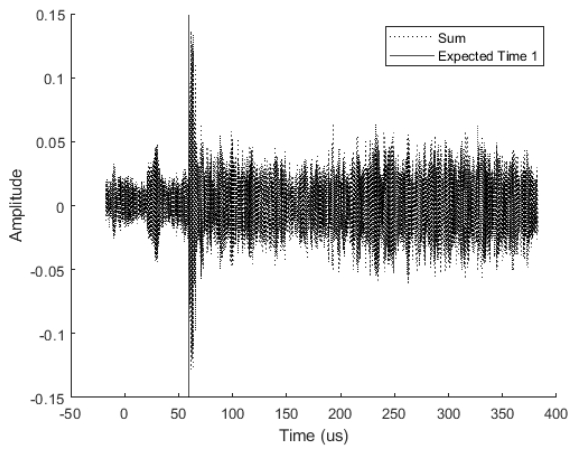
### 5.5.1 Phased Array Mixing Results in Aluminum Block

The aluminum block provided ample room for manipulation of the experimental setup until proof of mixing with phased arrays was demonstrated. As in the case of the single element mixing, the homogenous nature of the aluminum block does not lead to significant characterization. But the large size of the block helps give proof to the success of the developed technique for nonlinear wave mixing with phased arrays.

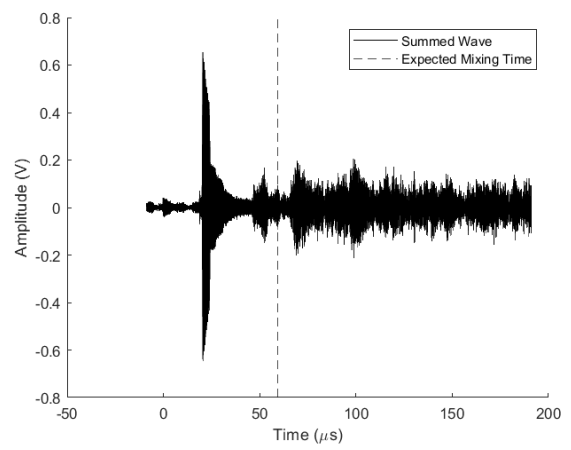
### 5.5.1.1 Proof of Scanning Verification

As discussed in Section 4.5.5.1, verification of mixing success is demonstrated in the aluminum block by measuring the wave field at multiple points under the aluminum block. In Figure 83, the measured signals from two receivers are shown when the phased arrays are delayed to mix at point 1 (left of center). In Figure 83(a), the result is from the receiving transducer in the correct location for the predicted path of the mixed wave. The result shown follows the four-way polarity flipping technique. The expected time of arrival is plotted with a vertical dotted line, which has good agreement with the peak in amplitude in the time domain signal. In Figure 83(b), the result is from the receiving transducer directly under Point 2 (center of wedges). No spike in amplitude is present at the expected time of mixing showing that the predicted movement of the mixing volume is occurring. The amplitude at the beginning of this signal is nonphysical and does not correlate to any potential acoustic wave path of the resonant wave.

Similarly, in Figure 83 the measured signals for the two receivers are shown when the incident waves are set to mix at point 2 (center). Figure 83(a) shows the four-way polarity flipping result from the left receiver at the “wrong” location for this mixing point with no peak from a mixed wave. Figure 83(b) shows an isolated peak corresponding to the estimated time of arrival of the mixed wave.

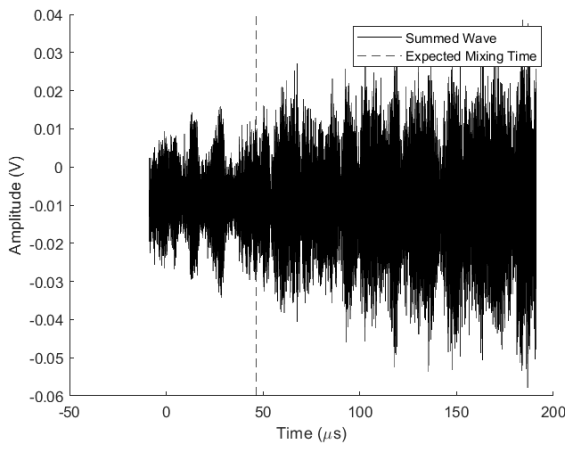


(a)

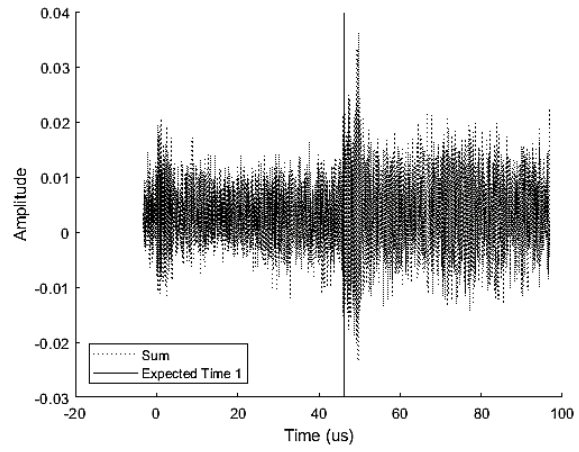


(b)

Figure 82: Phased array results in aluminum when mixing at Point 1 (a) measured at Point 1 (b) measured at Point 2



(a)



(b)

Figure 83: Phased array results in aluminum when mixing at Point 2 (a) measured at Point 1 (b) measured at Point 2

### 5.5.2 *Phased Array Mixing Results in Homogenous AM Material*

Mixing with phased arrays in the homogenous AM material was focused on ensuring an accurate experimental setup for eventual scanning of the heterogeneous specimen. As discussed in Section 4.5.6, the assessment of the mixing setup was performed by gradually moving the mixing point away from the center of the scanning arc. At points further away from the center, errors in the mixing setup are more influential. At points higher on the arc the steering angle of the two arrays are significantly different. As with the aluminum block, timing delays must be added to ensure that the two incident waves simultaneously reach the mixing point.

The received signal for mixing at the center of the scanning arc in the nominally powered AM specimen is shown in Figure 84. The effectiveness of the four-way polarity flipping technique is seen again as the received signal in Figure 84(a) shows a noisy signal result from a lone positive-positive mixed wave. Figure 84(b) shows the reduction in the unwanted second harmonics and an isolation of the mixed wave which reaches the receiver at the estimated time.

The received signal when the phased arrays are steered to 40% of the mixing arc are shown in Figure 85. Again, the mixed wave is evident following the four-way polarity flipping routine. Achievement of this measurement required successive iterations of the mixing setup and repeated assessment of material values from Section 5.2. The high sensitivity of the mixing setup with phased arrays to the values of acoustic speed is combated in the acquisition of these measurements. Small errors in alignment and timing can lead to no generation of a scattered wave. Difficulty in the experimental acquisition of these setups must be acknowledged in the discussion on the implementation of a phased

array based nonlinear wave mixing setup. This discussion is in the conclusion of this work (Section 6.3).

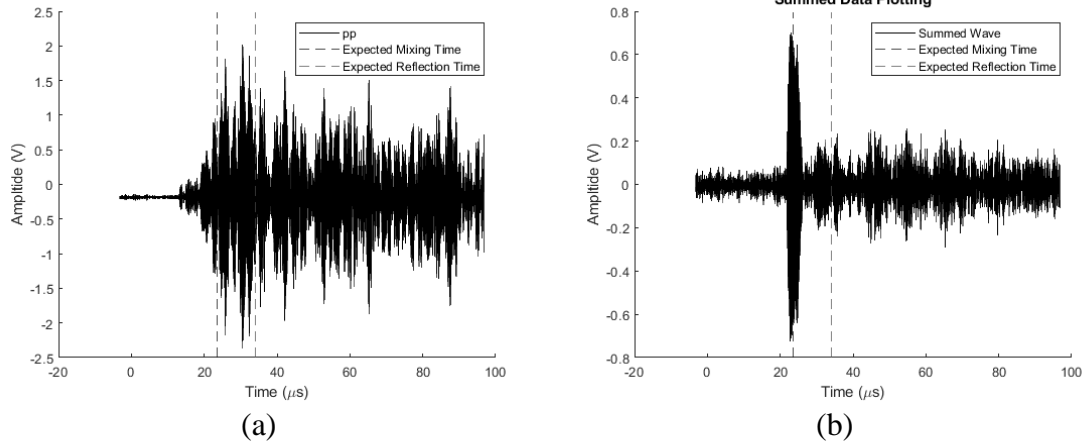


Figure 84: 50% of scanning arc in AM 1 with phased arrays

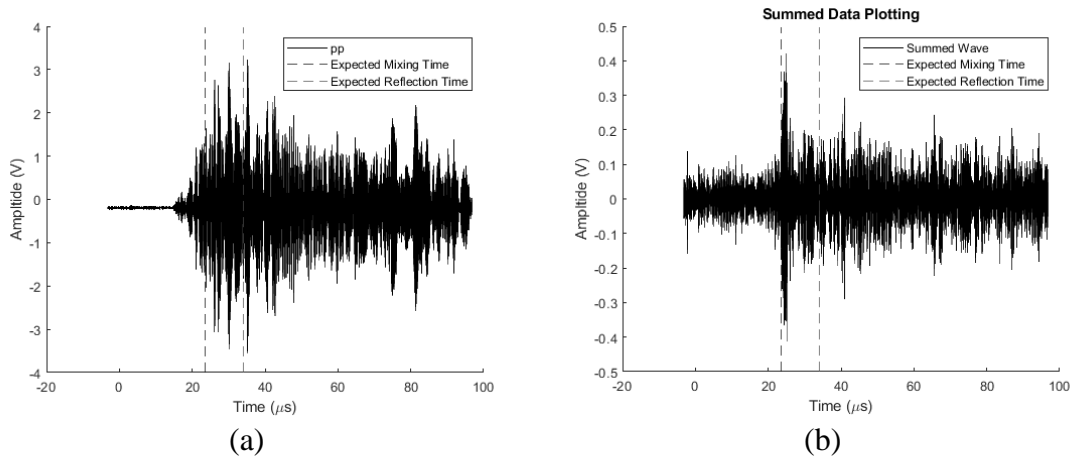


Figure 85: 40% of scanning arc in AM 1 with phased arrays

### 5.5.3 Phased Array Mixing Results in Heterogeneous AM Material

The results from the phased array based nonlinear wave mixing results in the heterogeneous AM specimens are shown and discussed in this section. First the results for the combined AM specimen are shown followed by the stacked AM specimen.

### 5.5.3.1 Across Acoustically Transparent Boundary

Scanning across the acoustically transparent boundary shows the first result of a nonlinear wave mixing setup that is sensitive to microstructural changes in a material that is scanned with phased arrays. Figure 86 shows the measured response when mixing at 55% of the scanning arc in the combined AM specimen as defined in Figure 54. The measurement point defined at 55% of the scanning arc is located on the underpowered side of the boundary.

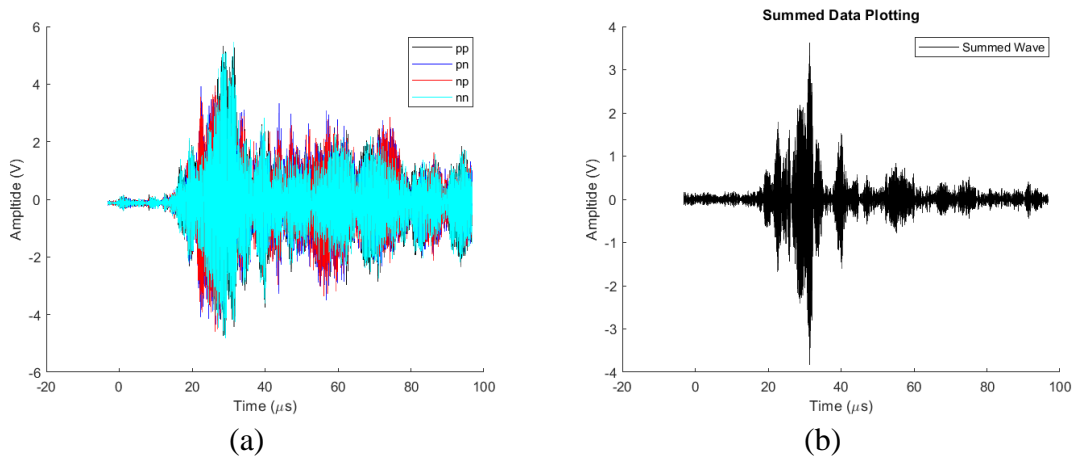


Figure 86: Measured Signal of 55% of scanning arc for combined AM specimen

The amplitude of  $\beta$  is quantified for repeated measurements made at mixing points defined at 55% of the scanning arc and 45% of the scanning arc, which is located within the nominally powered AM. The diffraction correction for the incident waves accounts for the differing attenuation and emitting angle for the incident waves. The diffraction for each incident wave is calculated from the material it propagates within the most. The diffraction for the mixed wave depends on which side of the acoustically transparent boundary the mixing occurs.

A comparison of the quantified values of relative nonlinearity is shown Figure 87. The measured value of acoustic nonlinearity is found to be 5.4 at 45% on the nominally powered side and 9.3 at 55% in the underpowered side. The percent difference between these two values is 53%. While a similar sensitivity is shown between characterization with single elements and phased arrays, comparison between the two experimental setups is difficult due to simplifications in the diffraction correction. The single element and phased arrays are simplified to a piston source differently. By following the same trend previously measured with single elements, the results for phased arrays in the combined specimen show the sensitivity of the developed technique to microstructural features in a heterogeneous sample. This is the first known result showing the potential for the use of phased arrays for the nonlinear wave mixing to characterize a material microstructure.

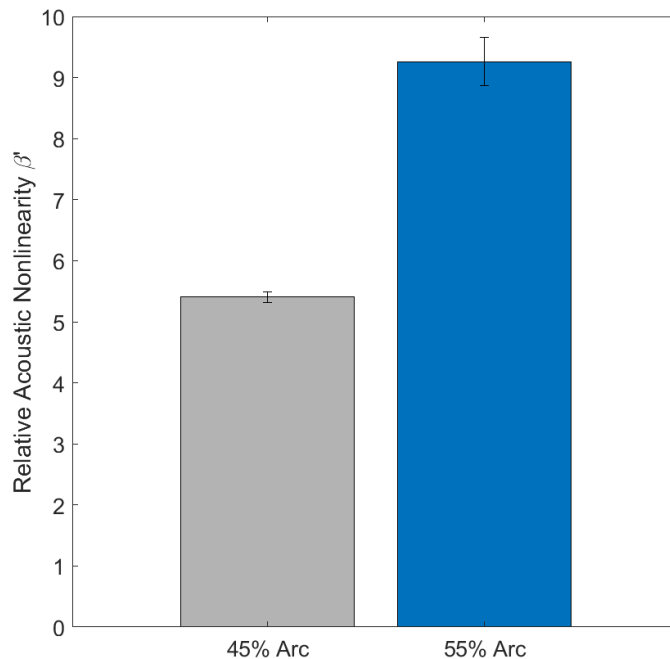


Figure 87: Comparison of relative acoustic nonlinearity measured with phased arrays on combined AM specimen after diffraction correction

When the small difference in speed of sound between the halves of the combined AM specimen is ignored, a single scanning arc is generated across the acoustically transparent boundary. A result measured following a setup with this error is shown in Figure 88 for discussion purposes. No noticeable amplitude corresponding to the resonant wave is seen Figure 88(b) even after the implementation of the four-way polarity flipping technique. A significant amplitude of a 10MHz wave field exists but does not correlate to a mixed wave. By not accounting for the small variations in speed of sound within the specimen, no or inefficient nonlinear wave mixing occurs. This exemplifies the sensitivity of the phased array based mixing technique to wave speed. Concern on the sensitivity of this technique is discussed in the conclusion.

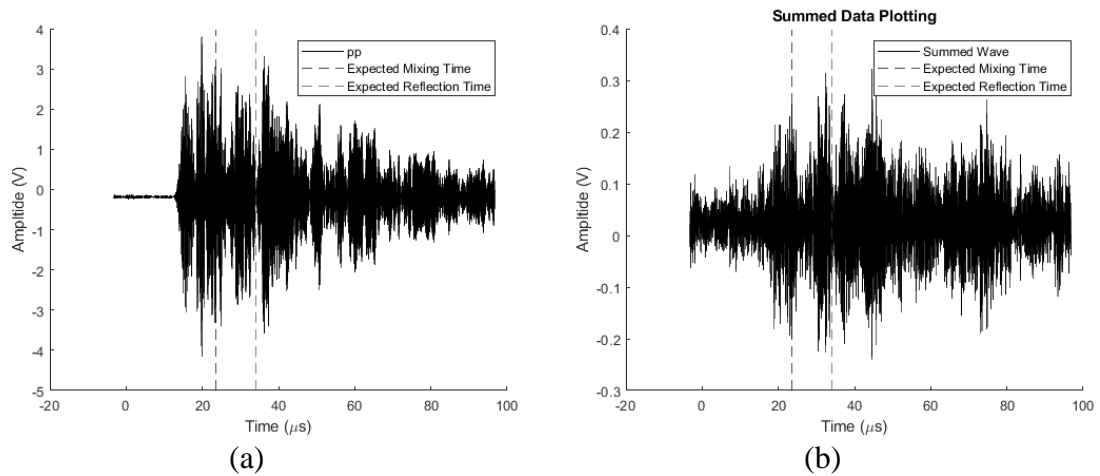


Figure 88: 45% of scanning arc in combined specimen across acoustic boundary when speed of sound differences are not considered

### 5.5.3.2 In Stack Material

The results for the nonlinear wave mixing with phased arrays in the stacked AM specimen is shown in Figure 89. The first peak in amplitude in the four-way polarity flipping signal aligns with the expected time of arrival of the mixed wave. Peaks in amplitude after this time are attributed to reflections within the layers of the specimen. This result shows the success of nonlinear mixing in another heterogeneous AM specimen. It shows the success of nonlinear mixing for an AM specimen with a more accurate representation of the boundary condition between regions with varying microstructural properties. However, due to the geometric constraints of the specimen, comparison between all three layers with the same phased array setup is not possible.

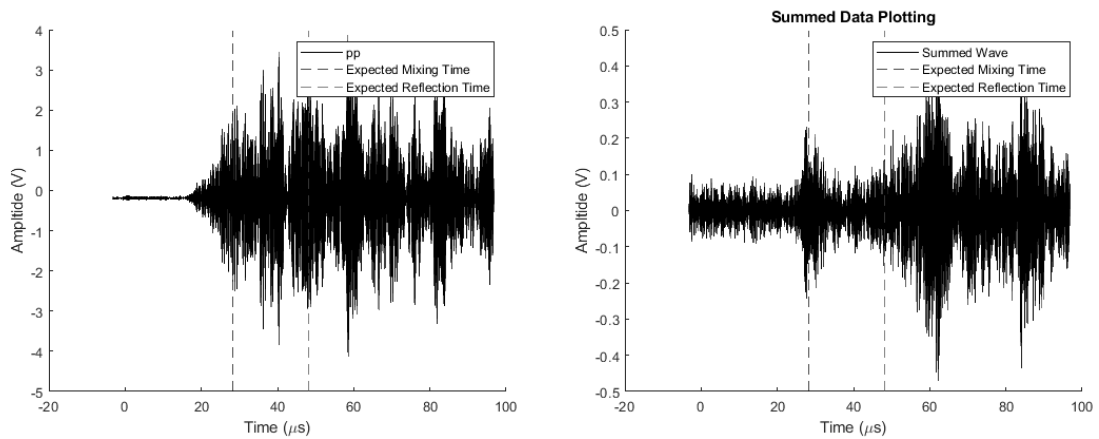


Figure 89: Measure of middle layer in stack AM specimen

## 5.6 Bulk Nonlinearity from Second Harmonic Generation

A relative measure of acoustic nonlinearity  $\beta_{SHG}$  is made with the through the thickness second harmonic generation NLU setup described in Section 4.6. The results of this measurement are shown in Figure 90. Following the trends in nonlinear mixing, the

relative measure of acoustic nonlinearity in the underpowered specimen is higher than that in the nominally powered specimen. Again, the increase in lack-of-fusion porosity in the underpowered specimen is thought to contribute to the generation of higher harmonics which is characterized with  $\beta_{SHG}$ . Note that the irregular shape of the porosity can be an efficient source of nonlinearity. Comparisons in the values of nonlinearity in these results should not be made with those presented from nonlinear wave mixing. In both measurement types, the presented value is a relative measure of nonlinearity. Furthermore, the absolute values for each nonlinearity would also not be equal. The third order elastic constants contributing to each generation of nonlinearity are different:  $m$  for  $\beta$  of shear-shear wave mixing and  $l$  and  $m$  for  $\beta_{SHG}$  of longitudinal second harmonic generation, while the porosity defect will contribute to increases of these third order elastic constants. The results from the through NLU measurement verify the increase in acoustic nonlinearity seen with nonlinear wave mixing.

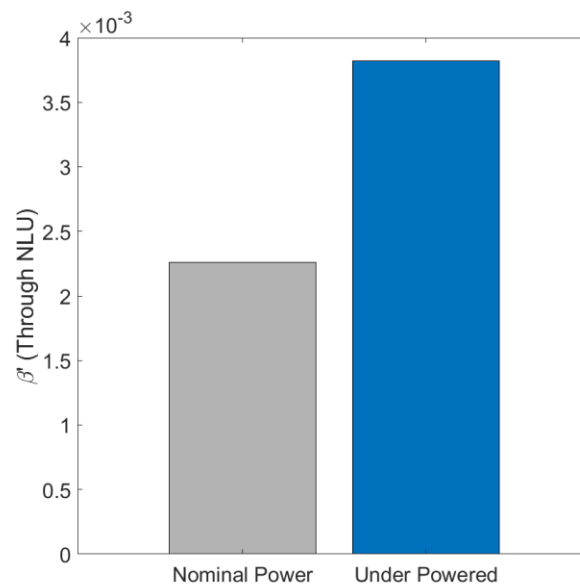


Figure 90: Comparison of relative  $\beta$  in AM specimens

## CHAPTER 6. CONCLUSION AND FUTURE WORK

### 6.1 Summary of Results

This research details the theorization and development of a novel phased array based measurement technique for nonlinear shear-shear wave mixing. This measurement technique can uniquely provide localized values of the acoustic nonlinearity parameter which is scanned from multiple points in a material of interest.

Phased arrays are used in this work to generate the incident waves. In doing so, the material state of multiple localized volumes can be interrogated from the same experimental setup and thus without altering the contact condition. The development of this technique is shown in a series of experimental setups taken before arriving at a successful phased array based nonlinear wave mixing measurement method.

This novel method was developed and verified using three classes of materials. A homogenous aluminum block is used as a substitute test material to serve as a large backdrop for material testing in metals. A concrete structure with imbedded ASR and fire damage is studied in parallel development showing the range of this technique and the distinct advantages it provides to heterogeneous materials. The central material in this work is a set of additively manufactured 316L stainless steels, in which one specimen has been intentionally made to increase lack-of-fusion porosity. Verification of the increase in porosity is made with X-ray computed tomography.

An accurate measure of acoustic velocity is made for each material and the sensitivity of the phased array based nonlinear wave mixing method is shown. Small errors in linear acoustic properties are significant in a phased array based nonlinear wave mixing

technique. Both the necessary resonance conditions and the generation of the correct incident waves with phased arrays are dependent on speed of sound. Implementation of a phased array based nonlinear wave mixing system in practical applications would require a preceding analysis to determine material properties. Another solution can be in the form of iterative nonlinear wave mixing measurements that are performed through a range of wave velocities. The set of material parameters that result in an identifiable mixed wave would then be used for the scanning of the material of interest.

Nonlinear wave mixing with single elements is shown to successfully map embedded damage in the concrete structure. At a cross section through each damage state, the resulting  $\beta$  from nonlinear wave mixing significantly increases at measurements made containing the damaged material. Single element mixing measurements are also compared between the nominally powered and low powered AM specimen. An increase in  $\beta$  is shown in the low powered AM specimen correlating to an increase in lack-of-fusion porosity. Nonlinear wave mixing results are shown to be more sensitive to the change in AM microstructure than comparative linear ultrasound measures.

Confirmation that the measured nonlinear response is uniquely caused by resonant interaction verifies successful nonlinear wave mixing with phased arrays. The effectiveness of nonlinear wave mixing resulting from beam steering is shown by gradually moving the mixing point through a defined scanning path. A successful demonstration of nonlinear wave mixing with phased arrays is made by characterizing a combined specimen with regions of varying porosity density. By scanning across a heterogeneous specimen, the scanning capabilities of the nonlinear mixing setup are shown, and the results follow the trends found from comparative measures.

## 6.2 Recommendations for Future Work

Refinements to the presented measurement method can be made for the expanded application of this method to new materials and geometries. A 316L PBF stainless steel specimen with embedded regions printed at varying power levels is presented in the Appendix A.4 Additional Additively Manufactured Specimen. The embedded regions are made to contain different porosity densities. Measurement of this specimen or others with small regions of damage could be used to show the granularity that is possible with a phased array based nonlinear wave mixing technique. Measurements of this form could better demonstrate the sensitivity of  $\beta$  to only the material within the mixing volumes along a scanning path and not the length of the incident waves.

No known commercial phased array systems are available for the generation of low frequency (<100 kHz) incident waves. Development of a functional low frequency array system would be required for a phased array based nonlinear wave mixing setup in concrete. Preliminary work on the creation of a functional low frequency phased array system has begun at Georgia Tech.

All specimens studied in this work are rectangular prisms; this geometry provides parallel surfaces for generally orthogonal measurement of the scattered wave. However, field application of this measurement technique would likely include more complex geometries. Variations of the mixing setup can be developed to better conform to non-rectangular geometries. The resonance cases beyond shear-shear mixing can be more beneficial in such geometries.

An additional study can be done to determine correlation between the measured  $\beta$  and material microstructures. This study would benefit multiple nonlinear ultrasound based

NDE techniques. A complete understanding of all influences on  $\beta$  can potentially lead to selectivity in microstructural damage assessment.

### **6.3 Significance and Impact**

The measurement technique developed in this work is the first known system for the characterization of material state using phased arrays for nonlinear wave mixing. In contrast to other nonlinear ultrasonic NDE techniques, a localized characterization of material state is made with nonlinear wave mixing. Other measures of acoustic nonlinearity are averaged over the propagation distance of the interrogating wave. Location specific microstructural information can better characterize materials with nonuniformly distributed microstructural damage.

With phased arrays, the material microstructure within a given scanning volume can be characterized with a single measurement setup. For large civil structures, this can significantly improve scanning speeds. In highly attenuative materials like concrete, nonlinear wave mixing can interrogate deeper into a material than comparative nonlinear NDE techniques. In additively manufactured materials, the localized values of nonlinearity can be used to assess print quality and as part of a qualification procedure.

## APPENDIX A. ULTRASONIC DERIVATIONS

### A.1 Nonlinear Wave Propagation

#### A.1.1 Derivation of Nonlinearity Parameter

Derivation from previous work follows [72]. Consider a single frequency sinusoidal longitudinal wave propagating in an isotropic material with quadratic nonlinearity [23]. Following the derivation of Hamilton and Blackstock [15], the one-dimension equation of motion is given by:

$$\rho \frac{\partial^2 \mathbf{u}}{\partial t^2} = \nabla \cdot \boldsymbol{\sigma} \quad (85)$$

where  $\rho$  is density,  $t$  is time,  $\boldsymbol{\sigma}$  is the Cauchy stress tensor, and  $(\nabla \cdot \boldsymbol{\sigma})_i = \partial \sigma_{ij} / \partial x_j$ , with summation over repeated indices implied.  $u$  is particle displacement from an initial point in Lagrangian coordinates ( $\mathbf{x}$ ) to the same point in Eulerian coordinates ( $\mathbf{x}^*$ ) and is defined as  $\mathbf{u} = \mathbf{x}^* - \mathbf{x}$ .

Equation 85 is expressed in a Eulerian, or spatial, coordinates; typically, nonlinear elasticity in solids is presented in Lagrangian, or material coordinates. The deformation gradient tensor relates the spatial and material frames:

$$\mathbf{F} = \frac{\partial \mathbf{x}^*}{\partial \mathbf{x}} \quad (86)$$

From this, the Lagrangian strain tensor is defined as:

$$\mathbf{E} = \frac{1}{2}(\mathbf{F}^T \cdot \mathbf{F} - \mathbf{I})$$

(87)

$$E_{ij} = \frac{1}{2} \left( \frac{\partial u_i}{\partial x_j} + \frac{\partial u_j}{\partial x_i} + \frac{\partial u_k}{\partial x_i} + \frac{\partial u_k}{\partial x_j} \right)$$

in both matrix and indices notations. The first Piola-Kirchoff stress tensor is introduced:

$$\mathbf{P} = \frac{\rho_o}{\rho} \boldsymbol{\sigma} \cdot \mathbf{F}^{-T}$$

(88)

where, in Lagrangian coordinates,  $\rho_o$  and  $\rho$  are the densities of the undeformed and deformed bodies, respectively. Substitution of the Piola-Kirchoff stress tensor Equation 88 into the Eulerian equation of motion (Equation 85) and use of the Euler-Piola-Jacobi identity provides the equation of motion in Lagrangian coordinates without body forces:

$$\rho_o \frac{\partial^2 \mathbf{u}}{\partial t^2} = \nabla_x \cdot \mathbf{P}$$

(89)

where  $\nabla_x$  is the gradient in the Lagrangian coordinates. The specific strain energy per mass  $W$  is a function of local deformation volume changes and is therefore a function of the Lagrangian strain tensor  $\mathbf{E}$ . The Piola-Kirchoff stress tensor can then be rewritten as:

$$\mathbf{P} = \rho_o \mathbf{F} \cdot \frac{\partial W}{\partial \mathbf{E}}$$

(90)

A Taylor expansion for small but not negligible strain leads to the following:

$$\rho_0 W = \frac{1}{2!} C_{ijkl} E_{ij} E_{kl} + \frac{1}{3!} C_{ijklmn} E_{ij} E_{kl} E_{mn} + O \quad (91)$$

where  $C_{ijkl}$  and  $C_{ijklmn}$  are the second and third order elastic moduli, respectively, and  $O$  are higher order terms that are neglected with the assumption of small strain. This allows the Piola-Kirchoff stress tensor in Equation 90 to be rewritten as:

$$P_{ij} = C_{ijkl} \frac{\partial u_k}{\partial x_l} + \frac{1}{2} M_{ijklmn} \frac{\partial u_k}{\partial x_l} \frac{\partial u_m}{\partial x_n} + \frac{1}{3} M_{ijklmn} \frac{\partial u_k}{\partial x_l} \frac{\partial u_m}{\partial x_n} \frac{\partial u_p}{\partial x_q} + \dots \quad (92)$$

With the higher order tensor being defined as:

$$M_{ijklmn} = C_{ijklmn} + C_{ijkln} \delta_{km} + C_{jnkl} \delta_{im} + C_{jlmn} \delta_{ik} \quad (93)$$

where  $\delta_{ij}$  is the Kronecker delta. Substitution of Equations 92 and 93 into Equation 89 gives the nonlinear wave equation:

$$\frac{\partial^2 u_i}{\partial t^2} = \frac{1}{\rho_0} \frac{\partial^2 u_k}{\partial x_j \partial x_l} \left( C_{ijkl} + M_{ijklmn} \frac{\partial u_m}{\partial x_n} \right) \quad (94)$$

The second and third order elastic constants of  $M_{ijklmn}$  in Equation 94 can be expressed using Voigt notation ( $C_{ijklmn} = C_{IJK}$ ), then one-dimensional wave motion in one direction is written:

$$\frac{\partial^2 u_1}{\partial t^2} = \frac{1}{\rho_0} \frac{\partial^2 u_1}{\partial x_1^2} \left( C_{11} + (C_{1111} + 3C_{11}) \frac{\partial u_1}{\partial x_1} \right) \quad (95)$$

Alternatively, the Huang coefficients ( $A_2^e = C_1 + C_{11}$ ;  $A_3^e = C_{111} + 3C_{11}$ ) are substituted into Equation 95:

$$\frac{\partial^2 u_1}{\partial t^2} = \frac{1}{\rho_0} \frac{\partial^2 u_1}{\partial x_1^2} A_2^e \left( 1 + \frac{A_3^e}{A_2^e} \frac{\partial u_1}{\partial x_1} \right) \quad (96)$$

where the ratio of Huang coefficients is defined as the acoustic nonlinearity parameter [81].

$$\beta = \frac{A_3^e}{A_2^e} = \frac{C_{111} + 3C_{11}}{C_1 + C_{11}} \quad (97)$$

Consider an excitation of a harmonic wave of amplitude  $A$  and frequency  $\omega$ :

$$u_1 = A \times \cos(kx_1 - \omega t) \quad (98)$$

where the wavenumber is defined  $k = \omega/c_L$ , with  $c_L$  being the longitudinal wave velocity of the material. With this excitation, the partial differential equation in Equation 96 can be solved through perturbation analysis as [81]:

$$\begin{aligned} u_1 &= \frac{1}{8} \beta k^2 A_1^2 x_1 + A_1 \cos(kx_1 - \omega t) + \frac{1}{8} \beta k^2 A_1^2 x_1 \cos(2kx_1 - 2\omega t) \\ &= A_0 + A_1 \cos(kx_1 - \omega t) - A_2 \cos(2kx_1 - 2\omega t) \end{aligned} \quad (99)$$

The third term in Equation 99 is information on the second harmonic wave and can be used to show the following relationship for the acoustic nonlinearity parameter:

$$\beta = \frac{8A_2}{k^2 x_1 A_1^2} \quad (100)$$

This expression shows that  $\beta$  can be measured from amplitudes of the fundamental ( $A_1$ ) and second harmonic ( $A_2$ ) signals, with information on the propagation distance ( $x_1$ ) and the wave number.  $\beta$  is an absolute material constant that can give information to the state of material damage as shown in Equation 97.

### A.3 Acoustic Attenuation

#### A.3.1 Derivation of Acoustic Attenuation

Derivation from previous work follows [72]. Acoustic attenuation is a property encompassing two different effects in a material. As a wave passes through a material, energy can be lost through absorption and scattering [71]:

$$\alpha(f) = \alpha_a(f) + \alpha_s(f) \quad (101)$$

where  $\alpha_a(f)$  is the absorption contribution to attenuation caused by features including dislocation damping and thermoelastic interactions, and  $\alpha_s(f)$  is the scattering contribution from interactions with features including voids and grain boundaries.  $f$  is the frequency for which attenuation is dependent upon [71]. For most media including stainless steels, wave amplitude decreases with propagation due to attenuation. This effect is accounted for in the 1D wave particle displacement equation with the form:

$$u = Ae^{(-\alpha Z)} e^{i(\omega t - kZ)} \quad (102)$$

To determine the attenuation coefficient of a material, first the wave speed in the material needs to be measured. The wave speed is measured for each specimen and by measuring the time difference between the initial wave packet and the first reflection:

$$c = \frac{2z}{t_1 - t_2} \quad (103)$$

where  $z$  is the sample thickness and  $t_1$  and  $t_2$  are the temporal locations of the same point on two contiguous packets. The magnitude for complex frequency spectra of each packet can be found from [82]:

$$s_n(f) = \frac{\lambda \times \Delta x}{(r_{trans})^2} \quad (104)$$

where  $\lambda$  is the wavelength of the signal found using the wave speed from Equation 103 and the inputted frequency.  $\Delta x$  is total distance travelled by the corresponding wave packet, and  $r_{trans}$  is the radius of the transducer. Equation 104 is used to calculate magnitudes of the complex diffraction correction functions corresponding to the propagation distances of these signals,  $D$ , as described by Rogers and Van Buren [74]:

$$D(s_n) = 1 - 2^{-i(2\pi/s_n)} \left[ J_0 \left( \frac{2\pi}{s_n} \right) + iJ_1 \left( \frac{2\pi}{s_n} \right) \right] \quad (105)$$

where  $J_n$  is a Bessel function of the first kind of order  $n$ . Equation 105 and the voltage ratio between wave packets can be used to calculate the attenuation coefficient:

$$\alpha(f) = \frac{1}{2z} \left[ \ln \left( \left| \frac{v_1}{v_2} \right| \right) - \ln \left( \left| \frac{D(s_1)}{D(s_2)} \right| \right) \right] \quad (106)$$

Where  $v_1/v_2$  is the measured voltage ratio between the steady state portions of the first and second wave packets. This attenuation measurement does not correct for losses between the transducer and material surface; however, with a consistent experimental setup, the largest contribution to the variation between each specimen's attenuation will come from the material itself. Thus, these values are used as a relative attenuation measurement to compare between the specimens in this work.

#### A.4 Printing Parameters of Additively Manufactured 316L PBF Specimens

Table 7: Printing Parameters of AM Specimens

Material Classification	Nominal Power	Low Power	High Power
Hatch Rotation Angle (°)	47	47	47
Hatch Restriction Angle (°)	30	30	30
Hatch Infill Skipping (Layers)	0	0	0
Hatch Offset (mm)	0.003	0.003	0.003
Hatch Overlap with Infill (mm)	0.17	0.17	0.17
Hatch Minimum Vector Length (mm)	0.1	0.1	0.1
Downskin Exposure Pattern	Stripes	Stripes	Stripes
Downskin Hatch Features	Skywriting	Skywriting	Skywriting
Downskin Pattern	Shifted	Shifted	Shifted
Downskin Exposure Mode	Single	Single	Single
Downskin Ridge (mm)	-1	-1	-1
Downskin Laser Speed (m/s)	0.0743	0.0743	0.0743
Downskin Hatch Distance (mm)	0.09	0.09	0.09
Upskin Exposure Pattern	Stripes	Stripes	Stripes
Upskin Hatch Features	Skywriting	Skywriting	Skywriting
Upskin Pattern	Shifted	Shifted	Shifted
Upskin Exposure Mode	Single	Single	Single
Upskin Ridge (mm)	-1	-1	-1
Upskin Stripe Width (mm)	1000	1000	1000
Upskin Overlap Stripes (mm)	0	0	0
Upskin Laser Speed (m/s)	0.5149	0.5149	0.5149

<b>Upskin Hatch Distance (mm)</b>	0.1	0.1	0.1
<b>Infill Exposure Pattern</b>	Stripes	Stripes	Stripes
<b>Infill Hatch Features</b>	Skywriting	Skywriting	Skywriting
<b>Infill Pattern</b>	Shifted	Shifted	Shifted
<b>Infill Exposure Mode</b>	Single	Single	Single
<b>Infill Stripe Width (mm)</b>	12	12	12
<b>Infill Overlap Stripes (mm)</b>	0.09	0.09	0.09
<b>Infill Laser Power (W)</b>	214.2	160	270
<b>Infill Laser Speed (m/s)</b>	0.9281	0.9281	0.9281
<b>Infill Hatch Distance (mm)</b>	0.1	0.1	0.1
<b>Contour Offset (mm)</b>	0	0	0
<b>Contour Thickness (Number of Layers)</b>	1	1	1
<b>Contour Corridor (mm)</b>	0.07	0.07	0.07
<b>Std. Contour Laser Power (W)</b>	136.1	136.1	136.1
<b>Std. Contour Laser Speed (m/s)</b>	0.4469	0.4469	0.4469
<b>Down Contour Laser Power (W)</b>	0	0	0
<b>Down Contour Laser Speed (m/s)</b>	4	4	4
<b>OnPart Contour Laser Power (W)</b>	127.9	127.9	127.9
<b>OnPart Contour Laser Speed (m/s)</b>	0.4471	0.4471	0.4471
<b>Edge Offset (mm)</b>	0	0	0
<b>Edge Factor</b>	2	2	2
<b>Edge Threshold</b>	3	3	3
<b>Edge Min. Radius Factor</b>	0	0	0
<b>Edge Laser Power (W)</b>	100	100	100
<b>Edge Laser Speed (m/s)</b>	0.9	0.9	0.9

#### **A.4 Additional Additively Manufactured Specimen**

An additional 316L PBF specimen was manufactured in this work. This part was made in a separate build from the other 316L PBF specimens shown in this work. The small cubes analyzed for the effects of the printing parameters on porosity were made simultaneously to this specimen. The printing parameters largely follow the printing parameters shared in Table 7 which were used on the other AM specimens in this work. Differences to this set of printing parameters are from the variation in laser power used to build each portion of the additional AM specimen.

A diagram of the specimen can be seen in Figure 91. The majority of this specimen is built at 214.2 W which is the nominal laser power for the print speed used in Table 7. The material printed at this laser power is considered the reference state. Small regions are embedded within this specimen that are printed at a range of laser power settings. Regions printed at 160 W and 187 W are intended to correlate with an increase in lack-of-fusion porosity. Printing at 242 W and 270 W are intended to cause an increase in keyhole porosity. The embedded regions are located along an intersect plane that can be easily scanned using the experimental setup discussed in Section 4.4.4. A crosscut of the specimen is shown in Figure 92, the size and location of the embedded regions can be seen. A successful scan of this specimen with a phased array based nonlinear wave mixing technique has not been performed at the time of this thesis.

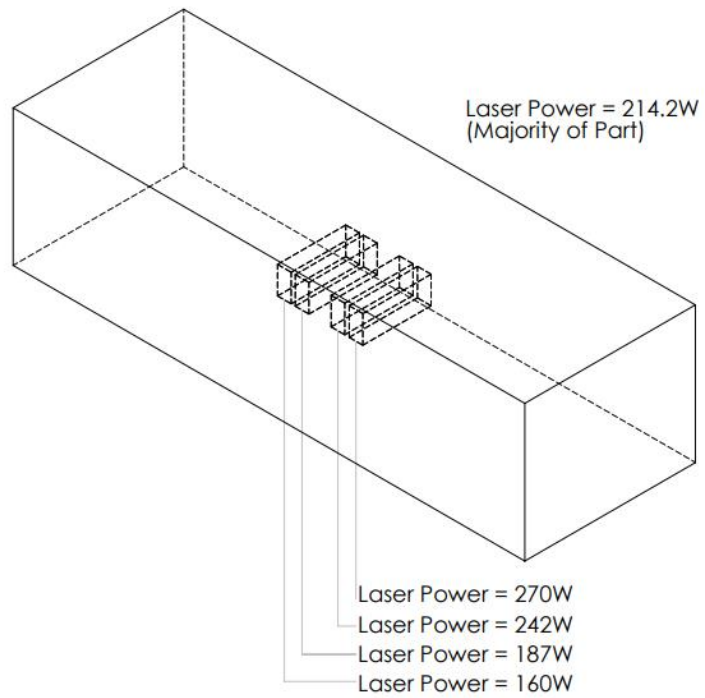


Figure 91: Additional 316L PBF specimen



Figure 92: Cross cut of additional 316L PBF specimen

## REFERENCES

- [1] A. Bellotti *et al.*, “Nonlinear ultrasonic technique for the characterization of microstructure in additive materials,” *J. Acoust. Soc. Am.*, vol. 149, no. 1, pp. 158–166, Jan. 2021, doi: 10.1121/10.0002960.
- [2] L. Yang *et al.*, *Additive Manufacturing of Metals: The Technology, Materials, Design and Production*. Springer International Publishing, 2017. doi: 10.1007/978-3-319-55128-9.
- [3] J. M. Waller, R. L. Saulsberry, B. H. Parker, K. L. Hodges, E. R. Burke, and K. M. Taminger, “Summary of NDE of additive manufacturing efforts in NASA,” presented at the 41ST ANNUAL REVIEW OF PROGRESS IN QUANTITATIVE NONDESTRUCTIVE EVALUATION: Volume 34, Boise, Idaho, 2015, pp. 51–62. doi: 10.1063/1.4914594.
- [4] M. Seifi, A. Salem, J. Beuth, O. Harrysson, and J. J. Lewandowski, “Overview of Materials Qualification Needs for Metal Additive Manufacturing,” *JOM*, vol. 68, no. 3, pp. 747–764, Mar. 2016, doi: 10.1007/s11837-015-1810-0.
- [5] A. M. Beese, “Chapter 5 - Microstructure and Mechanical Properties of AM Builds,” in *Thermo-Mechanical Modeling of Additive Manufacturing*, M. Gouge and P. Michaleris, Eds. Butterworth-Heinemann, 2018, pp. 81–92. doi: 10.1016/B978-0-12-811820-7.00007-0.

- [6] M. Gouge and P. Michaleris, “Chapter 1 - An Introduction to Additive Manufacturing Processes and Their Modeling Challenges,” in *Thermo-Mechanical Modeling of Additive Manufacturing*, M. Gouge and P. Michaleris, Eds. Butterworth-Heinemann, 2018, pp. 3–18. doi: 10.1016/B978-0-12-811820-7.00002-1.
- [7] H. Gong, K. Rafi, H. Gu, T. Starr, and B. Stucker, “Analysis of defect generation in Ti–6Al–4V parts made using powder bed fusion additive manufacturing processes,” *Addit. Manuf.*, vol. 1–4, pp. 87–98, Oct. 2014, doi: 10.1016/j.addma.2014.08.002.
- [8] R. Cunningham, S. P. Narra, C. Montgomery, J. Beuth, and A. D. Rollett, “Synchrotron-Based X-ray Microtomography Characterization of the Effect of Processing Variables on Porosity Formation in Laser Power-Bed Additive Manufacturing of Ti-6Al-4V,” *JOM*, vol. 69, no. 3, pp. 479–484, Mar. 2017, doi: 10.1007/s11837-016-2234-1.
- [9] R. Cunningham, S. P. Narra, T. Ozturk, J. Beuth, and A. D. Rollett, “Evaluating the Effect of Processing Parameters on Porosity in Electron Beam Melted Ti-6Al-4V via Synchrotron X-ray Microtomography,” *JOM*, vol. 68, no. 3, pp. 765–771, Mar. 2016, doi: 10.1007/s11837-015-1802-0.
- [10] W. E. King *et al.*, “Observation of keyhole-mode laser melting in laser powder-bed fusion additive manufacturing,” *J. Mater. Process. Technol.*, vol. 214, no. 12, pp. 2915–2925, Dec. 2014, doi: 10.1016/j.jmatprotec.2014.06.005.
- [11] K. H. Matlack, J. J. Wall, J.-Y. Kim, J. Qu, L. J. Jacobs, and H.-W. Viehrig, “Evaluation of radiation damage using nonlinear ultrasound,” *J. Appl. Phys.*, vol. 111, no. 5, p. 054911, Mar. 2012, doi: 10.1063/1.3692086.

- [12] A. Ruiz, N. Ortiz, A. Medina, J.-Y. Kim, and L. J. Jacobs, “Application of ultrasonic methods for early detection of thermal damage in 2205 duplex stainless steel,” *NDT Amp E Int.*, vol. 54, pp. 19–26.
- [13] Lawrence Kinsler, A. Frey, A. Coppins, and J. Sanders, *Fundamentals of Acoustics*, 3rd ed. John Wiley & Sons, Ltd, 1982.
- [14] B. A. Auld, *Acoustic fields and waves in solids*. Рипол Классик, 1973.
- [15] M. F. Hamilton and D. T. Blackstock, *Nonlinear Acoustics*. Academic Press, 1998.
- [16] F. D. Murnaghan, “Finite Deformations of an Elastic Solid,” *Am. J. Math.*, vol. 59, no. 2, pp. 235–260, 1937, doi: 10.2307/2371405.
- [17] M. P. May, “Proposal and analysis of a non-collinear wave mixing technique for the detection of micro-cracks using phased arrays,” Aug. 2020, Accessed: Mar. 10, 2023. [Online]. Available: <https://smartech.gatech.edu/handle/1853/64085>
- [18] S. Takahashi and R. Motegi, “Measurement of third-order elastic constants and applications to loaded structural materials,” *SpringerPlus*, vol. 4, p. 325, Jul. 2015, doi: 10.1186/s40064-015-1019-2.
- [19] K. H. Matlack, J.-Y. Kim, L. J. Jacobs, and J. Qu, “Review of Second Harmonic Generation Measurement Techniques for Material State Determination in Metals,” *J. Nondestruct. Eval.*, vol. 34, no. 1, p. 273, Nov. 2014, doi: 10.1007/s10921-014-0273-5.

- [20] J.-Y. Kim, L. J. Jacobs, J. Qu, and J. W. Littles, “Experimental characterization of fatigue damage in a nickel-base superalloy using nonlinear ultrasonic waves,” *J. Acoust. Soc. Am.*, vol. 120, no. 3, pp. 1266–1273, Sep. 2006, doi: 10.1121/1.2221557.
- [21] J. H. Cantrell and X.-G. Zhang, “Nonlinear acoustic response from precipitate-matrix misfit in a dislocation network,” *J. Appl. Phys.*, vol. 84, no. 10, pp. 5469–5472, Nov. 1998, doi: 10.1063/1.368309.
- [22] T. R. Smith, J. D. Sugar, J. M. Schoenung, and C. San Marchi, “Anomalous Annealing Response of Directed Energy Deposited Type 304L Austenitic Stainless Steel,” *JOM*, vol. 70, no. 3, pp. 358–363, Mar. 2018, doi: 10.1007/s11837-017-2711-1.
- [23] Akira Hikata, Bruce B. Chick, and Charles Elbaum, “Dislocation Contribution to the Second Harmonic Generation of Ultrasonic Waves,” *J. Appl. Phys.*, vol. 36, no. 1, pp. 229–236, 1965, doi: 10.1063/1.1713881.
- [24] S.-H. Park, S. Choi, D.-G. Song, and K.-Y. Jhang, “Microstructural Characterization of Additively Manufactured Metal Components Using Linear and Nonlinear Ultrasonic Techniques,” *Materials*, vol. 15, no. 11, Art. no. 11, Jan. 2022, doi: 10.3390/ma15113876.
- [25] S. Park *et al.*, “Nonlinear Acoustic Technique for Monitoring Porosity in Additively Manufactured Parts,” *J. Nondestruct. Eval. Diagn. Progn. Eng. Syst.*, vol. 5, no. 2, Jan. 2022, doi: 10.1115/1.4053252.

- [26] J. A. Slotwinski, E. J. Garboczi, and K. M. Hebenstreit, “Porosity Measurements and Analysis for Metal Additive Manufacturing Process Control,” *J. Res. Natl. Inst. Stand. Technol.*, vol. 119, pp. 494–528, Sep. 2014, doi: 10.6028/jres.119.019.
- [27] Z. Prevorovsky, J. Krofta, and J. Kober, “NDT in Additive Manufacturing of Metals,” p. 10.
- [28] G. L. Jones and D. R. Kobett, “Interaction of Elastic Waves in an Isotropic Solid,” *J. Acoust. Soc. Am.*, vol. 35, no. 1, pp. 5–10, Jan. 1963, doi: 10.1121/1.1918405.
- [29] L. H. Taylor and F. R. Rollins, “Ultrasonic Study of Three-Phonon Interactions. I. Theory,” *Phys. Rev.*, vol. 136, no. 3A, pp. A591–A596, Nov. 1964, doi: 10.1103/PhysRev.136.A591.
- [30] V. A. Korneev and A. Demčenko, “Possible second-order nonlinear interactions of plane waves in an elastic solid,” *J. Acoust. Soc. Am.*, vol. 135, no. 2, pp. 591–598, Feb. 2014, doi: 10.1121/1.4861241.
- [31] X. Gao and J. Qu, “Necessary and sufficient conditions for resonant mixing of plane waves in elastic solids with quadratic nonlinearity,” *J. Acoust. Soc. Am.*, vol. 148, no. 4, pp. 1934–1946, Oct. 2020, doi: 10.1121/10.0002009.
- [32] F. R. Rollins, “Interaction of ultrasonic waves in solid media,” *Appl. Phys. Lett.*, vol. 2, no. 8, pp. 147–148, Apr. 1963, doi: 10.1063/1.1753818.

- [33] A. J. Croxford, P. D. Wilcox, B. W. Drinkwater, and P. B. Nagy, “The use of non-collinear mixing for nonlinear ultrasonic detection of plasticity and fatigue,” *J. Acoust. Soc. Am.*, vol. 126, no. 5, pp. EL117–EL122, Nov. 2009, doi: 10.1121/1.3231451.
- [34] Z. Zhang, P. B. Nagy, and W. Hassan, “On the feasibility of nonlinear assessment of fatigue damage in hardened IN718 specimens based on non-collinear shear wave mixing,” *AIP Conf. Proc.*, vol. 1706, no. 1, p. 060003, Feb. 2016, doi: 10.1063/1.4940509.
- [35] M. Sun, Y. Xiang, M. Deng, J. Xu, and F.-Z. Xuan, “Scanning non-collinear wave mixing for nonlinear ultrasonic detection and localization of plasticity,” *NDT E Int.*, vol. 93, pp. 1–6, Jan. 2018, doi: 10.1016/j.ndteint.2017.09.010.
- [36] A. Demčenko, R. Akkerman, P. B. Nagy, and R. Loendersloot, “Non-collinear wave mixing for non-linear ultrasonic detection of physical ageing in PVC,” *NDT E Int.*, vol. 49, pp. 34–39, Jul. 2012, doi: 10.1016/j.ndteint.2012.03.005.
- [37] A. Demčenko, V. Koissin, and V. A. Korneev, “Noncollinear wave mixing for measurement of dynamic processes in polymers: Physical ageing in thermoplastics and epoxy cure,” *Ultrasonics*, vol. 54, no. 2, pp. 684–693, Feb. 2014, doi: 10.1016/j.ultras.2013.09.011.
- [38] A. Demčenko, L. Mainini, and V. A. Korneev, “A study of the noncollinear ultrasonic-wave-mixing technique under imperfect resonance conditions,” *Ultrasonics*, vol. 57, pp. 179–189, Mar. 2015, doi: 10.1016/j.ultras.2014.11.009.

- [39] J. Jiao, H. Lv, C. He, and B. Wu, "Fatigue crack evaluation using the non-collinear wave mixing technique," *Smart Mater. Struct.*, vol. 26, no. 6, p. 065005, May 2017, doi: 10.1088/1361-665X/aa6c43.
- [40] H. Lv, J. Zhang, J. Jiao, and A. Croxford, "Fatigue crack inspection and characterisation using non-collinear shear wave mixing," *Smart Mater. Struct.*, vol. 29, no. 5, p. 055024, Apr. 2020, doi: 10.1088/1361-665X/ab5486.
- [41] J. Alston, A. Croxford, J. Potter, and P. Blanloeuil, "Nonlinear non-collinear ultrasonic detection and characterisation of kissing bonds," *NDT E Int.*, vol. 99, pp. 105–116, Oct. 2018, doi: 10.1016/j.ndteint.2018.07.003.
- [42] J. Alston, "Detection of kissing bonds with non-collinear nonlinear ultrasound," p. 258.
- [43] K. Sapountzi, "The development of non-collinear non destructive evaluation of aircraft materials," p. 164.
- [44] E. Escobar-Ruiz *et al.*, "Non-linear Ultrasonic NDE of Titanium Diffusion Bonds," *J. Nondestruct. Eval.*, vol. 33, no. 2, pp. 187–195, Jun. 2014, doi: 10.1007/s10921-013-0217-5.
- [45] Z. Zhang, P. B. Nagy, and W. Hassan, "Analytical and numerical modeling of non-collinear shear wave mixing at an imperfect interface," *Ultrasonics*, vol. 65, pp. 165–176, Feb. 2016, doi: 10.1016/j.ultras.2015.09.021.

- [46] P. Blanloeuil, A. Meziane, and C. Bacon, “2D finite element modeling of the non-collinear mixing method for detection and characterization of closed cracks,” *NDT E Int.*, vol. 76, pp. 43–51, Dec. 2015, doi: 10.1016/j.ndteint.2015.08.001.
- [47] M. Liu, G. Tang, L. J. Jacobs, and J. Qu, “Measuring acoustic nonlinearity parameter using collinear wave mixing,” *J. Appl. Phys.*, vol. 112, no. 2, p. 024908, Jul. 2012, doi: 10.1063/1.4739746.
- [48] T. Ju, J. D. Achenbach, L. J. Jacobs, M. Guimaraes, and J. Qu, “Ultrasonic nondestructive evaluation of alkali–silica reaction damage in concrete prism samples,” *Mater. Struct.*, vol. 50, no. 1, p. 60, Feb. 2017, doi: 10.1617/s11527-016-0869-6.
- [49] Z. Chen, G. Tang, Y. Zhao, L. J. Jacobs, and J. Qu, “Mixing of collinear plane wave pulses in elastic solids with quadratic nonlinearity,” *J. Acoust. Soc. Am.*, vol. 136, no. 5, pp. 2389–2404, Nov. 2014, doi: 10.1121/1.4896567.
- [50] G. Tang, M. Liu, L. J. Jacobs, and J. Qu, “Detecting Localized Plastic Strain by a Scanning Collinear Wave Mixing Method,” *J. Nondestruct. Eval.*, vol. 33, no. 2, pp. 196–204, Jun. 2014, doi: 10.1007/s10921-014-0224-1.
- [51] M. Hasanian and C. J. Lissenden, “Second order harmonic guided wave mutual interactions in plate: Vector analysis, numerical simulation, and experimental results,” *J. Appl. Phys.*, vol. 122, no. 8, p. 084901, Aug. 2017, doi: 10.1063/1.4993924.
- [52] A. K. Metya, S. Tarafder, and K. Balasubramaniam, “Nonlinear Lamb wave mixing for assessing localized deformation during creep,” *NDT E Int.*, vol. 98, pp. 89–94, Sep. 2018, doi: 10.1016/j.ndteint.2018.04.013.

- [53] H. Cho, M. Hasanian, S. Shan, and C. J. Lissenden, “Nonlinear guided wave technique for localized damage detection in plates with surface-bonded sensors to receive Lamb waves generated by shear-horizontal wave mixing,” *NDT E Int.*, vol. 102, pp. 35–46, Mar. 2019, doi: 10.1016/j.ndteint.2018.10.011.
- [54] F. Li, Y. Zhao, P. Cao, and N. Hu, “Mixing of ultrasonic Lamb waves in thin plates with quadratic nonlinearity,” *Ultrasonics*, vol. 87, pp. 33–43, Jul. 2018, doi: 10.1016/j.ultras.2018.02.005.
- [55] M. B. Morlock, J.-Y. Kim, L. J. Jacobs, and J. Qu, “Mixing of two co-directional Rayleigh surface waves in a nonlinear elastic material,” *J. Acoust. Soc. Am.*, vol. 137, no. 1, pp. 281–292, Jan. 2015, doi: 10.1121/1.4904535.
- [56] T. Kundu, Ed., *Nonlinear Ultrasonic and Vibro-Acoustical Techniques for Nondestructive Evaluation*. Cham: Springer International Publishing, 2019. doi: 10.1007/978-3-319-94476-0.
- [57] J.-Y. Kim, A. Bellotti, P. Alapati, K. E. Kurtis, J. Qu, and L. J. Jacobs, “Use of a non-collinear wave mixing technique to image internal microscale damage in concrete,” *J. Appl. Phys.*, vol. 131, no. 14, p. 145102, Apr. 2022, doi: 10.1063/5.0086194.
- [58] S.-C. Wooh and Y. Shi, “Optimum beam steering of linear phased arrays,” *Wave Motion*, vol. 29, no. 3, pp. 245–265, Apr. 1999, doi: 10.1016/S0165-2125(98)00039-0.
- [59] Z. Xiao *et al.*, “Acoustic Field of a Linear Phased Array: A Simulation Study of Ultrasonic Circular Tube Material,” *Sensors*, vol. 19, no. 10, Art. no. 10, Jan. 2019, doi: 10.3390/s19102352.

- [60] “Standard Terminology for Additive Manufacturing Technologies,” <https://www.astm.org/f2792-12.html> (accessed Mar. 07, 2023).
- [61] M. Leary, “Chapter 11 - Powder bed fusion,” in *Design for Additive Manufacturing*, M. Leary, Ed. Elsevier, 2020, pp. 295–319. doi: 10.1016/B978-0-12-816721-2.00011-7.
- [62] Carsten Engel, “Selective Laser Melting versus Electron Beam Melting,” 03:41:23 UTC. Accessed: Mar. 07, 2023. [Online].
- [63] H. Choo *et al.*, “Effect of laser power on defect, texture, and microstructure of a laser powder bed fusion processed 316L stainless steel,” *Mater. Des.*, vol. 164, p. 107534, Feb. 2019, doi: 10.1016/j.matdes.2018.12.006.
- [64] “Analysis of defect generation in Ti–6Al–4V parts made using powder bed fusion additive manufacturing processes - ScienceDirect.” <https://www.sciencedirect.com/science/article/pii/S2214860414000074> (accessed Jun. 24, 2022).
- [65] P. Karimi, T. Raza, J. Andersson, and L.-E. Svensson, “Influence of laser exposure time and point distance on 75- $\mu$ m-thick layer of selective laser melted Alloy 718,” *Int. J. Adv. Manuf. Technol.*, vol. 94, no. 5, pp. 2199–2207, Feb. 2018, doi: 10.1007/s00170-017-1019-1.
- [66] S. I. Wright, M. M. Nowell, and D. P. Field, “A Review of Strain Analysis Using Electron Backscatter Diffraction,” *Microsc. Microanal.*, vol. 17, no. 3, pp. 316–329, Jun. 2011, doi: 10.1017/S1431927611000055.

- [67] “Mid-Size Metal 3D Printer for all kind of materials.”  
<https://www.eos.info/en/additive-manufacturing/3d-printing-metal/eos-metal-systems/eos-m-290> (accessed Jun. 24, 2022).
- [68] C. Britt, C. J. Montgomery, M. J. Brand, Z.-K. Liu, J. S. Carpenter, and A. M. Beese, “Effect of processing parameters and strut dimensions on the microstructures and hardness of stainless steel 316L lattice-emulating structures made by powder bed fusion,” *Addit. Manuf.*, vol. 40, p. 101943, Apr. 2021, doi: 10.1016/j.addma.2021.101943.
- [69] W. Sachse and Y. Pao, “On the determination of phase and group velocities of dispersive waves in solids,” *J. Appl. Phys.*, vol. 49, no. 8, pp. 4320–4327, Aug. 1978, doi: 10.1063/1.325484.
- [70] R. L. Smith, “The effect of grain size distribution on the frequency dependence of the ultrasonic attenuation in polycrystalline materials,” *Ultrasonics*, vol. 20, no. 5, pp. 211–214, Sep. 1982, doi: 10.1016/0041-624X(82)90021-X.
- [71] R. L. Smith, “Ultrasonic materials characterization,” *NDT Int.*, vol. 20, no. 1, pp. 43–48, Feb. 1987, doi: 10.1016/0308-9126(87)90371-3.
- [72] A. Bellotti, “Nonlinear Ultrasonic Technique for the Characterization of Microstructure in Additive Materials,” Master’s Thesis, Georgia Institute of Technology, Atlanta, GA, 2020.
- [73] “Lumped LC Band Pass Filter, 9.5 - 11.5 MHz, 50Ω | BBP-10.7+ | Mini-Circuits.”  
<https://www.minicircuits.com/WebStore/dashboard.html?model=BBP-10.7%2B>  
(accessed Mar. 12, 2023).

- [74] P. H. Rogers and A. L. Van Buren, “An exact expression for the Lommel-diffraction correction integral,” *J. Acoust. Soc. Am.*, vol. 55, no. 4, pp. 724–728, Apr. 1974, doi: 10.1121/1.1914589.
- [75] D. S. Kupperman and K. J. Reimann, “Ultrasonic wave-propagation characteristics and polarization effects in stainless steel weld metal,” Argonne National Lab. (ANL), Argonne, IL (United States), ANL-78-29, Mar. 1978. doi: 10.2172/6679929.
- [76] “Explorer,” *The Phased Array Company*.  
<https://thephasedarraycompany.com/offer/hardware-offer/explorer/> (accessed Feb. 09, 2023).
- [77] “McMaster-Carr.” <https://www.mcmaster.com/> (accessed Mar. 09, 2023).
- [78] “Rexolite®.” <http://www.rexolite.com/> (accessed Mar. 09, 2023).
- [79] “Rexolite Specifications | Rexolite®.” <http://www.rexolite.com/specifications/> (accessed Mar. 09, 2023).
- [80] C. Kim, H. Yin, A. Shmatok, B. C. Prorok, X. Lou, and K. H. Matlack, “Ultrasonic nondestructive evaluation of laser powder bed fusion 316L stainless steel,” *Addit. Manuf.*, vol. 38, p. 101800, Feb. 2021, doi: 10.1016/j.addma.2020.101800.
- [81] J.-Y. Kim, L. J. Jacobs, J. Qu, and J. W. Littles, “Experimental characterization of fatigue damage in a nickel-base superalloy using nonlinear ultrasonic waves,” *J. Acoust. Soc. Am.*, vol. 120, no. 3, pp. 1266–1273, Sep. 2006, doi: 10.1121/1.2221557.

[82] M. Treiber, J.-Y. Kim, L. J. Jacobs, and J. Qu, “Correction for partial reflection in ultrasonic attenuation measurements using contact transducers,” *J. Acoust. Soc. Am.*, vol. 125, no. 5, pp. 2946–2953, May 2009, doi: 10.1121/1.3106125.